Title: Analysis of collision centrality and negative pion spectra in 7Be + 9Be interactions at CERN SPS energy range

Author: Emil Kaptur

Citation style: Kaptur Emil. (2017). Analysis of collision centrality and negative pion spectra in 7Be + 9Be interactions at CERN SPS energy range. Praca doktorska. Katowice : Uniwersytet Śląski

Uniwersity of Silesia

Doctoral Thesis

ANALYSIS OF COLLISION CENTRALITY AND NEGATIVE PION SPECTRA IN ^{7}Be + ^{9}Be INTERACTIONS AT CERN SPS ENERGY RANGE

mgr Emil Kaptur

Supervisor:

dr hab. Seweryn Kowalski

June 2017

Contents

4

1. Introduction

This thesis presents the first analyses of the ^{7}Be + ^{9}Be data taken by the NA61/SHINE collaboration.

The NA61/SHINE experiment is a multi–purpose facility able to measure production of hadrons from variety of beams and target. The experiment placement at the CERN Super Proton Synchrotron accelerator provide large range of beam momenta ranging from $13A$ to $150A$ GeV/c for ion beam and up to 400 GeV/c for hadron beams.

The thesis will present results on two–dimensional spectra of negatively charged pions defined in rapidity and transverse momentum or mass. The spectra were obtained by subtracting simulated contribution of non–pion hadrons from the spectra of all negatively charged hadrons. Most of the negatively charged hadrons produced in heavy ion collisions are pions. Therefore model dependent correction is small and imprecision of the Monte–Carlo models does not play a large role in the accuracy of the final result.

The spectra are presented for five beam momenta and four centrality classes.

Furthermore, the results of the inelastic and production cross section of the ^{7}Be + ^{9}Be interaction analysis will be presented.

In addition to the physics analyses mentioned above the following technical results used as a building blocks of each ^{7}Be + ^{9}Be analysis in the collaboration will be presented:

- Event cuts in ^{7}Be + ^{9}Be

- Centrality determination in ^{7}Be + ^{9}Be data and simulation

- Parametrization of the particle showers produced in the NA61/SHINE calorimeter (The Projectile Spectator Detector — PSD)

- Simulation of the PSD

All of the above analyses were performed by the author of this thesis. In addition to the analysis the author is responsible for the following tasks in the collaboration:

- Expert of the following hardware subsystems:
  - Beam setup
  - Trigger detectors
  - Beam position detectors
  - Trigger logic system
- Building and testing new detectors:
  - New heavy ion trigger detectors
  - Scintillating fibre beam position detectors
- General software development, including:
  - Analysis packages
  - Parametrized PSD simulator
  - Maintenance and bug fixing of the legacy simulation chain
  - Computing speed optimization
- Monte–Carlo simulated data production for ^{7}Be + ^{9}Be

The part of this thesis related to the data analysis is rather large, exceeding 100 pages. To minimize the volume of this thesis the introductory parts related to the physics goals of the collaboration and detector description will be as short as possible.

2. Physics goals of the NA61/SHINE collaboration

2.1. Phases of nuclear matter

Matter exists in various phases. When the physical properties of matter are uniform in some region of space the matter is in some given phase. An ice cube have some given density, conductivity, or Young's modulus which are more or less uniform throughout it. Due to values of these physical constant it can be said that the ice cube is in a solid state. By changing some external parameters, for example by rising temperature the state of matter can change, a so called phase transition. Heating the ice cube will cause it to melt into liquid water. Liquid water will have some other physical properties than ice, however these properties will be more or less uniform throughout the volume of water.

An analogous behaviour can be seen in nuclear matter. By colliding nuclei with energies lower than some threshold value a gas of hadrons is produced. By rising the collision energy a phase transition into another state of nuclear matter can occur, i.e. so called quark–gluon plasma (QGP).

Hadrons are build by quarks and gluons. The quark within the hadron cannot be separated or detected independently due to property of the strong force called confinement. Differently than electric force between two charged particles the strong force between quarks do not decrease with the distance between them. At some point the creation of a new quark–antiquark pair becomes favourable energetically creating more hadrons instead of unbound quarks. Within the hadron gas each hadron behave as an independent and complete entity.

After the phase transition into the QGP the energy density is large enough to break the confinement. Within the QGP quarks and gluons behave as independent entities.

2.2. Phase diagram of nuclear matter

The external parameters required to obtain given phase of matter can be presented as a phase diagram. In the example of water the common way of expressing the phase diagram is plotting regions of temperature and pressure where given phase exists with the phase transition marked by the lines dividing different phases (see fig. 1 *(left)*).

For nuclear matter the most common parameters is the temperature and the baryochemical potential. These parameters are not measured directly in the collisions of nuclei but they are determined from the models based on measurements of various different observables. The comparison between phase diagram of water and nuclear matter can be find on fig. 1.
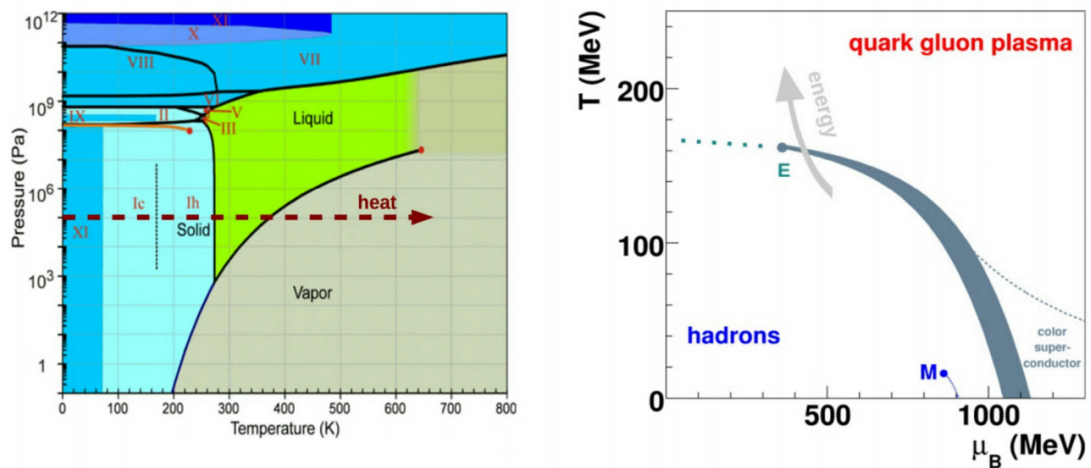
Figure 1: *(left):* Phase diagram of water *(right:)* Phase diagram of nuclear mater

By changing the collision energy and colliding system size probing the phase diagram of nuclear matter is possible. The phase diagram is relatively well scanned with proton + proton interactions with bubble chamber experiments at the low end of the energy spectrum through SPS, ISR, RHIC, and LHC experiments at the high end. NA61/SHINE is also providing additional, very precise reference data on proton + proton interactions at SPS energy range.

The heaviest colliding systems, like Pb + Pb and Au + Au have their energy dependence also known quite well. At the low end of the energy spectrum data from SIS and AGS is available, in the middle the SPS and RHIC experiments performed detailed energy scans and at the high end there are LHC experiments' measurements.

There is, however, very little information about colliding systems of intermediate sizes. In section 3 more information about such measurements will be given.

2.3. Two–dimensional phase diagram scan

NA49 experiment found the so called onset of deconfinement [1, 2] which means the first order phase transition between the hadron gas and QGP during their Pb + Pb beam energy scan. The measurements of the NA49 were motivated by the Statistical Model of Early Stage (SMES) [3–5], which will be shortly described later.

However many questions about the phase diagram of strongly interacting matter still remains. What are the exact parameters of the onset of deconfinement? Do we see it in proton + proton collisions? If not, what is the minimum colliding system size needed for the onset of deconfinement to occur? Is there a critical point? If so, where?

To answer this questions the NA61/SHINE experiment proposed a two–dimensional scan of measurements of various colliding systems at various beam momenta. The current status of the scan is visualised on fig. 2. The range of the phase diagram parameters probed by this scan is shown on fig. 3.

2.4. Statistical Model of Early Stage

Statistical Model of Early Stage predicted behaviour of various observables measured by the NA49 and then confirmed by the STAR experiments. NA61/SHINE uses these observables for the study of the onset of deconfinement.
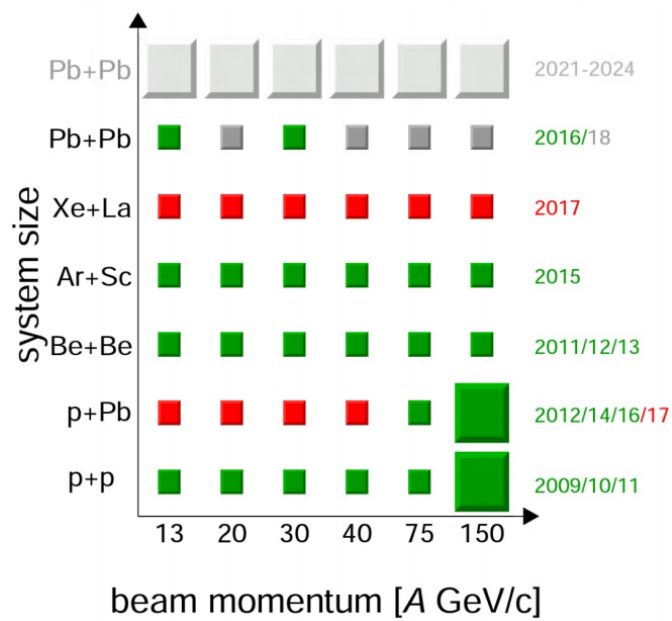
Figure 2: Current status of the NA61/SHINE two–dimensional scan
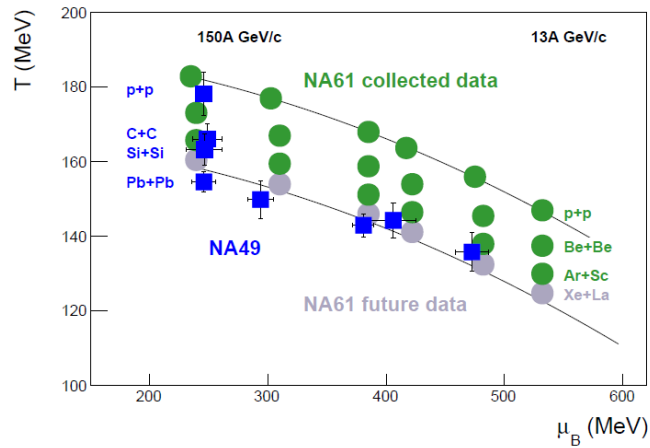
Figure 3: Phase diagram coverage of the NA61/SHINE data taking plan

2.4.1. "Kink"

Within SMES the entropy produced in the collision is carried mostly by the lightest (and most abundantly) produced particles, i.e. pions. The model predicts that the

12

entropy of the collision will rise with the energy of the colliding system. However, the increase of entropy will be faster within the deconfined QGP, than within the state of hadron gas.

An experimental variable used to probe the entropy of the collision is the average multiplicity of pions produced during the interaction divided by the number of "wounded" nucleons ($\frac{\langle \pi \rangle}{\langle N_W \rangle}$). To observe the increase of the value of the above observable with the energy of the colliding system $\frac{\langle \pi \rangle}{\langle N_W \rangle}$ is plotted as a function of the Fermi energy measure.

The number of wounded nucleons is a model dependant variable describing number of interacting nucleons during the heavy ion collision. For peripheral collisions, where impact parameter is large, the number of wounded nucleons is small (and number of non interacting spectator nucleons is large). For central collisions, with small impact parameters, number of wounded nucleons is large. The number of wounded nucleons is not accessible experimentally and have to be extracted from the Glauber Monte–Carlo models [6, 7].

The Fermi energy measure is a function of beam energy given by the equation:

$$F = \left[\frac{(\sqrt{s_{NN}} - 2m_N)^3}{\sqrt{s_{NN}}} \right]^{1/4} ,$$

where $\sqrt{s_{NN}}$ is the total centre-of-mass energy, m_N is the mass of a nucleon, and F is the Fermi energy measure.

SMES predicts change of the slope of $\frac{\langle \pi \rangle}{\langle N_W \rangle}$ at the onset of deconfinement (fig. 4).

Unfortunately, in this thesis the kink plot from ^{7}Be + ^{9}Be data will not be shown. Obtaining reliable number of wounded nucleons from models for such a small system is very difficult. The experimental collision parameters used to determine centrality (e.g. forward energy, multiplicity, forward multiplicity) are poorly correlated with model variables like impact parameter, number of projectile spectators or number of wounded nucleons.
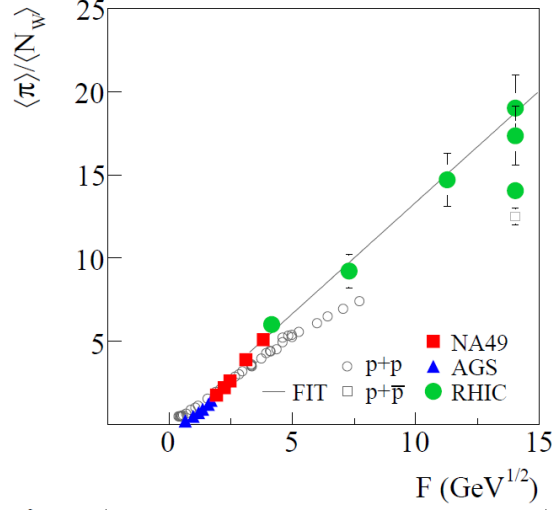
Figure 4: $\frac{\langle \pi \rangle}{\langle N_{\mathrm{W}} \rangle}$ as a function of Fermi energy measure. A change of slope is visible for heavy ion data at $F \approx 2.5\sqrt{\mathrm{GeV}}$.

2.4.2. "Horn"

According to SMES, in the hadron gas state (at low collision energies) the strangeness to entropy ratio increases with F due to the fact that the mass of the strangeness carriers (kaons) is larger than the temperature of the system. In the deconfined state of the QGP the mass of the strange quarks is lower than the temperature of the system, therefore strangeness to entropy ratio do not change drastically with the collision energy, and in addition it is lower than in hadron gas state.

As an experimental observable which reflect the strangeness to entropy ratio a ratio of the average number of positively charged kaons to the average number of positively charged pions is selected.

SMES prediced maximum of $\frac{K^+}{\pi^+}\big|_{y=0}$ at the onset of deconfinement (fig. 5).

The analysis of negatively charged pions presented in this thesis is used in obtaining the horn plot. In NA61/SHINE experiment it is difficult to obtain π^+ spectra at midrapidity due to the Bethe–Bloch curves crossovers and limited acceptance of

14
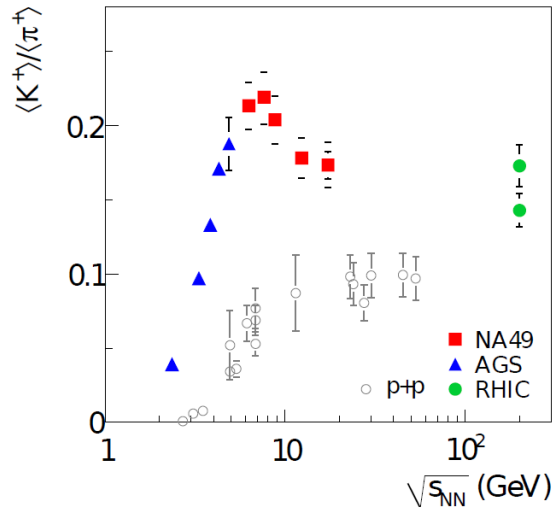
Figure 5: $\frac{K^+}{\pi^+}\big|_{y=0}$ as a function of collisions energy. Maximum is visible for heavy ion data at $\sqrt{s_{\mathrm{NN}}} \approx 7$ GeV

Time–of–Flight system, see fig. 6. Therefore, a measured π^+ meson spectra are extrapolated with the help of the spectra of π^- mesons to the midrapidity.
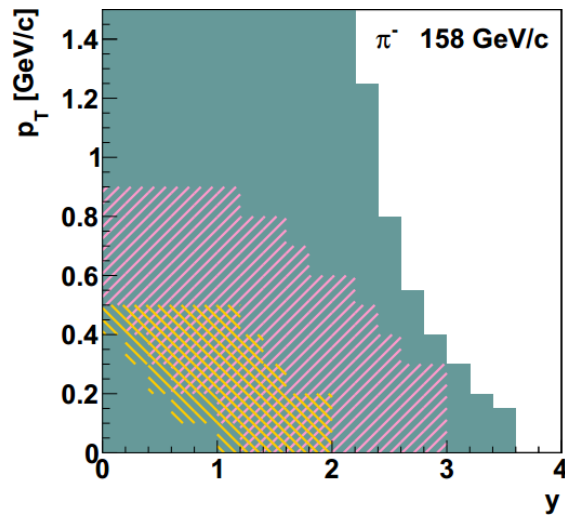
Figure 6: The acceptance of various particle identification method. The green area shows accepnance of the h^- method, the magenta and yellow areas show, respectively, acceptance of dE/dx and ToF identification methods.

3. Previous measurements of the light ion collisions at relativistic energies

The previous studies of the ^{7}Be + ^{9}Be interactions at relativistic energies are limited to one total inelastic cross–section measurement. The measurement was carried out by the dedicated cross–section experiment at Bevalac [8]. The experiment measured cross–section of various isotopes of light ions including ^{7}Be + ^{9}Be. The cross–section was obtained at beam momenta of $1.45A$ GeV/c. This measurement will be compared with the Glauber Monte–Carlo model and results of the NA61/SHINE experiment in **??**.

More data is available for the ^{12}C + ^{12}C interactions. While the carbon system is heavier than the beryllium system, but it is the closest system with available measurements.

The Hades experiment measured dilepton [9], pion [10], lambda [11] and kaon [12] spectra in ^{12}C + ^{12}C interactions at beam momenta of $1A$ and $2A$ GeV/c. The results of the Hades experiment on negatively charged pion production would be difficult to compare with the results presented in this work. The difficulty arises due to centrality was selection made only by multiplicity requirements of the trigger system. Hades provide pion multiplicity extrapolated to full phase–space per participant nucleon. Such value could be compared with the data presented in this work. However, the calculation of the number of participant nucleons in ^{7}Be + ^{9}Be collisions have large model dependence and further work is needed to obtain multiplicity per participant nucleon in NA61/SHINE data with small systematic error.

The NA49 [13] experiment took data with a secondary, fragmentation beam of ^{12}C on carbon target at $40A$ and $158A$ GeV/c [14]. However this data have various problems. The ^{12}C fragmentation beam was heavily contaminated by other ions with $Z/A = 1/2$ as well as isotopes close to this ratio. The NA49 collaboration sometimes calls the colliding system as "C"+C. The mid–central collisions were selected for this data set to rise the available statistics. The extrapolation to

full phase–space was performed assuming symmetrical rapidity distribution. The NA61/SHINE data on ^{7}Be + ^{9}Be interactions shows that for such small systems with centrality selected only in the projectile hemisphere (e.g. from the measurement of forward energy) the rapidity spectrum is not symmetric.

4. History of zero–degree calorimeters

The NA61/SHINE experiment is using Projectile Spectator Detector (PSD) as a detector measuring energy of hadrons and ions produced at low polar angles. One of the goals of the PSD is the measurement of the centrality of the collision.

By measuring energy of non–interacting spectator particles the final physics result is correlated with the centrality selection method weaker than by using e.g. multiplicity.

The history of hadronic calorimeters use in heavy ion experiments starts with Bevalac experiments in the 1970's.

The Plastic Ball experiment [15] at Bevalac used scintillators which were displaced from the main experiment to construct the Plastic Wall (fig. 7). The displacement lowered occupancy of the detector in the forward region. The Plastic Wall [15] covered phase–space occupied by the spectator protons.

The Streamer Chamber experiment [16] used a purpose build scintillator hodoscope with acceptance covering spectator protons. The hodoscope was named Forward Wall (fig. 8).

The NA61/SHINE [17] is a descendant of a series of heavy ion experiments at CERN SPS. These experiments: NA5 [18], NA35 [19], and NA49 [13] shared a common calorimeter. Each of them modified and improved the calorimeter (named Veto Calorimeter). Only latest iteration of the Veto Calorimeter of the NA49 experiment will be described (fig. 9).

The Veto Calorimeter was build as a Pb/Fe Scintillator sandwich. It consisted with
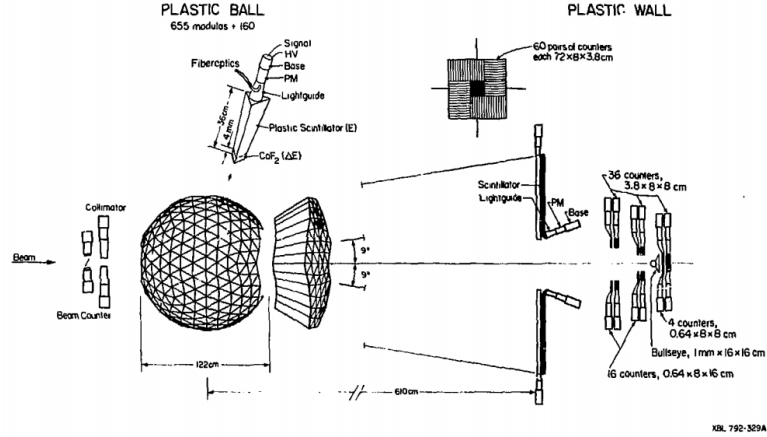
Figure 7: The schematic of the Plastic Ball experiment. The Plastic Wall used in the high occupancy forward region was covering phase–space region of spectator protons.
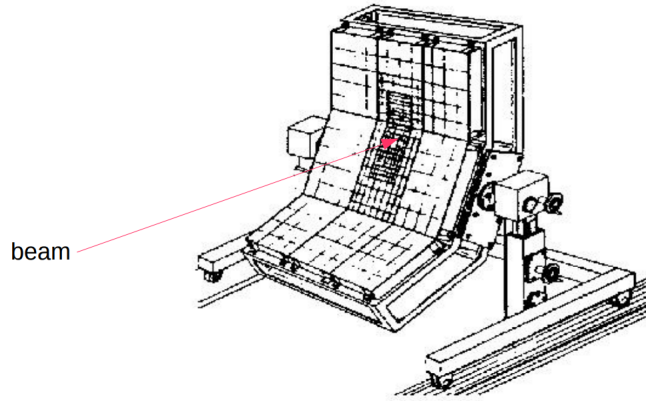
Figure 8: The Forward Wall of the Streamer Chamber experiment at Bevalac.

four modules in transverse direction, electromagnetic part with Pb/Sci construction and hadronic part with Fe/Sci construction. To allow measurements at different energies with similar phase space coverage an iron collimator was used.

The Zero–Degree Calorimeter (ZDC) [20] of the STAR experiment [21] at Relativistic Heavy-Ion Collider (RHIC) was constructed as a sandwich of tungsten plates and optical fibres read out by the Photomultiplier Tubes (PMTs). The light in the optical fibres was produced by the Cherenkov radiation of secondary particles
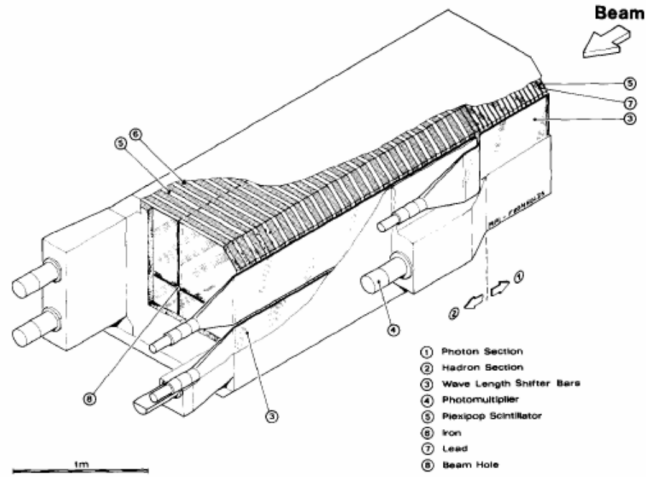
Figure 9: Calorimeter of the NA5/35/49 experiments.

produced in tungsten absorber plates. The schematic of one module of the ZDC is presented on fig. 10.

Currently, the CALICE collaboration [22] works on designing, testing and constructing a calorimeter system for the International Linear Collider [23]. The tested prototype have very large granularity in both longitudinal and transverse direction. Such large granularity allows to precisely measure and fit the shower produced by the impinging hadrons. An analysis inspired by measurements of CALICE collaboration will be presented in this work.
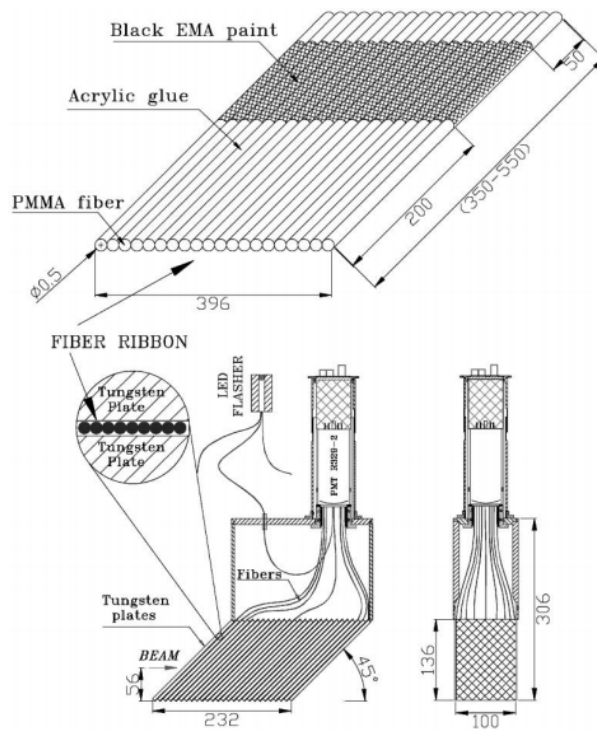
Figure 10: Schematic of one ZDC module of the STAR experiment.

5. Experimental Setup

This thesis was prepared using the NA61/SHINE detector system. This chapter will focus on the experimental setup in years 2011 – 2013, when data on ^{7}Be + ^{9}Be interaction was taken. Detailed description of the NA61/SHINE detector system for various data taking periods as well as detailed description of each detector can be found in [24].

NA61/SHINE is a multi-purpose facility able to measure particle production in hadron—proton, hadron—nucleon and nucleon—nucleon interactions. The facility is placed at the CERN Super Proton Synchrotron in the H2 beamline of the North Area.

The detector system is a large acceptance spectrometer with excellent particle identification capabilities. The base of the detector system consists of five Time Projection Chambers (TPCs). Two of them are placed in the magnetic field of the superconducting magnets (Vertex TPCs, VTPCs) enabling momentum determination. Two Main TPCs (MTPCs) are a large volume chambers placed downstream of the VTPCs. MTPCs are used for the particle identification based on the specific enegry loss of particles. The fifth TPC, Gap TPC (GTPC), is a small TPC placed on the beamline between the VTPCs. The GTPC have many supplementary uses, like momentum determination of high momentum particles or cross section determination. Additional two chambers (Forward TPCs, FTPCs) are being build to supplement forward tracking, high momentum determination and particle identification.

The particle identification is further supplemented with two Time of Flight (ToF) walls. The ToF walls are placed to cover mid–rapidity acceptance of kaons. Each wall is a pixel ToF based on scintillators and photomultiplier tubes.

For centrality determination in heavy–ion collisions, a high resolution, modular zero–degree calorimeter, named Projectile Spectator Detector (PSD), is used. High modularity of the PSD allows to fine–tune centrality selection and minimize biases.

The beamline of NA61/SHINE is well instrumented to allow for high beam purity even with secondary ion beams. The beam instrumentation consists of scintillator counters used for triggering and beam particle identification, veto scintillation counters (with a hole in the middle) for rejection of upstream interactions and beam halo particles, and Cherenkov charge detector. Additionally there are three Beam Position Detectors (BPDs) used for determination of the beam position and slope as well as charge measurement.

The schematic of the experimental setup is shown on fig. 11.
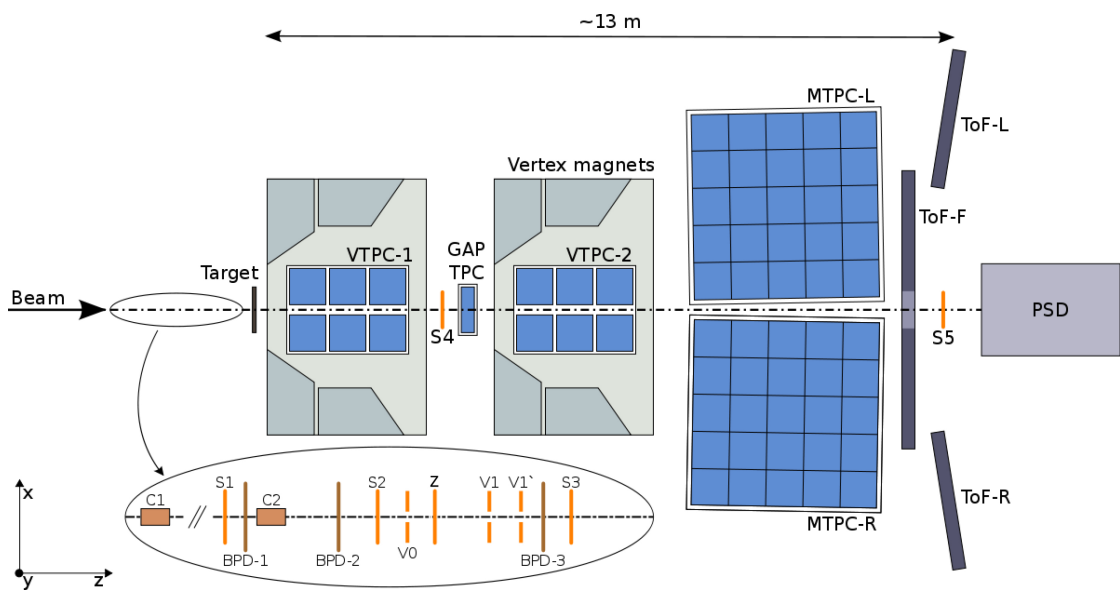
Figure 11: Experimental setup of the NA61/SHINE experiment

5.1. Beam

5.1.1. Accelerator Chain

In the following section a lead ion acceleration chain will be described, since the lead ions were used to produce secondary beryllium beam.

The CERN ion acceleration chain starts with an Electron Cyclotron Resonance

(ECR) source. The ECR source provide lead ions with an energy of 2.5 keV/u, a spectrometer placed at the exit of the source selects Pb^{29+} ions for further acceleration.

The Pb^{29+} ions are accelerated by the Radio–Frequency Quadruple (RFQ) to the beam energy of 250 keV/u before acceleration in the LINAC3 linear accelerator. LINAC3 accelerate the ions to the beam energy of 4.2 MeV/u. A 0.3 μm thick carbon foil provides the first stripping stage at the exit of LINAC3, which is followed by a spectrometer selecting the Pb^{54+} charge state.

The Pb^{29+} ions are injected into the Low Energy Ion Ring (LEIR). LEIR accelerate lead ions to the beam energy of 72 MeV/u. After acceleration the beam is extracted towards Proton Synchrotron (PS).

The PS accelerate ions to the beam energy of 5.9 GeV/u. After acceleration the beam is extracted through a final stripping stage (1 mm aluminium foil) to produce Pb^{82+} ions.

The Pb^{82+} ions are injected into Super Proton Synchrotron (SPS) which accelerate them to a desired beam energy between 13 GeV/u and 160 GeV/u. The lower beam energy limit is due to stability reason, and the higher limit is due to limits of the power supplies and energy in the magnets. The lead beam used for production of beryllium beam was debunched naturally, which means that some of the original time structure of the beam is retained after extraction to the North Area.

5.1.2. Secondary Beryllium Beam

The Pb^{82+} ions extracted from the SPS were steered toward fragmentation target placed 535 m from the NA61/SHINE experiment. The fragmentation target is a 180 cm long beryllium (use of the same material as the wanted beam is coincidental) plate. The lead ions passing through 180 cm of target material undergoes fragmentation, resulting in a mixture of nuclear fragments. The fragments consists of nucleons not participating in inelastic collisions (spectators), and consequently their momentum per nucleon is equal to the beam momentum per nucleon smeared
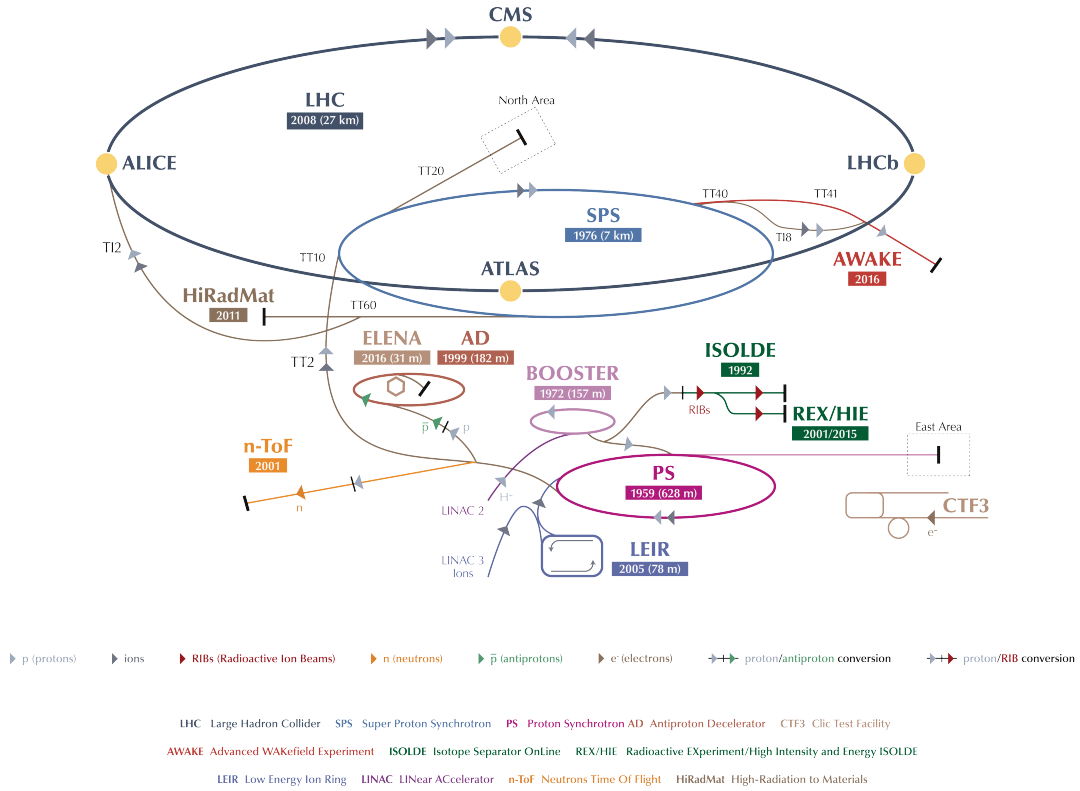
Figure 12: Accelerators of CERN. NA61/SHINE is located in the North Area [25]

by the Fermi motion momentum.

Wanted beam composition can be selected from the mixture of nuclear fragments (and the remnants of primary Pb beam) with the help of two large spectrometers placed on the beamline. These spectrometers allows to select beam particles based on the particle rigidity: $B\rho = 3.33p_{\text{beam}}/Z$, where $B\rho$ can be selected by setting required current on the dipole magnets of the spectrometer, p_{beam} is the momentum of the beam particle and Z charge of the beam particle. As previously mentioned, momentum per nucleon is roughly equal for all nuclear fragments, the rigidity equation can be rewritten to:

$$B\rho = 3.33\frac{p_{\text{beam}}}{A}\frac{A}{Z},$$

which means, that in practice, spectrometers selects particles with given A/Z ratio.

NA61/SHINE experiment choose ^{7}Be as the beam particle. The ^{7}Be is proton

heavy, which helps with rejection of heavy fragments (which are neutron heavy) by the A/Z ratio selection of beamline spectrometers. Additionally, ^{8}Be is very short lived, decaying into two α particles, which helps in obtaining mono-isotopic beryllium beam. The beam charge composition are visible on fig. 13 and beam mass composition is visible on fig. 14.
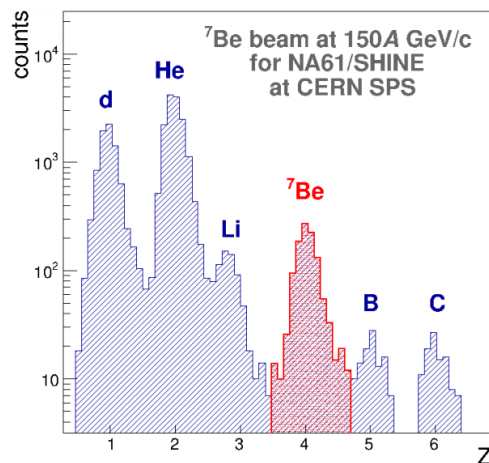
Figure 13: Charge of the beam particles measured by the Z detector
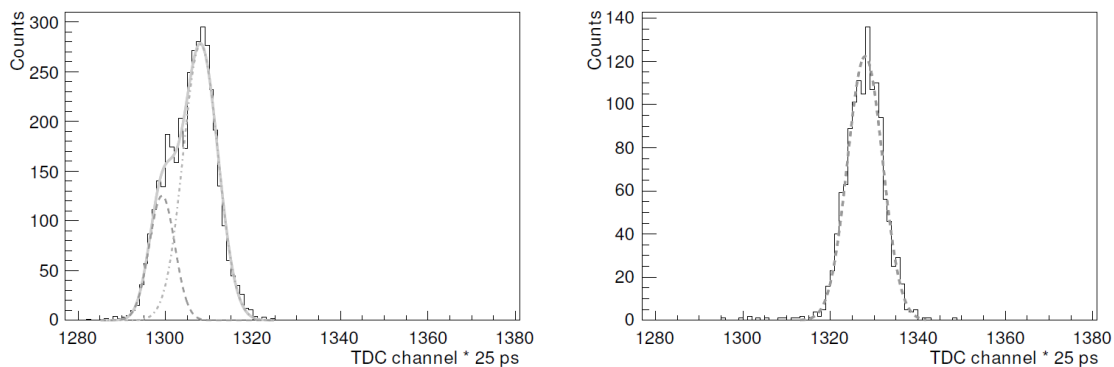
Figure 14: Mass of the beam particles. On the left, measurement for carbon ions show double Gaussian structure due to two isotopes of carbon in the beam. On the right, measurement for beryllium ions show single Gaussian distribution, indication isotopic purity of the beryllium in the beam.

The primary lead beam used to produce secondary beryllium beam is bunched into short bursts of particles to facilitate acceleration. The time structure of the beam is shown on fig. 15. Although nowadays CERN ion beams send to the North Area are actively debunched, which results in uniform time distribution of beam particles, it was not the case during beryllium data taking.
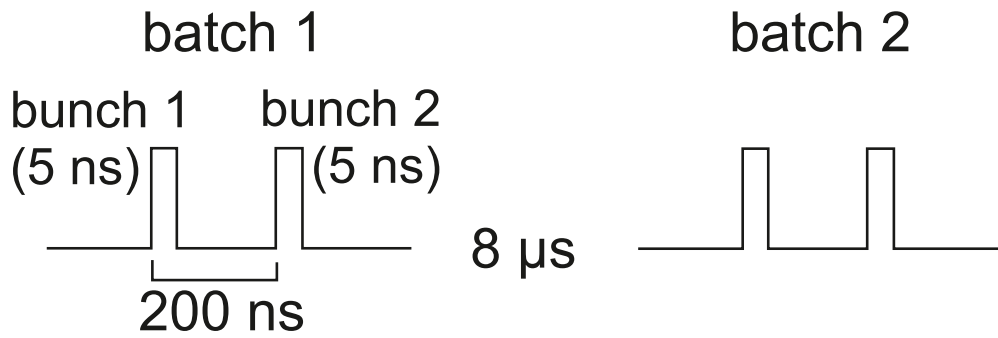
Figure 15: Schematic of the beryllium beam time structure. The particles were arriving to the experiment in short bursts separated by longer time without beam.

6. Datasets

This work is based on the ^{7}Be + ^{9}Be interactions gathered by the NA61/SHINE experiment during two data taking campaigns. During the first data taking period in late 2011 data at beam momenta of $40A$, $75A$, and $150A$ GeV/c were taken. The second campaign during which data at beam momenta of $13A$, $19A$, and $30A$ GeV/c were recorded, took place in early 2013. Due to the very low quality of the beam at $13A$ GeV/c beam momentum, the pion spectra results from this dataset will not be presented in this work.

The high momenta ^{7}Be + ^{9}Be data taking was the first ion beam in the NA61/SHINE experiment. The experiences obtained during this period were used to improve detectors, especially PSD, and trigger conditions for the low momenta ^{7}Be + ^{9}Be data taking (more informations in section 5.1.2). The two periods of the beam time were planed exactly for this reason. High momenta beams form the SPS have a very good quality, therefore imperfect detector performance is acceptable. The quality of the beams of low momenta is much worse, therefore even small improvements in data taking efficiency are very helpful.

The data was collected in two target configurations: target inserted and target removed. Target inserted configuration constituted $\approx 90\%$ of all events. Target removed configuration, constitutes $\approx 10\%$ of all events. The target removed configuration was recorded in order to measure background from the interactions of the beam particles with the material in and around the beamline.

Various trigger configurations were used to collect data. In the low momentum data four trigger definitions were used: identified beam, identified central interaction, unidentified beam and unidentified minimum bias interaction. In high momentum data three trigger definitions were used: identified beam, identified central interaction and unidentified beam.

Identified beam triggers constitutes $\approx 10\%$ of recorded events, most of the rest are identified central interaction triggers. Unidentified triggers were recorded with very low statistics, mostly for online monitoring of the beam composition.

The schematic of the placement of the beam and trigger detectors can be seen on fig. 16. The trigger detectors consists of: set of scintillators recording presence of the beam particle (S1, S2), set of veto detectors, i.e. scintillators with a hole used to reject beam particles passing far from the centre of the beamline (V0, V1), a charge detector (Z), and an interaction trigger detector, which is used to check whether beam particle changed charge after passing through target (S4).

The trigger definitions as well as approximate percentage of data recorded with each trigger are presented for the low momentum beams in table 1 and for the high momentum beams in table 2.
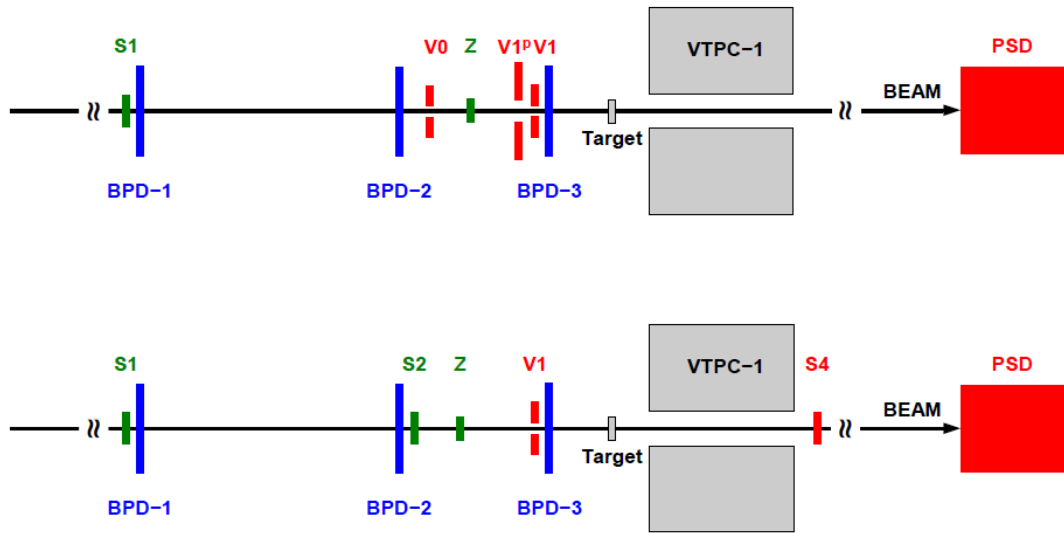
Figure 16: The schematic of the placement of the beam and trigger detectors in a high momentum data taking *(top)* and a low momentum data taking *(bottom)*

An interaction trigger was defined differently for the low and high momentum data taking. In the low momentum data, an event is tagged as an interaction when the signal from the S4 scintillator is lower than a typical signal from the Beryllium ion. In the high momentum data no minimum bias interaction is defined, instead an event is tagged as an interaction when energy deposited in the PSD is lower than

Table 1: Trigger definitions during low momentum data taking (id. — identified, unid. — unidentified).

Name	Description	Definition	Recorded fraction
T1	Id. beam	$S1 \cdot S2 \cdot \overline{V1} \cdot Z(Be)$	30%
T2	Id. central interaction	$S1 \cdot S2 \cdot \overline{V1} \cdot Z(Be) \cdot \overline{S4} \cdot \overline{PSD}$	60%
T3	Unid. beam	$S1 \cdot S2 \cdot \overline{V1}$	5%
T4	Unid. mbias interaction	$S1 \cdot S2 \cdot \overline{V1} \cdot \overline{S4}$	5%

Table 2: Trigger definitions during high momentum data taking (id. — identified, unid. — unidentified).

Name	Description	Definition	Recorded fraction
T1	Id. beam	$S1 \cdot \overline{V0} \cdot \overline{V1} \cdot \overline{V1'} \cdot Z(Be)$	6%
T2	Id. central interaction	$S1 \cdot \overline{V0} \cdot \overline{V1} \cdot \overline{V1'} \cdot Z(Be) \cdot \overline{PSD}$	90%
T3	-	-	0%
T4	Unid. beam	$S1 \cdot S2 \cdot \overline{V0} \cdot \overline{V1} \cdot \overline{V1'}$	4%

some threshold value, allowing only for a central interaction trigger.

The recorded number of events for all beam momenta are presented in table 3.

Table 3: Number of recorded Target Inserted events for all measured beam momenta. Different trigger definitions are summed together.

p_{beam} [GeV/c]	N_{in}
$13A$	2.698×10^6
$19A$	3.155×10^6
$30A$	3.894×10^6
$40A$	2.858×10^6
$75A$	3.936×10^6
$150A$	2.828×10^6

7. Event selection

Various analyses differ in the requirements for the event selection. In the following section all event cuts used in the analyses, together with the discussion of the most common values for the cuts, will be presented.

The event cuts can be divided into two families: the non–biasing event cuts and the biasing event cuts. The non-biasing event cuts do not use variables which values depend on whether interaction took place or what was the type of the interaction. This family cuts on the beam composition, beam time structure and beam position. The non-biasing cuts can be made arbitrarily strong. The only drawback would be lower data statistics, but systematic effects e.g. related to the misidentification of the beam particle would be lower.

The second family, biasing cuts use variables which depend on interaction. These cuts are mostly used to reject background from the out-of-target interactions or to select centrality. Biasing cuts can and do bias the data selected for the analysis. For example requirement of a good fit quality of the primary vertex reject more low multiplicity events, where vertex fit is more difficult, than high multiplicity events, skewing mean multiplicity of produced particles to higher values. To assess the amount of bias caused by this family of cuts, a detailed Monte–Carlo simulations

are carried out, and the biases are corrected.

The non–biasing cuts are listed below, they will be explained in more detail later:

- Beam particle identification cuts:

    – S1 vs. Z cut,

    – S2 vs. Z cut,

    – Beam Position Detector (BPD) charge vs. Z cut.

- Beam time structure cuts:

    – Multi-Hit Time Digital Converter (MHTDC) beam cut,

    – MHTDC interaction cut,

    – Z vs. Z delayed cut,

    – BPD RMS cut.

- Beam position cuts.

The list of biasing cuts is presented below:

- Existence of the primary vertex,

- Fit quality of the primary vertex,

- Position of the reconstructed primary vertex along the beamline,

- Gap Time Projection Chamber (GTPC) beryllium cut,

- Projectile Spectator Detector (PSD) centrality cut.

7.1. Calibration of beam and trigger detectors

To maximize charge resolution and simplify cuts, the variations of the response of the beam and trigger detectors have to be calibrated out. The response of the beam counters was calibrated first in time with a strong cut on beam position to separate gain variation and beam movement. Then a time-calibrated signal was binned in x and y and each of such bins was calibrated again to suppress signal height dependence on how close beam particle hit to the Photomultilier Tube (PMT).

The calibration procedure consisted of fitting a convolution of Gaussian and Landau distribution to the helium and beryllium peaks, and then setting the maxima of these distributions to the Z^2 of the respective ions (fig. 17). The calibration procedure was performed in 1+2D bins of time and beam particle position. The procedure had to be automatic due to large number of calibration bins for each detector.
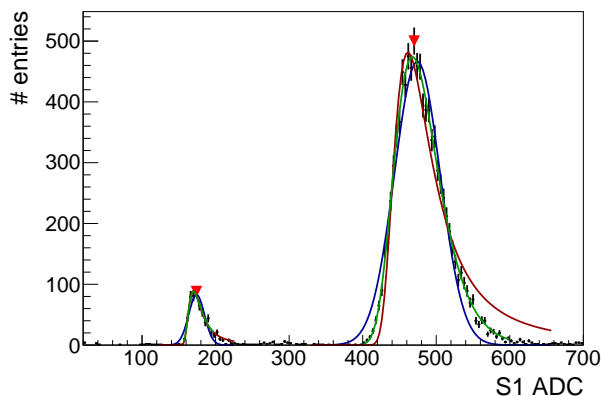
Figure 17: An example bin from the position calibration of the S1 counter response. Helium and beryllium peaks are visible. The red triangles represent the result of the peak finding algorithm. The blue curve is a test fit by the Gaussian distribution. The red curve is a test fit by the Landau distribution. The green curve is a fit by a convolution of the Gausiann and Landau distributions. The calibration factors were read out from the fitted convolution.

32

The S1 response before and after calibration can be seen on fig. 18.
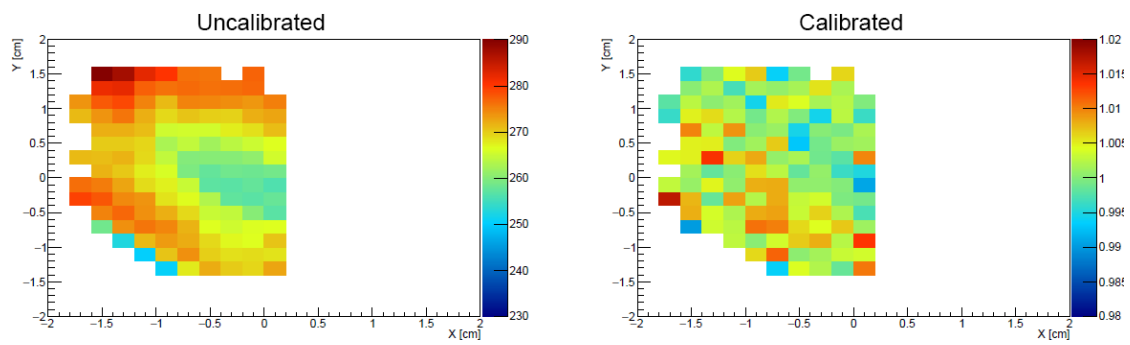
Figure 18: Average response of the S1 detector as a function of the beam position. On the left, the uncalibrated ADC values show variations of the order of 10%. On the right, after calibration the variations of the calibrated response are of the order of 1%.

7.2. Beam composition cuts

The beam used in the beryllium data taking was a secondary, bunched beam. The beam comprised of many ion species, therefore good beam particle identification was necessary. The online cut used in the trigger system was a simple 1D cut on the response of the quartz Cherenkov Z detector. Spectrum of the Z detector can be seen on fig. 19. Such cut was insufficient for the good rejection of the non–beryllium ions. The fig. 20 shows the inefficiency of the trigger set only on the Z detector.
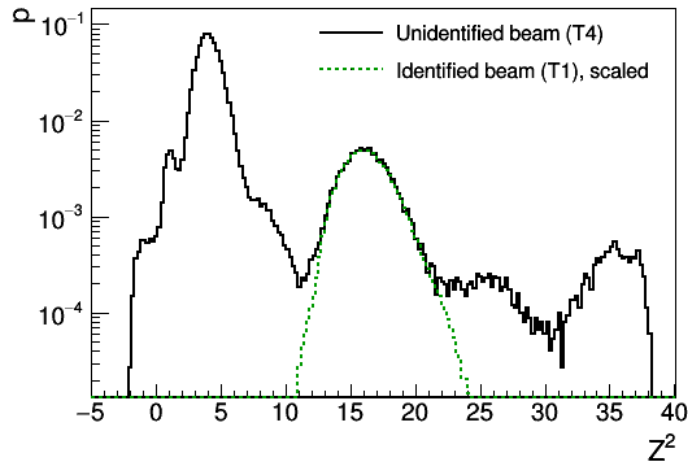
Figure 19: Probability density of obtaining given value of Z^2 from the Z detector measurement. Black line shows events recorded with the unidentified beam trigger. Green dashed line shows events recorded with identified beam trigger. Data recorded with identified beam trigger was scaled to the maximum of the beryllium peak from the unidentified trigger data.

Cuts on various correlation plots between response of different beam detectors (see fig. 21) were used to improve rejection of the non-beryllium ions. Each beam detector had various advantages and disadvantages for this task. The response of the beam counters depends on time due to gain fluctuations, as well as position of the beam particle. The particles hitting closer to the PMT give higher signal than the particles hitting further from the PMT.
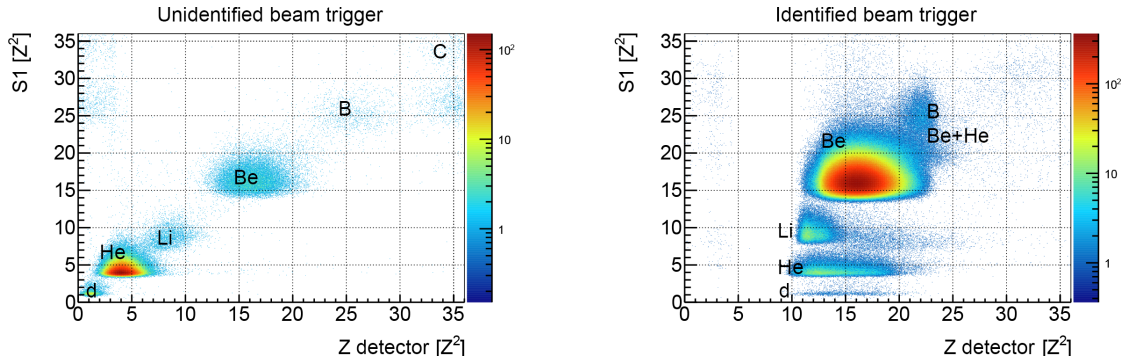
Figure 20: Correlation between charge measured by S1 counter and Z detector. On the left the unidentified beam trigger events were plotted, different ions are labeled. On the right the identified beam trigger events were plotted. The beam contained much larger fraction of deuterons and helium ions than beryllium ions. The enhancement of the beryllium peak by the trigger set on the Z detector automatically enhances tails of the distributions of the lighter ions. Also enhancement of the boron tail and beryllium and helium off-time particle within the integration time (120 ns) of the beam counters is visible.

Z detector was specially constructed to resolve charge of the beam particles. Its main advantage was a very low Landau tail of the amplitude spectrum. A low Landau tail ensured that only small amount of light ions can be misidentified as beryllium. This attribute made it a good trigger detector as well.

Main advantage of the S1 detector was a very good charge resolution obtained by reading out the scintillator with four PMTs. It allowed good separation between various ion species. Unfortunately, the S1 was placed in a very upstream position ≈ 30 m from the target. Using only the S1 for identification would not reject beryllium ions that interacted and fragmented before reaching the target.

The S2 detector, placed ≈ 5 m upstream from the target, was used to reject interactions between S1 and the target, although S2 charge resolution was not as good as the resolution of the S1.

35
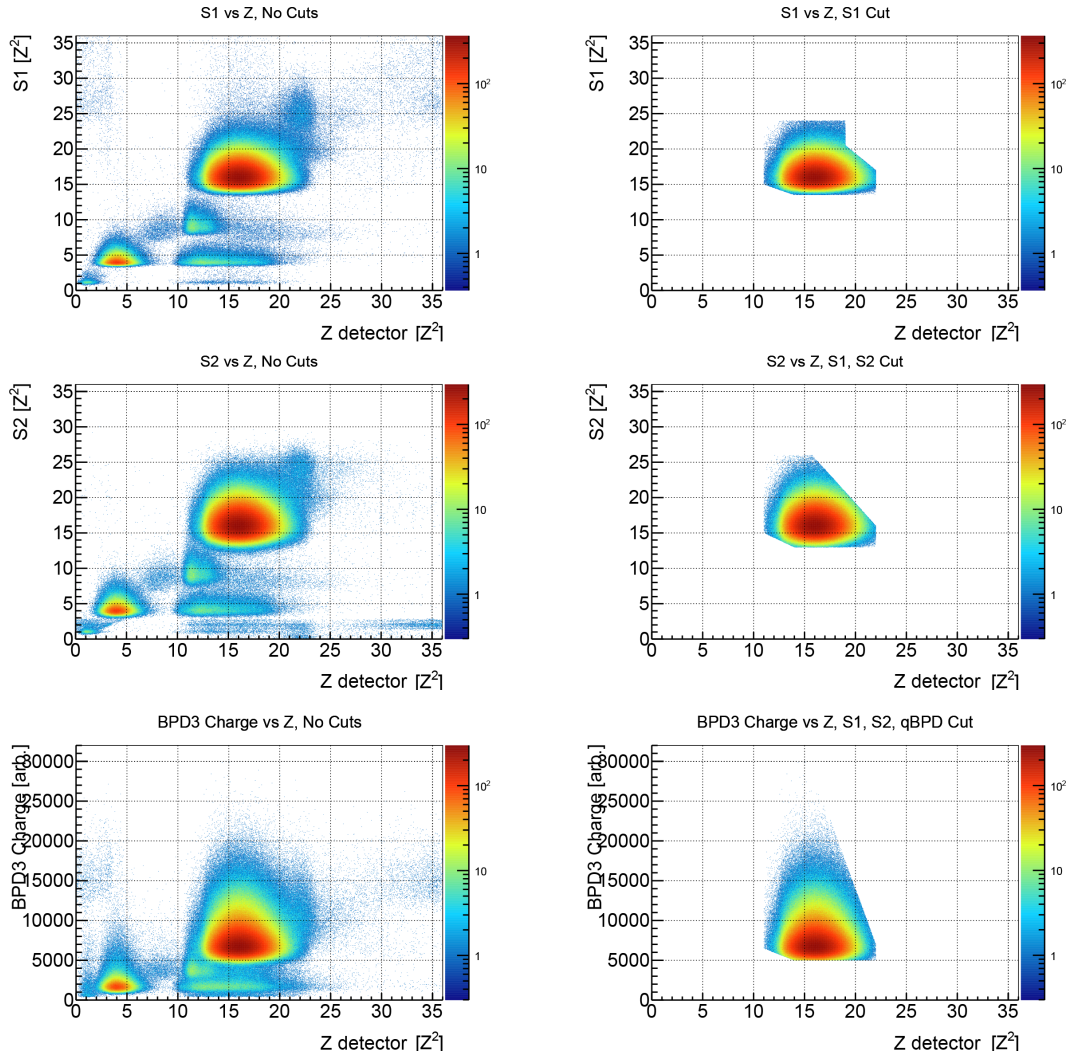
Figure 21: Beam composition cuts. The plots show correlation between charge measured by two different beam and trigger detectors. Data from all triggers is added together. Left column shows distributions before the beam composition cuts. Right column shows distribution after the beam composition cuts. In addition of selecting pure beryllium beam, these cuts reject $Z^2 = 20 = 4^2 + 2^2$ discarding most of the offtime from ions heavier than helium within the integration time of the beam detectors (120 ns).

To reject interactions of beryllium just before the target, a charge deposited in the BPD3 was used. The BPD3 is a small volume MWPC, thus charge resolution is very poor, nevertheless it is enough to reject interactions up to 90 cm before the target without large loss of the beryllium particles.

7.3. Beam time structure cuts

Due to a bunched time structure of the beam there was a large probability of two or more particles coming in a very short time (< 1 μs) one after another. Such events can cause bias due to multiple interactions in the target, as well as bias in the energy deposited in the PSD. Such particles coming in a short time after the trigger particle are called off-time particles.

An off-time beam particle can skew the results of the cross-section measurement or a centrality determination by, respectively, changing the apparent charge of the beam particle or increasing the energy deposited in the PSD. Moreover, an off-time interaction can produce additional particles which can fit to the main vertex of a triggered interaction increasing the apparent particle multiplicity. Therefore, the removal of the events with an off-time particle is important.

7.3.1. Multi-Hit Time Digital Converter Cut

To reject such events a combination of various cuts were used. The main cut was performed with the data recorded by the Multi Hit Time Digital Converter (MHTDC), a device registering arrival time of the signals with respect to the trigger signal.

Two channels of the MHTDC were used for the off-time rejection. The first channel was connected to the signal from the S1 detector registering the arrival time of all particles in the beam, an example plot showing the time structure of the beam is presented in fig. 22. The second channel of the MHTDC was connected to the minimum bias interaction trigger, providing information whether and when

additional interactions took place.
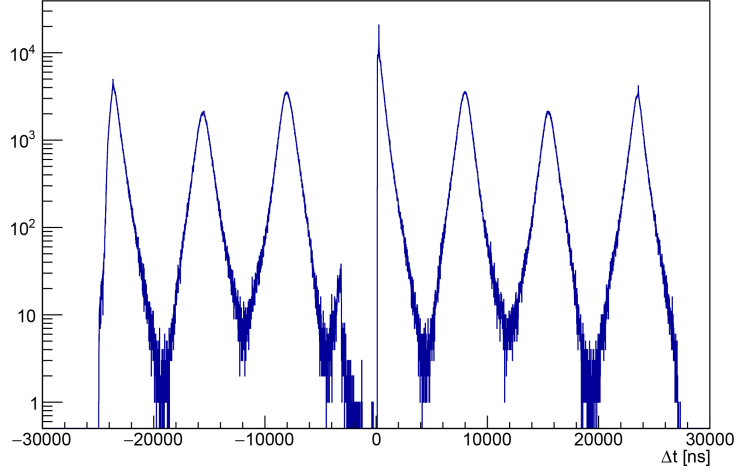
Figure 22: Time distribution of the off-time particle closest to the trigger. Trigger particle arrive at 0 ns. The bunched structure of the beam is visible as the peaks of the distribution.

The standard value of the MHTDC beam (S1) cut was chosen at 4.5 μs rejecting any events with additional beam particle within the same beam bunch as the trigger particle.

The standard value of the MHTDC minimum bias interaction cut was selected at 25 μs rejecting any events with an off-time interaction which would be seen within the TPCs volume.

Unfortunately, MHTDC cannot see particles coming within 120 ns from the trigger particle due to the signal width limitation.

7.3.2. Gap TPC off-time crosscheck

The presence of the off-time particles at > 1 μs can also be checked with the help of the TPCs. In the TPCs the y component of the cluster position is determined from the signal arrival time measurement and the known electron drift velocity. Thus off-time particles will appear shifted in y. For example an off-time deuterium

coming 2 µs after the trigger will look like a deuterium coming with the trigger particle shifted 2.8 cm down (the drift velocity is approximately 1.4 cm µs^{-1}). Likewise, particles produced due to off-time interaction will appear to have the interaction vertex shifted in y.

During both Beryllium data taking campaigns the Gap TPC was placed in the beam. A histogram showing a track angle in YZ plane as a function of a Y position without the off-time particle cuts for low and high beam momentum can be seen on fig. 23. The structures are explained on the fig. 24. A similar histogram with a MHTDC cut of off-time particles can be seen on fig. 25.
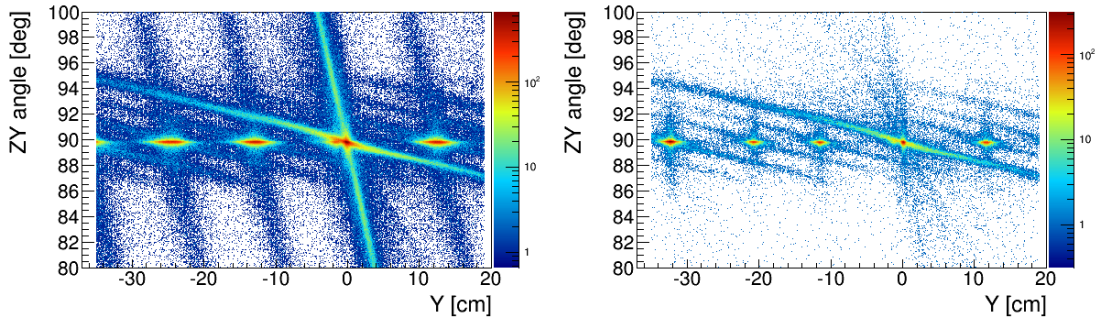
Figure 23: Histogram of the particle track Y position and ZY angle measured by the GTPC. Explanation of the visible structures is given on fig. 24. 30A GeV/c *(left)*, 75A GeV/c *(right)*.

In the fig. 25 one can see residual off-time particles left after the MHTDC cut. The threshold on the S1 signal was set too high allowing some deuterons to pass undetected. The amount of the residual off-time particles can be estimated by plotting a histogram of the Y position of the particles that comes with an angle in the range from 89° to 90° and counting the number of the off-time events in one bunch of the beam. An example plots can be seen on fig. 26. For low momenta data taking the amount of the residual off-time within the trigger bunch is equal to 0.05% of the events after all cuts, and thus is negligible. For high momenta data taking the amount of the residual off-time within the trigger bunch is equal to 1% of the events after all cuts. Fortunately, with the target interaction length
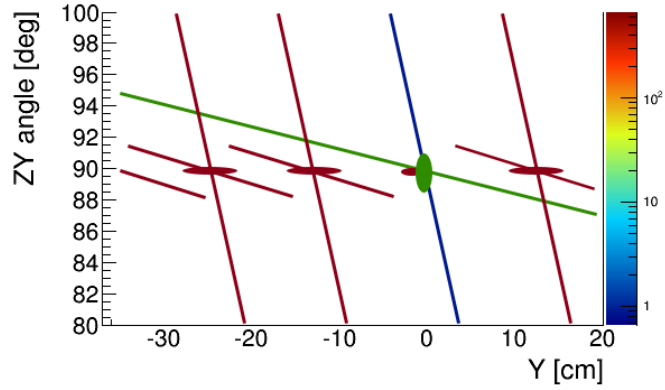
Figure 24: Schematic of the particle track Y position and ZY angle measured by the GTPC. The green oval represents the projectile and the projectile fragments. The green line represent the particles produced in interaction within the target. The blue line represent the particles produced by the interactions within the S4, beam pipe windows and GTPC entry window. The red lines and ovals represent off-time particles. Each oval correspond to the different bunch of the beam.
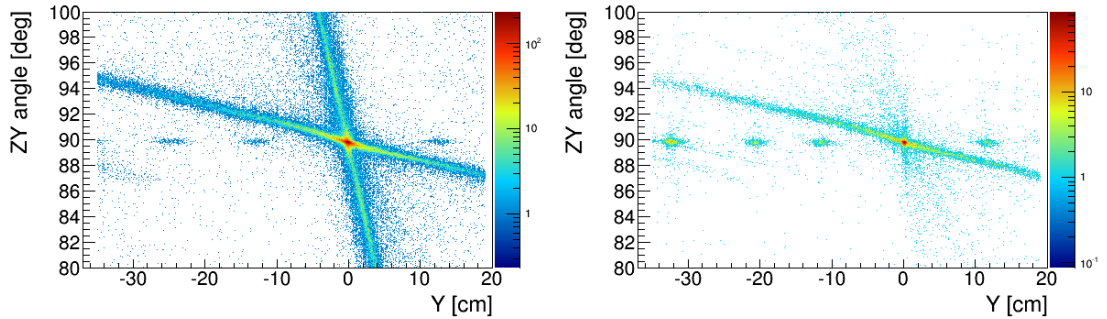
Figure 25: Histogram of the particle track Y position and ZY angle measured by the GTPC with MHTDC off-time particle cut set to eliminate events with off-time particles within $25\,\mu\text{s}$ of the trigger particle. $30A$ GeV/c *(left)*, $75A$ GeV/c *(right)*.

for deuterium of less than 10% and relatively low multiplicity of d+Be collisions, the actual effect of this residual off-time is lower than 0.1%, which will be added to

the systematic errors.
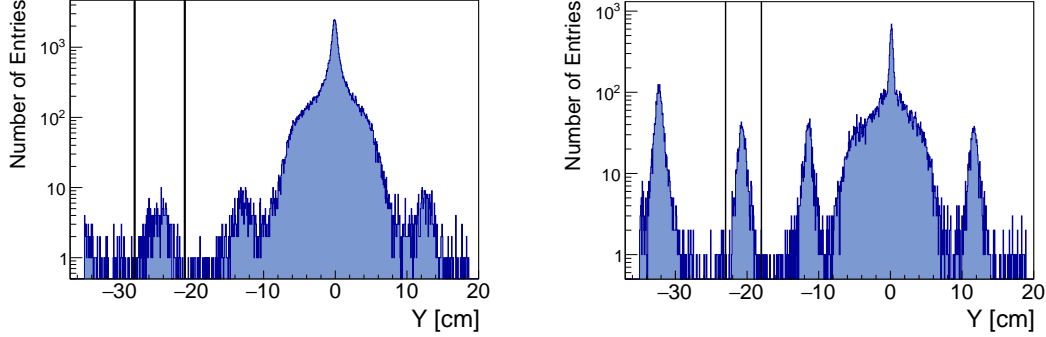
Figure 26: Y position of the tracks measured with GTPC with an angle between 89° and 90°. Region used for calculating amount of the residual off-time is marked: $30A$ GeV/c *(left)*, $75A$ GeV/c *(right)*.

7.3.3. Z vs. Z delayed cut

To handle off-time within 120 ns from the trigger, which cannot be seen with the MHTDC or the Gap TPC, another cuts have to be devised.

Some of this off-time will be cut with the beam composition cuts. In the presence of the off-time the registered charge will be higher. As the beam counters Z^2 cut is set at around $20 = 4^2 + 2^2$ most of the offtime coming from the ions heavier than helium and about half of the helium off-time should be cut. The length of the beam counters ADCs gate is 120 ns, so only off-time within this period can be registered.

The Z detector signal was split into two differently delayed signals, so called Z and Z delayed signal. Both of these signals were independently digitized. The delay was set such, that both Z and Z delayed signals from the trigger particle will still be within the ADC gate. On the other hand if the off-time particle would come later than ≈ 20 ns from the trigger it would still be registered in Z signal as a $Z^2_{\text{trigger}} + Z^2_{\text{off-time}}$, but within the delayed Z signal it would fall outside of the gate

registering only Z^2_{trigger}. A fig. 27 presents a few of the possible cases. The actual data and the effect of the cut are presented on fig. 28.

Case	Z^2	delayed Z^2	Ratio
1	16	13	1.23
2	17 (16 + 1)	13	1.30
	20 (16 + 4)	13	1.53
3	17 (16 + 1)	14 (13 + 1)	1.21
	20 (16 + 4)	17 (13 + 4)	1.17
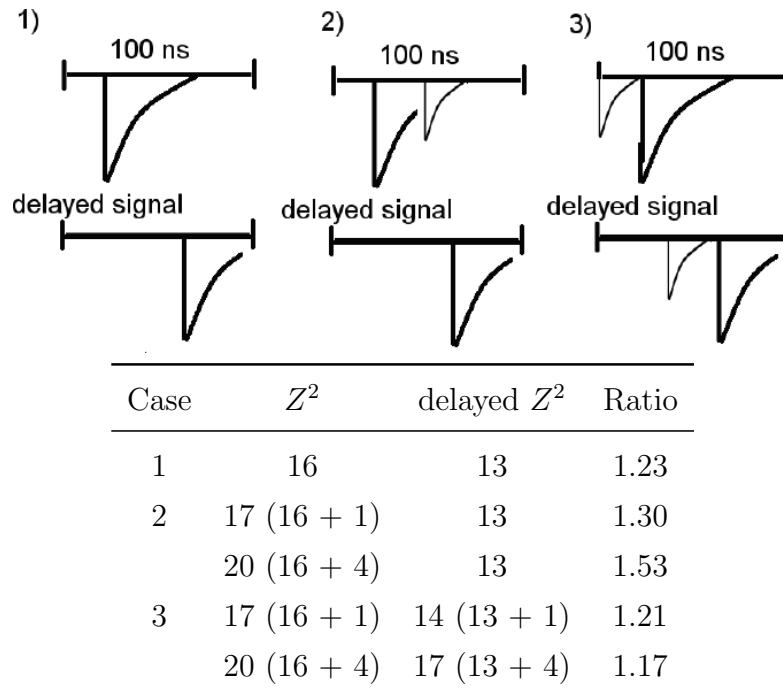
Figure 27: The principle of removing off-time with a delayed Z detector signal. Three cases are shown. First, without off-time particle, second, with off-time after trigger particle, and third, with off-time before trigger particle. The third case is not realized due to the presence of so called Fast Clear protection, which discards triggers with off-time particle up to the $1\,\mu s$ before.

7.3.4. BPD cluster width cut

Another possibility to remove off-time particles within 120 ns is to use signal from the BPDs. The integration time of the BPDs is approximately 300 ns, which would allow to distinguish particles within this time-frame. During beam track reconstruction events with two or more particles hitting any BPD are automatically discarded, although good spatial separation of clusters are necessary for it to work.
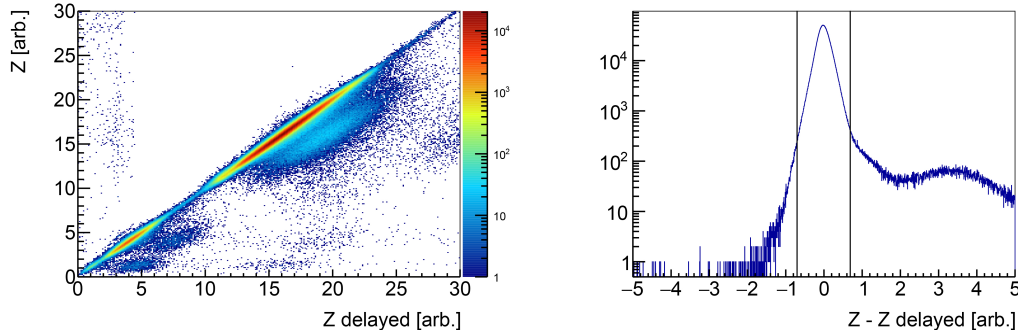
Figure 28: Correlation between the Z detector signal and the delayed Z detector signal *(left)*. Difference between the Z detector and the delayed Z detector signal. The peak around 4 correspond to the helium off-time particles, the enhancement around 1 correspond to the deuterium off-time particles. Cut values are represented as the vertical lines *(right)*.

Further removal of the off-time can be achieved by looking into the width of the cluster. Thanks to long integration time of BPDs there is a time overlap with the MHTDC. By plotting the BPD cluster width as a function of the MHTDC time of closest off-time particle (fig. 29) more events with larger width are visible for off-time within integration time of the BPDs. Unfortunately, there is no good separation between events with and without off-time particle. A cut which would reject any significant amount of events with close off-time particle would also reject many good events. Due to this lack of strong separation this cut will not be used in any of the following analyses.

7.3.5. Beam position cuts

To ensure beam with a good quality a set of cuts for the beam position on various beam detectors was applied. These cuts are most important at low beam momenta, where the beam size is relatively large.

To reliably extrapolate the beam track to the target position a good position measurement by the BPDs are necessary. To ensure good beam track fit near the
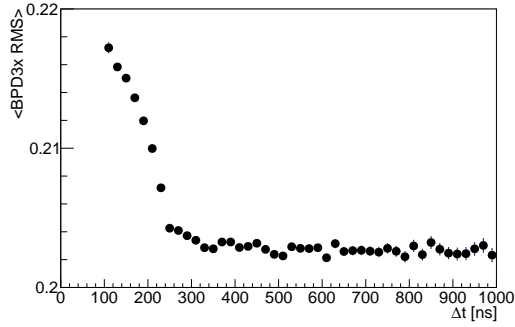
Figure 29: Average width of the BPD3 cluster as a function of the arrival time of the off-time particle. An enhancement is visible for times shorter than the integration time of the BPD detector. Due to the large variations of the width of the BPDs clusters and relatively small enhancement of the width by the off-time particles an efficient cut would cut a lot of data without off-time.

target a requirement of well measured cluster in both (X and Y) planes of the BPD3 was imposed. Additionally, requirement of well measured clusters in one other X plane of the BPDs and one other Y plane of the BPDs is necessary for the beam track fit to succeed.

Additional cuts to remove events where the beam missed some of the beam counters (e.g. at low momenta there are some beams that hit a PMT photocatode of the S1 detector). An example set of the beam position plots is presented on fig. 30.

44
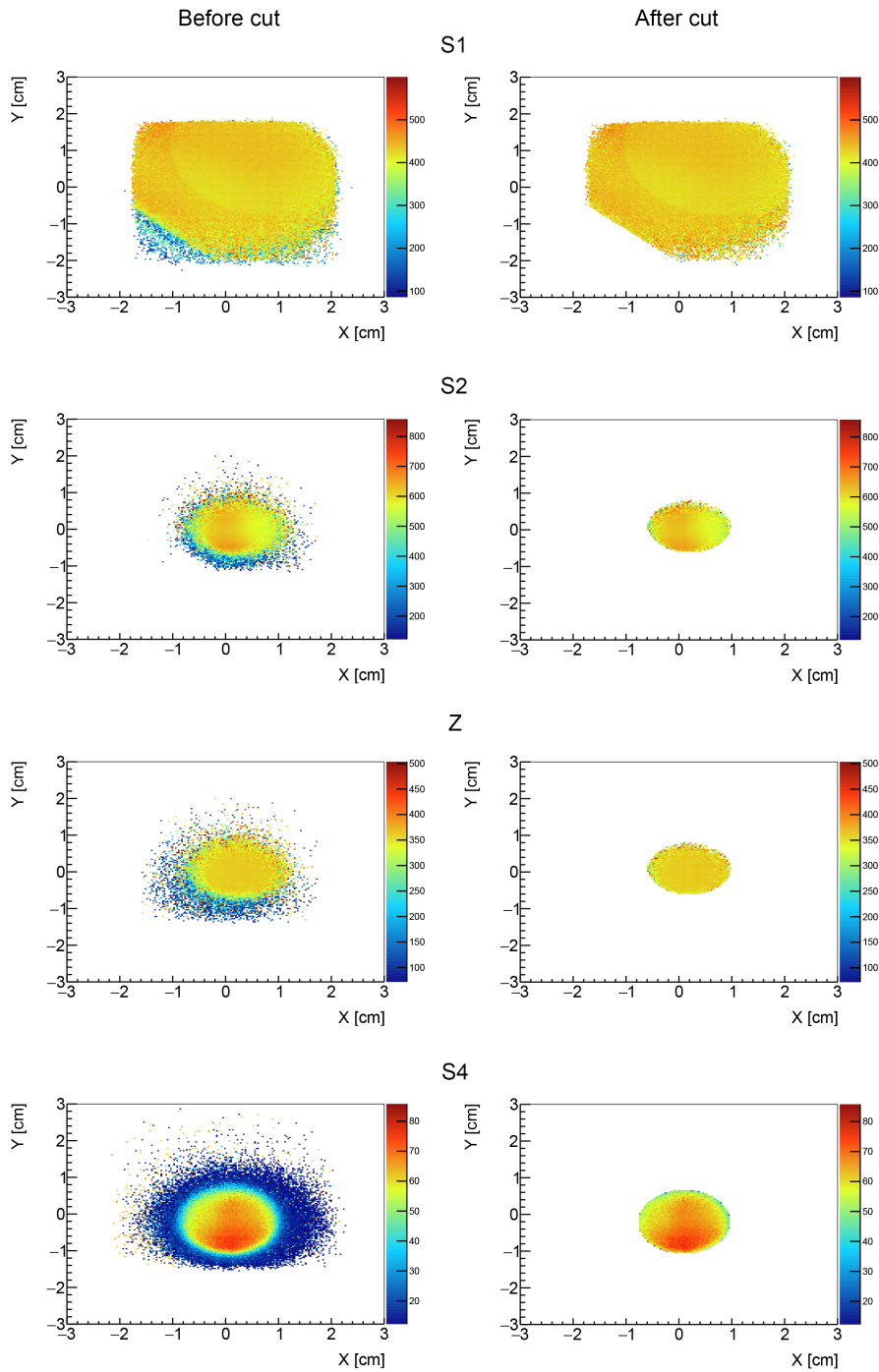
Figure 30: Beam position cuts, 13A GeV/c beam momentum. The color scale represent an average ADC value form the beam and trigger detector for a given beam position. Left column shows data before the cut. Right column shows data after the cut. Outline of the beam and trigger detectors can be seen as a large values of the average ADCs.

7.4. Biasing cuts

The biasing cuts used for following analyses are designed to remove background interactions, while retaining as much as possible of the interactions within the target.

7.4.1. Primary vertex cuts

The reconstruction software tries to fit tracks measured within the TPCs to the common interaction vertex placed along the beam track extrapolated from the BPDs measurement. If this fit fails a differentiation between the primary, secondary and background tracks would not be possible. Thus, the first biasing cuts are the requirement of the primary vertex existence and a good fit quality.

The primary vertex position in XY plane is determined from the BPDs measurements and the beam track extrapolation. The Z position (along the beamline) of the primary vertex is fitted from the TPCs tracks. The next biasing cut reject interactions that did not happened in the target. The beam transverse some material around the target (e.g. BPD3, mylar windows of the target holder, helium and air), any of it could cause background interaction. By cutting on the Z position of the primary vertex such interactions can be minimized.

A histogram of the Z position of the primary vertex can be seen on fig. 32 in both target inserted and removed configurations. Target removed data was normalized to the target inserted data in the region without in-target interactions (from $-500\,\mathrm{cm}$ to $-200\,\mathrm{cm}$). The target position and stardard cut value are marked with vertical lines. The zoomed out histogram of the Z position of the primary vertex with explanation of the orgin of the structures can be seen on fig. 31. The standard value of the cut on primary vertex Z position was set at $\pm 15\,\mathrm{cm}$. This cut value allows to retain most of the in target interactions while rejecting interactions from the target holder exit window.

After the vertex Z position cut there are $\approx 0.35\%$ of the out-of-target interactions
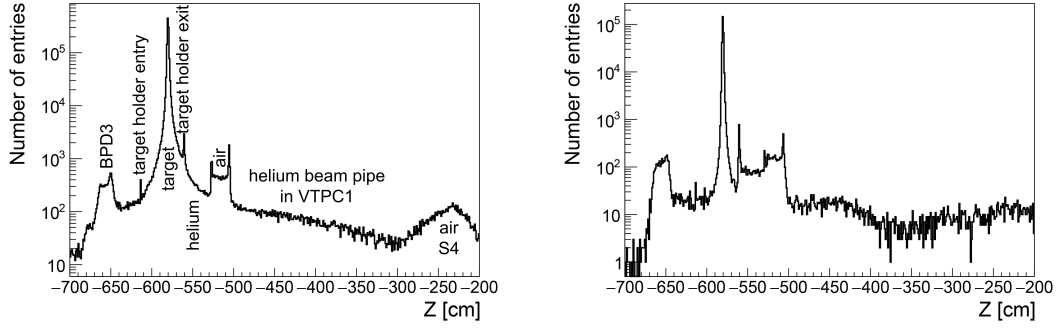
Figure 31: Distribution of the Z coordinate of the primary vertex.
20A GeV/c *(left)*, 150A GeV/c *(right)*.
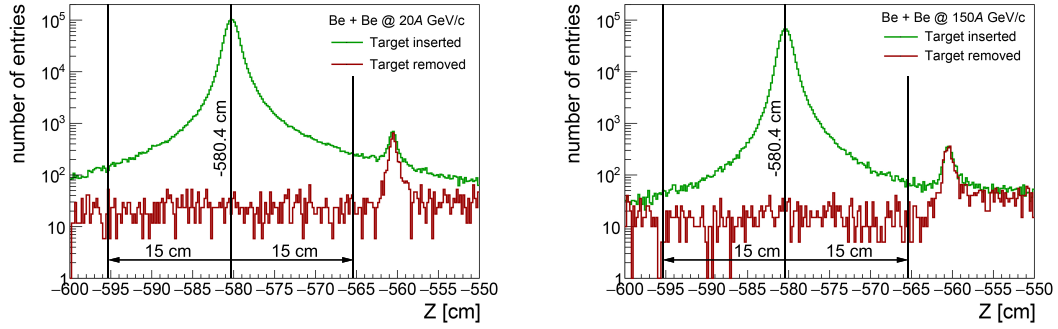
Figure 32: Distribution of the Z coordinate of the primary vertex.
Target position and standard cut value are marked.
20A GeV/c *(left)*, 150A GeV/c *(right)*.

in the target inserted data for all beam momenta. Use of the target removed data to correct for this background interactions is not possible for the differential analyses (e.g. double differential pion spectra) due to the low statistics of the target removed data after all cuts ($\approx$ 1000 events). This bias will be taken into account during systematic error estimation.

On the other hand the vertex Z position cut rejects some of the low multiplicity in-target interactions. The amount of this bias differs for all beam momenta due to its dependence of produced particle multiplicity. To estimate how much in-target

events are lost, normalized target removed distribution of vertex Z position was subtracted from the target inserted distribution. Then integral of the subtracted histogram was calculated outside of the cut region. The results are tabulated in table 4. This bias can be corrected by the Monte-Carlo simulation.

Table 4: Bias due to the vertex Z position cut. The fraction shows how much in-target events were lost due to the cut.

p_{beam} [GeV/c]	Fraction of lost events
$13A$	0.5%
$19A$	0.4%
$30A$	0.3%
$40A$	0.3%
$75A$	0.4%
$150A$	0.2%

7.4.2. Gap TPC interaction cut

At high beam momenta no minimum bias trigger was available. In addition, PSD response to beryllium particles was relatively low (due to particle shower leakage), allowing generation of a central interaction trigger even when no interaction happen. To ensure the interaction took place, all events where there is a beryllium charge registered in the GTPC close to the beam position are removed fig. 33. The value of this cut was set to reject all of the events with the beryllium particle. The amount of such events was calculated for all energies and the results are presented in the second column of table 5. Unfortunately, due to limited charge resolution of the GTPC, this cut removes some of the events with the lithium fragment of the primary interaction. The amount of this bias was estimated by fitting an exponential function to the right side of the lithium peak. This bias was tabulated in the third column of table 5.
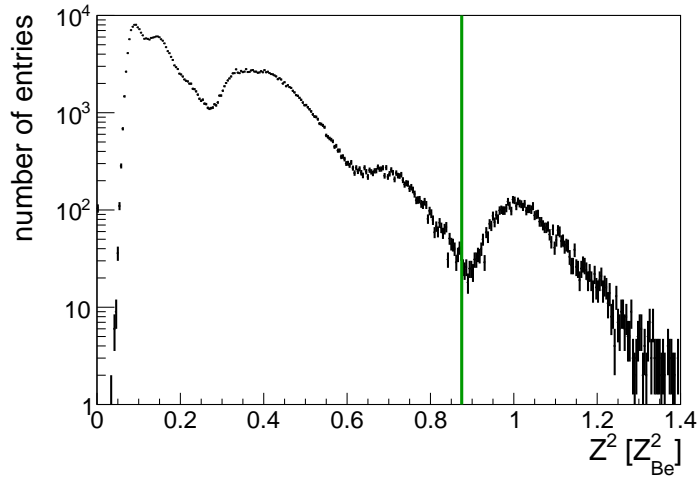
Figure 33: Distribution of the energy loss of tracks in the GTPC. Only central interaction trigger events after all non-biasing cuts and vertex Z position cut are plotted. The green vertical line represents the cut value to exclude non-interacting beryllium (peak around 1) from the interaction data.

Table 5: The amount of biases removed and introduced by the GTPC interaction cut. At low beam momenta there was no beryllium particles in the interaction trigger due to rejection of such events by an on-line S4 cut.

p_{beam} [GeV/c]	$f_{\mathrm{removed}}^{\mathrm{Be\ bias}}$	$f_{\mathrm{introduced}}^{\mathrm{Li\ bias}}$	$\frac{f_{\mathrm{removed}}^{\mathrm{Be\ bias}}}{f_{\mathrm{introduced}}^{\mathrm{Li\ bias}}}$
$13A$		not necessary	
$19A$		not necessary	
$30A$		not necessary	
$40A$	1.44%	0.04%	36
$75A$	1.41%	0.10%	14.1
$150A$	0.61%	0.17%	3.6

7.4.3. Centrality selection

A cut to select most central events based on the PSD energy is also considered a biasing cut. It will be explained further within the next chapters of this work.

7.5. Software library design

While the biasing cuts can change from analysis to analysis depending on the susceptibility of a given analysis to various biases, the non–biasing cuts which select a pure, well measured beam particle without off–time particles should be constant between different analyses.

An easy to use C++ class contained within header library was developed to facilitate use of these cuts even by users not familiar with the advanced programming concepts.

To include the library within an analysis program user have to only include the library header file:

#include <UpstreamEventCutsBe.h>

To setup the class user has to write:

```
// the path to the calibration constants of the beam detectors
UpstreamEventCutsBe upstreamEventCutter("./Calibration");
```

To reject an event that do not pass the cuts following code has to be used:

```
if (!upstreamEventCutter.IsEventGood(event))
  continue;
```

8. Cross section determination

The total cross section for the interaction of a beryllium beam on a beryllium target can be divided into two parts: an inelastic cross section and elastic cross section.

$$\sigma_{\text{tot}} = \sigma_{\text{inel}} + \sigma_{\text{el}}$$

Inelastic cross section is a cross section for the processes where the initial state particles are different than the final state particles. It includes not only the cross section for production of new particles but also the cross section for fragmentation of either beam or target nucleus.

Elastic cross section is defined as a cross section for a process where initial and final state particles are the same.

Inelastic cross section have contributions due to electromagnetic and strong processes. We are unable to distinguish them experimentally, although simulations and data extrapolation show that for ^{7}Be $+ {}^{9}$Be at SPS energies cross section due to electromagnetic processes is around 50 times smaller than due to strong processes.

$$\sigma_{\text{inel}}^{\text{em}} = 2\% \cdot \sigma_{\text{inel}}^{strong}$$

Inelastic cross section can be further divided into two parts: quasi-elastic cross section and production cross section.

Quasi-elastic cross section involve processes where either target, projectile or both are fragmented but no additional hadrons were produced. It is difficult to measure target fragmentation in the fixed target experiments, therefore, projectile fragmentation cross section was measured. Such simplification was also employed by the only other measurement of the inelastic ^{7}Be $+ {}^{9}$Be cross section [8].

Production cross section involve processes where new hadrons are produced in the final state.

$$\sigma_{\text{inel}} = \sigma_{\text{prod}} + \sigma_{\text{qe}}$$

The interaction probability, defined as a ratio between the beam particles that interacted to all beam particles, can be rewritten as cross section according to the formula:

$$\sigma = \frac{1}{\rho L N_{\mathrm{A}}/A} P_{\mathrm{int}}, \tag{1}$$

where ρ is the target density, L the target length, N_{A} the Avogadro constant, A the atomic number of the target, and P_{int} probability of interaction in the target.

A beam undergoes exponential attenuation as it interacts within the target. Therefore, at the downstream face of target there is less beam particles than at the upstream face of the target. This attenuation can be taken into account in eq. (1) by exchanging the real target length by the effective target length given by the equation:

$$L_{\mathrm{eff}} = \lambda_{\mathrm{abs}}(1 - e^{-L/\lambda_{\mathrm{abs}}}) \tag{2}$$

with the absorption length

$$\lambda_{\mathrm{abs}} = \frac{A}{\rho N_{\mathrm{A}} \sigma}. \tag{3}$$

By substituting an effective target length (eq. (2)) in place of the real target length in the eq. (1), an iterative procedure is obtained (the absorption length, eq. (3) contains value of cross section):

$$\sigma_i = \frac{P_{\mathrm{int}} \cdot \sigma_{i-1}}{1 - \exp\left(-L\rho N_{\mathrm{A}}\sigma_{i-1}/A\right)} \tag{4}$$

Most of the results of this chapter will be expressed as the probabilities of interaction. The conversion to the cross section will be performed as a last step to obtain final results.

All of the analysis in this section was done on the data taken with identified beam trigger ($\approx 10\%$ of total recorded statistics) and all of the non-biasing cuts were applied to obtain pure beryllium beam without the off-time particles.

As can be seen from eq. (1) the cross section depends on the target properties. The target properties were measured with finite precision. Therefore, the target properties systematic uncertainties will propagate to the cross section measurement.

The atomic composition of target was measured with Wavelength Dispersive X-Ray Fluorescence (WDXRF) method in Jan Kochanowski University in Kielce, Poland. The results of the measurement are presented in the table 6.

Table 6: WDXRF measurements of the atomic composition of the beryllium target. Weighted mass number is the mass number of an isotope weighted by its amount within target.

Isotope	Amount[%]	Weighted mass number
^{9}Be	99.6200	8.9658
^{16}O	0.0905	0.0145
^{24}Mg	0.0414	0.0099
^{27}Al	0.0413	0.0112
^{32}S	0.0032	0.0010
^{45}Sc	0.0005	0.0002
^{48}Ti	0.0151	0.0072
^{51}V	0.0013	0.0007
^{55}Mn	0.0258	0.0142
^{56}Fe	0.1200	0.0672
^{59}Ni	0.0151	0.0089
^{60}Co	0.0024	0.0014
^{64}Cu	0.0077	0.0049
^{65}Zn	0.0085	0.0055
^{184}W	0.0030	0.0055
^{238}U	0.0063	0.0150
Sum	100.0021	9.1332

The results of the cross section measurement were corrected for target contamination by the following procedure.

An assumption that the cross section scales with $\sqrt{A_{\text{targ}}^{2/3} + A_{\text{proj}}^{2/3}}$ was made as the simplest possible model. The correction factor for the probability of interaction

was calculated according to the equation:

$$c = \frac{\sqrt{9^{2/3} + A_{\text{proj}}^{2/3}}}{\sqrt{\langle A_{\text{targ}}^{2/3} \rangle + A_{\text{proj}}^{2/3}}} \cdot f,$$

where c is the multiplicative correction factor, $A_{\text{proj}}^{2/3}$ is the mass number of the projectile, $\langle A_{\text{targ}}^{2/3} \rangle$ is the sum of the weighted mass numbers of the target components, and f is the fraction of the beryllium in the target. The procedure is not analytically correct, but the MC simulations indicate an error of less than a per mile. To account for unknown errors of the composition measurements, as well as simplified procedure a 10% of the correction will be treated as a systematic error.

The value of the correction factor due to impurities in the target is 0.7% for all beam momenta. The systematic error corresponding to this correction are set to 0.1%.

The length of the target was measured with 0.3 mm precision. Propagating this error to the cross section value gives systematic error of 2.5% for all beam momenta. For most beam momenta and measurements this is the dominant source of error.

The density of the target was measured with 0.5% precision. Such precision translate to 0.4% systematic error of the cross section measurement.

The total systematic error related to the target properties measurement is equal to $\pm 2.6\%$ for all beam momenta and cross section measurements. This error is fully correlated for all beam momenta.

8.1. Production cross section

The production cross section of ^{7}Be + ^{9}Be collisions were determined by the measurement of the multiplicity distribution of the newly produced particles in the large TPCs acceptance. Despite a large acceptance of the NA61/SHINE TPCs a correction for experimental biases (mostly loss of the low multiplicity events) have to be applied.

The correction was calculated based on the standard NA61/SHINE simulation chain. The CRMC 1.55 EPOS 1.99 [26–28] was used as a primary interaction generator. EPOS generator proved [29] to describe interactions at the SPS energy range reasonably well. The output of the EPOS model was passed through a detailed detector simulation based on the GEANT3 [30] framework. Such simulated data was then reconstructed using the same reconstruction chain as for the experimental data.

8.1.1. Data selection

To select clean data sample for cross section analysis both non-biasing as well as biasing cuts described in section 7 were used. In addition to event cuts the track cuts had to be used to obtain minimally biased multiplicity distribution. For this analysis precise information about track parameters, i.e. momentum or particle type, is not needed, therefore track quality cuts can be quite loose.

List of the track quality cuts used:

- well fitted to primary interaction vertex,

- > 10 clusters in the Vertex TPCs (out of maximally 144 clusters),

- distance of the closest approach of the track to the vertex in x (b_{x}) and y (b_{y}): $|b_{\mathrm{x}}| < 4\,\mathrm{cm}$ and $|b_{\mathrm{y}}| < 2\,\mathrm{cm}$.

Additionally, a requirement of at least one positively charged track in an event was imposed. Such restriction rejected events where only delta electrons were produced. Events where only projectile fragmentation occurred and no new particles were produced do not fit this requirement as well, as the possible phase space of the fragmentation products places them outside of the Vertex TPCs acceptance.

8.1.2. Procedure

To calculate probability of the new particle production, first a "raw" trigger probability of production was calculated as:

$$p_{\text{prod}}^{\text{raw}} = \frac{N_{\text{sel}}^{\text{data}}}{N_{\text{beam}}^{\text{data}}}, \tag{5}$$

where $N_{\text{sel}}^{\text{data}}$ is the number of reconstructed beam and interaction events after all cuts (the cuts select only events with particle production) and $N_{\text{beam}}^{\text{data}}$ is the total number of registered beam and interaction events. Both nominator and denominator events were filtered through non-biasing cuts, as they do not change an interaction probability, but only select the well defined beams.

The correction factor was calculated from the Monte-Carlo simulations in a following way:

$$c_{\text{MC}} = \frac{N_{\text{sel}}^{MC}}{N_{\text{gen}}^{\text{MC}}}, \tag{6}$$

where N_{sel}^{MC} is the number of reconstructed events after all cuts and $N_{\text{gen}}^{\text{MC}}$ is the total number of generated events. The EPOS generator generates only production events, therefore this ratio shows the rejection rate of the good production events.

The final result is determined as:

$$p_{\text{prod}} = p_{\text{prod}}^{\text{raw}}/c_{\text{MC}}. \tag{7}$$

8.1.3. Simulation quality

The quality of the Monte-Carlo simulation, as well as the amount of bias introduced by the cuts selecting only production events were tested in various ways.

A test of the cuts biases can be performed by plotting multiplicity distribution from generated MC events together with multiplicity distribution from MC events selected by all cuts. On fig. 34 a bias in multiplicity lower than 4 can be seen.

To test how well multiplicity distribution from simulation reflects data, the multiplicity distribution of data and MC were plotted after all cuts, fig. 35. The
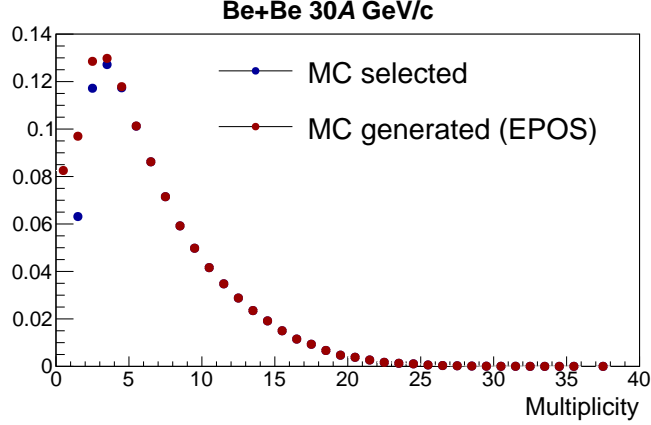
Figure 34: Example distribution of the multiplicity of particles measured by the TPCs from the minimum bias MC simulation. Red points show unbiased, generated distribution. Blue points show distribution of the simulated data after the reconstruction and all cuts. Events where no particles crossed active volume of the TPCs are cut out by definition, only red point is visible for them. Above the multiplicity of 4 particles no bias is visible.

minimum bias EPOS simulation gives $\approx 10\%$ highrt mean multiplicity than data: $\langle n_{\mathrm{MC}} \rangle = 6.4 > \langle n_{\mathrm{data}} \rangle = 5.9$. This discrepancy will cause bias in the correction factor, since the low multiplicity events, where the reconstruction and cuts bias the data, will be misrepresented.

The effect of the discrepancy between multiplicity distribution of data and MC have to be studied in more detail to determine systematic bias related to MC correction factor determination. A plot of the final probability of production as a function of rising multiplicity cut was plotted on fig. 36. To obtain this plot the analysis was repeated with different values of multiplicity cut applied both for data and MC (standard multiplicity cut is a requirement of at least one positive particle). The result changes with rising the value of the cut. Extrapolation of the trend to multiplicity cut $n = 0$ gives possible bias which is tabulated in table 7. This value will be treated as a model systematic error of the results.
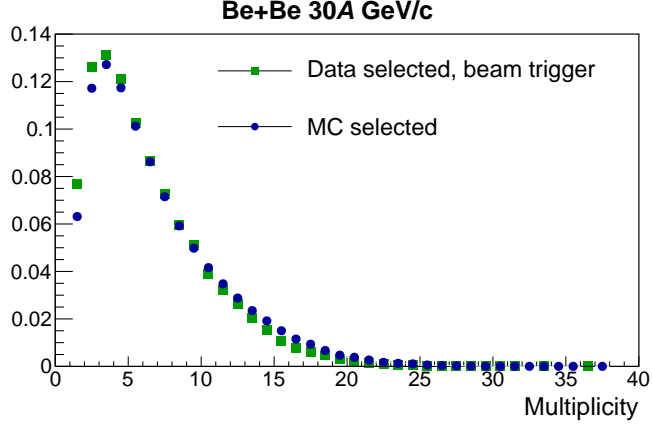
Figure 35: Example distribution of the multiplicity of particles measured by the TPCs. Only data after reconstruction and all cuts are plotted. Blue points show the distribution of the simulated data. Green points show the distribution of the experimental data. Events where no particles crossed active volume of the TPCs are cut out by definition. The higher particle multiplicity of the simulated data is visible.

Table 7: Magnitude of the model systematic error of the production cross section measurement. Lower values at high beam momenta can be explained by a higher mean multiplicity of produced particles. A reconstruction and cuts bias is located mostly at the low multiplicity events.

p_{beam} [GeV/c]	Systematic error
19A	2.2%
30A	1.3%
40A	0.6%
75A	0.6%
150A	0.1%
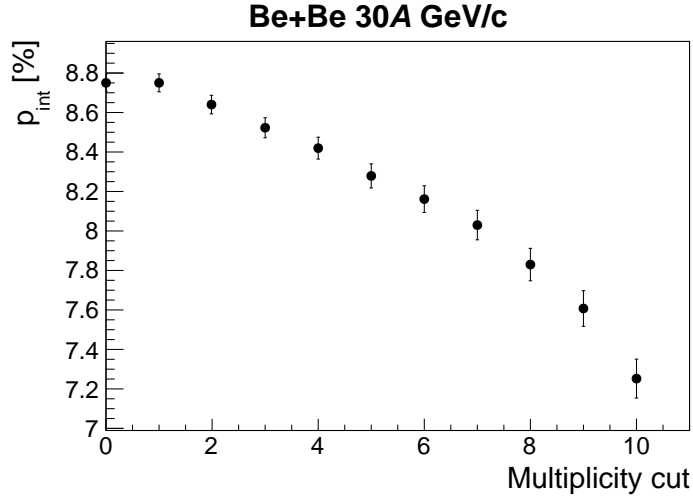
Figure 36: Example probability of production interaction as a function of rising particle multiplicity cut. Due to different shape of the multiplicity distribution in data and simulation, a lack of stability is visible. The difference between extrapolation of the visible trend to the multiplicity of 0 and the measured p_{int} with standard cuts will be treated as a model systematic error.

8.1.4. Result stability crosschecks

Stability crosschecks of the final result with respect to various beam parameters were carried out. These crosschecks allow to recognize possible biases and calculate systematic errors. The procedure consists of calculating final probability of production p_{prod} in disjoint subset of events defined by some parameter. If the result in all subsets will give the same value up to the statistical error ($\chi^2/\text{ndf} \approx 1$) the result is stable and no systematic error have to be assigned due to the change in studied parameter.

The first stability check was carried out as a function of beam position. The data was divided into subsets differing by the beam position on the target. A concentric rings with outer and inner radius difference of $\Delta r = 0.1$ cm was chosen, see fig. 37. The result appear stable with respect to beam position on target (fig. 38), therefore

no systematic error was assigned.
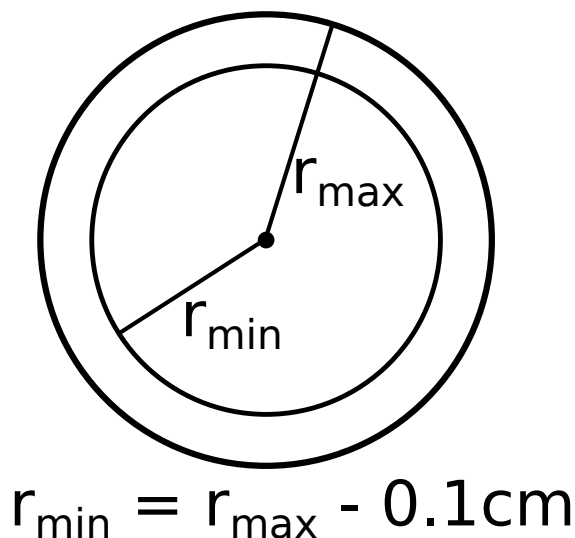
Figure 37: Data selection scheme for the beam position stability check of the production cross section. The data was binned in the mutually exclusive concentric rings centered at the middle of the beam spot.

The second stability check involved off-time beam particles. The data was divided into disjoint subsets by the arrival time of the closest off-time beam particle. The result was plotted on fig. 39. While the result do not depend on existence of the off-time particle later than $\approx 4.5\,\mu s$, there is a strong dependence on the arrival time of the closest off-time on shorter timescales. Since MHTDC cut do not bias the data, the events with off-time closer than $\approx 4.5\,\mu s$ can be simply removed.

Unfortunately, MHTDC cannot measure off-time in the $0 — 120\,\mu s$ after the trigger. While most of this off-time is probably rejected by other time structure cuts, it is difficult to estimate how much. An assumption of not removing off-time close to the trigger particle is adopted as a conservative estimate of the systematic error.

With the beam intensity of 100k particles on S1, according to the time structure of the beryllium beam without any implicit debunching, assuming that number of particles per bunch are independent and distributed with Poisson distribution, there is a 6% probability of off-time that we cannot measure and 26% probability
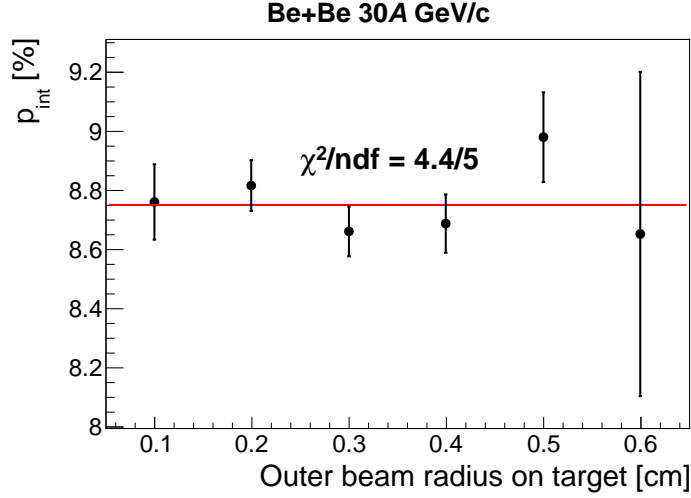
Figure 38: The results of the beam position stability check of the production cross section. The probability of production was calculated for various position of the beam. The statistical errors are uncorrelated. No instability is visible.

of off-time in 200 — 320 ns time window. A real probability (including implicit debunching) can be calculated from MHTDC time spectrum of data:

$$p_{\text{off-time}}(0-120\text{ns}) = \frac{6\%}{26\%} p_{\text{off-time}}(200-320\text{ns}).$$

The maximum possible bias due to off-time can then be calculated according to the equation:

$$\Delta p_{\text{prod}} = \left(p_{\text{prod}} - \frac{p_{\text{prod}} - p_{\text{prod}}(120\text{ns}) \cdot p_{\text{off-time}}}{1 - p_{\text{off-time}}} \right) / p_{\text{prod}},$$

where p_{prod} is the measured probability of production, Δp_{prod} is the maximum possible bias due to off-time, $p_{\text{prod}}(120\text{ns})$ is the probability of production with the requirement of the off-time within 120 ns, and $p_{\text{off-time}}$ is the probability of off-time within 120 ns from the trigger particle.

This equation connects unmeasured effect of off-time within 120 ns from the trigger particle to the effect of off-time in the 200 — 320 ns range.

The maximum possible bias for all analyzed beam momenta is presented in table 8.
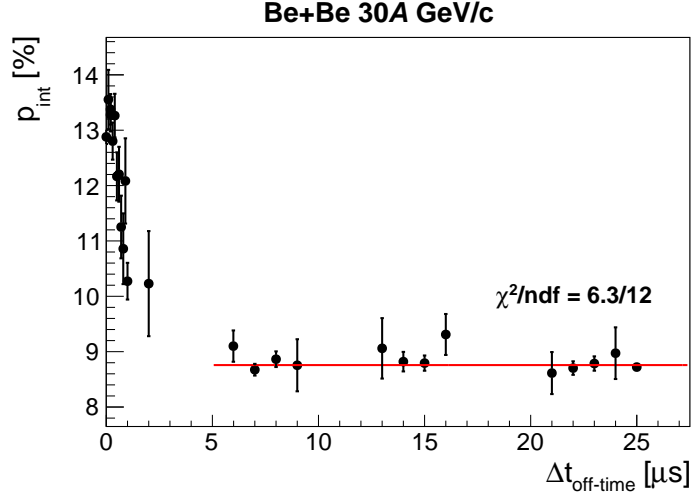
Figure 39: The results of the off-time particles stability check of the production cross section. The probability of production was calculated in disjoint event sets selected by the arrival time of the closest off-time particle. The results are stable for off-time particles arriving later than 4.5 μs from the trigger particles. For events with the off-time particles closer to the trigger particle than 4.5 μs an increase of the probability of production is visible. This increase is caused by the particles produced in off-time interaction being fitted to the primary vertex, rising the apparent multiplicity of the collision.

Table 8: Maximum possible bias due to off-time interactions for probability of production.

p_{beam} [GeV/c]	Maximum possible bias
19A	0.3%
30A	0.4%
40A	0.4%
75A	0.5%
150A	0.8%

8.1.5. Results

The "raw" trigger production probabilities and MC correction factors together
with their statistical uncertainties are plotted in fig. 40.
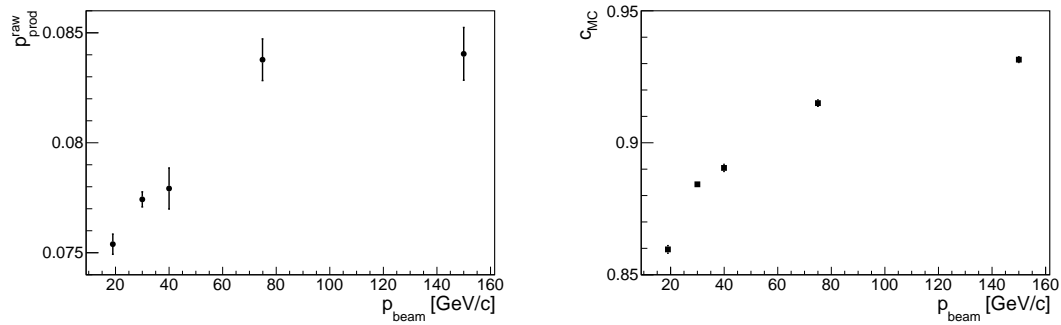
Figure 40: *(left):* Raw probability of production — eq. (5),
(right): MC correction factor — eq. (6).

The final result recalculated from the probability of production to the production
cross section with the help of eq. (4) can be seen on fig. 41.

A table with the results of the production $^{7}Be + {}^{9}Be$ cross section measurement
together with the values of the statistical and systematic errors can be seen in
table 9.
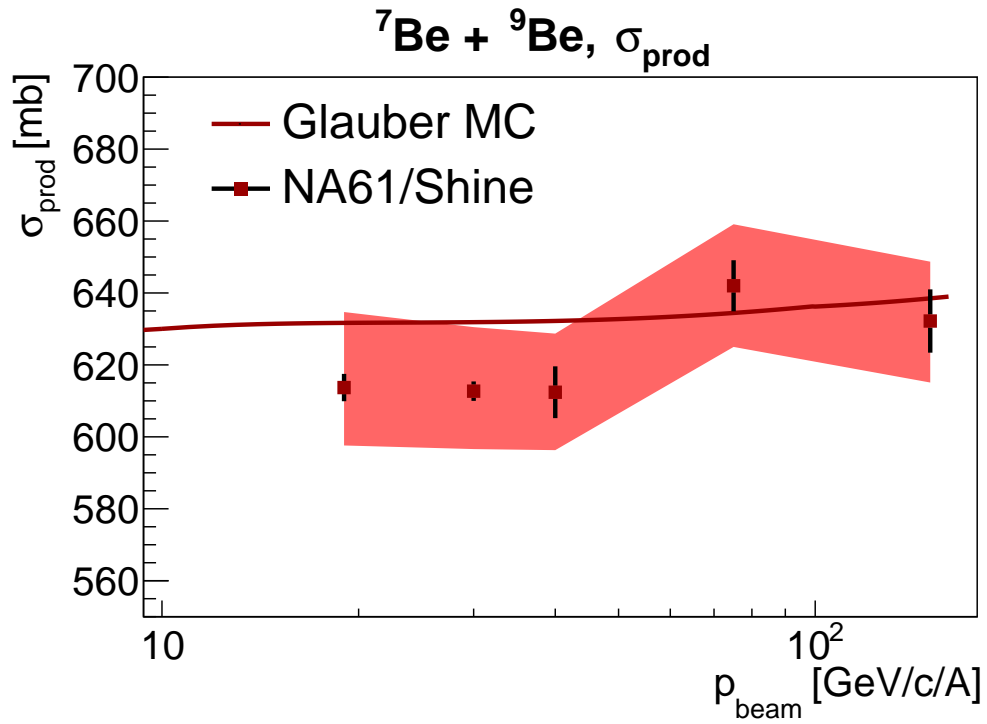
Figure 41: Production cross section in ^{7}Be + ^{9}Be interactions as a function of the beam momentum. Statistical errer is marked with the error bars. Systematic error is marked with the band. The line represents Glauber Monte-Carlo calculation within the Geant4 model.

Table 9: Production cross section of ^{7}Be + ^{9}Be interactions. The results are presented using following convention: result $\pm$ statistical error $\pm$ systematic error related to MC model (model) $\pm$ systematic error related to off-time interactions (off-time) $\pm$ systematic error related to the uncertainty of the target parameters (target).

p_{beam} [GeV/c]	σ_{prod} [mb]	stat. error	total sys. error
$19A$	$613.7 \pm 3.8 + 13.6^{\mathrm{model}} - 1.9^{\mathrm{off\text{-}time}} \pm 16.0^{\mathrm{target}}$	0.6%	3.4%
$30A$	$612.7 \pm 2.7 + 8.1^{\mathrm{model}} - 2.6^{\mathrm{off\text{-}time}} \pm 15.9^{\mathrm{target}}$	0.5%	2.9%
$40A$	$612.4 \pm 7.2 + 3.7^{\mathrm{model}} - 2.4^{\mathrm{off\text{-}time}} \pm 15.9^{\mathrm{target}}$	1.2%	2.7%
$75A$	$642.0 \pm 7.1 + 3.9^{\mathrm{model}} - 3.1^{\mathrm{off\text{-}time}} \pm 16.7^{\mathrm{target}}$	1.1%	2.7%
$150A$	$632.2 \pm 8.8 + 0.7^{\mathrm{model}} - 4.8^{\mathrm{off\text{-}time}} \pm 16.4^{\mathrm{target}}$	1.4%	2.7%

8.2. Inelastic cross section

Inelastic cross section in ^{7}Be + ^{9}Be was determined by using the charge measurements of the Gap TPC, and at the low beam momenta, the S4 scintillator. Both Gap TPC, as well as the S4 provide satisfactory charge resolution to distinguish between beryllium and lower charges. While inelastic cross section include processes that fragments only target nuclei, measurement of such reaction is very difficult. The only other existing measurement of the ^{7}Be + ^{9}Be inelastic cross section [8] define inelastic cross section as a cross section for fragmentation of the projectile. This work will follow this convention.

The measurement of the cross section carried out by NA61/SHINE are sensitive only to the fragmentation where the charge of the projectile change. Fortunately, when ^{7}Be fragments to ^{6}Be or ^{5}Be the lifetime of such fragmentation products are extremely short. Decay modes and lifetimes of beryllium isotopes can be found in table 10 [31].

Table 10: Table of the beryllium isotopes that are possible to encounter during ^{7}Be + ^{9}Be collisions. Decay modes, lifetimes and distance travel by a particle within its lifetime assuming speed of light are presented. Projectile (^{7}Be) fragmentation can produce only very short-lived isotopes which will decay before the detector.

Isotope	Decay mode	Half-life	Traveled distance
^{5}Be	^{5}Be $\to$ ^{4}Li + p	≈ 0	≈ 0
^{6}Be	^{6}Be $\to$ ^{4}He + 2p	5.0×10^{-21} s	1.5 pm
^{7}Be	^{7}Be + e $\to$ ^{7}Li	53.22 d	1.3×10^{12} km
^{8}Be	^{8}Be $\to$ 2α	6.7×10^{-17} s	20 nm
^{9}Be		stable	

Thanks to the short decay time of the isotopes of beryllium with $A < 7$, the measurement of the projectile charge after the target is enough to measure the projectile fragmentation cross section.

66

8.2.1. Procedure

For this analysis only non-biasing cuts can be used. The fragmentation of the Beryllium projectile can happen without any particles being deflected into the acceptance of the large volume TPCs, making a primary vertex fit impossible to succeed. Because of the inability to perform background suppressing biasing cuts, the background have to be handled in another way. To correct for the background of interactions outside of the target, the analysis is performed separately for target inserted and target removed configuration. Then final probability of interaction is calculated according to the following equation:

$$p_{\text{int}}^{\text{target}} = \frac{p_{\text{int}}^{\text{inserted}} - p_{\text{int}}^{\text{removed}}}{1 - p_{\text{int}}^{\text{removed}}}, \tag{8}$$

where $p_{\text{int}}^{\text{target}}$ is the probability of interaction inside the target, $p_{\text{int}}^{\text{inserted}}$ is the probability of interaction in the target inserted configuration (which includes in-target interactions and out-of-target interactions), $p_{\text{int}}^{\text{removed}}$ is the probability of interaction in the target removed configuration, and the denominator is related to the change of the normalization due to the beam attenuation in the target [32].

8.2.2. The S4 method

The S4 detector response is proportional to the sum of the squared charge of the particles passing through the scintillator during the integration time. Therefore, to calculate inelastic cross section a fraction of the events which correspond to the lower Z^2 than that of Beryllium need to be analysed. Example spectrum of the S4 detector can be seen on fig. 42. Unfortunately, there are two effects that make the procedure more difficult.

First, the limited charge resolution of the detector cause the tails of the peaks from the various charges overlap. To correctly select the range of the non-interacting beryllium the probability of interaction is calculated for all bins of the S4 spectrum. Then, the probabilities of interaction in target inserted, removed and in-target (eq. (8)) configuration is plotted (fig. 43). As a final result a probability of interaction
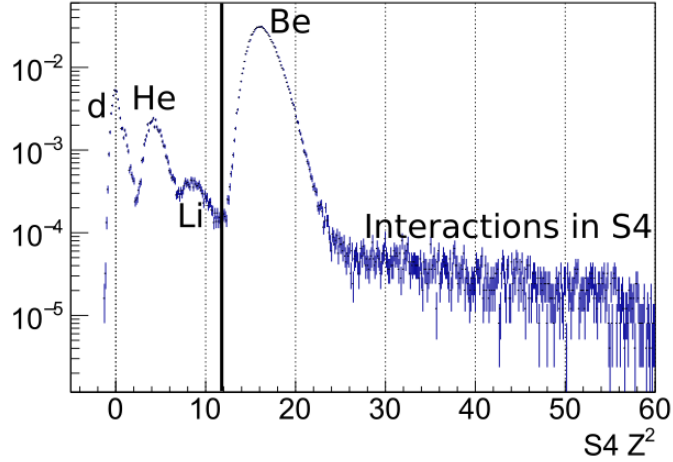
Figure 42: Squared charge measured by the S4 detector. A cut to reject the beryllium particles was plotted as a vertical line. The long tail of the distribution at high Z^2 is the result of the interactions in the S4 detector.

just before the large fluctuations related to the subtraction of the beryllium peak is chosen. The variation of the result in proximity to the chosen value is selected as a systematic error. The procedure is shown on fig. 43.

The second effect is the interaction in the S4. Due to a rather large interaction length of the S4, there is $\approx 2.5\%$ probability of a helium ion (which is most frequent fragment of a beryllium interaction) interacting in the S4. Such interaction can cause a large signal from the detector. A minimum ionizing particles produced from the projectile will increase the signal by 1 per each particle. If 16 particles are produced, they would leave the signal equal to the beryllium ion. A low momenta particles from the S4 ions will be completely stopped within the S4 converting most of their energy into the S4 signal.

A beryllium particle with the energy of $80\,\text{GeV}$ passing through the S4 ($5\,\text{mm}$ plastic scintillator) loses $\approx 20\,\text{MeV}$ of its energy [33]. An interaction inside S4 that knocked off one nucleon form the detector material with the Fermi energy of $\approx 200\,\text{MeV}$ would give ten times higher signal in the detector than a passing beryllium beam

68
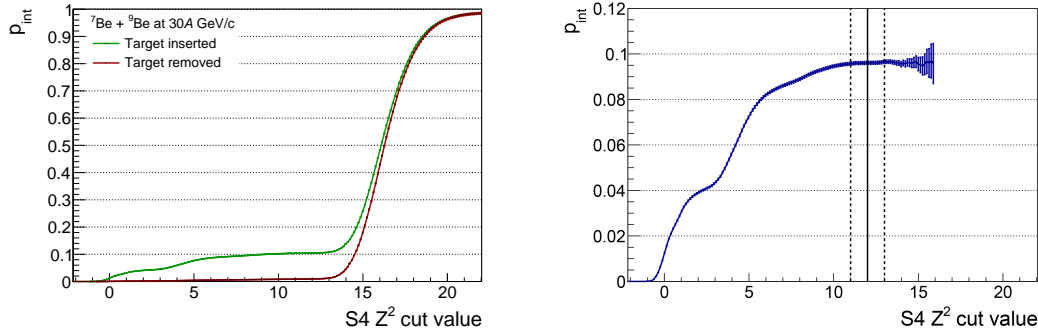
Figure 43: Probability of interaction as a function of where the cut for non-interacting beryllium particles is placed.

On the left, a probability of interaction in the target inserted and removed configuration is plotted. A rapid increase around Z^2 correspond to counting beryllium beam particles as interactions.

On the right, a probability of interaction after out-of-target background subtraction is plotted. A value of the cut for which final result is obtained is marked as a solid vertical line. The systematic error of the method is estimated based on the values marked with dashed vertical lines.

particle. A cut from above the beryllium peak can be made. However, the beryllium beam particles also interact with the S4. Therefore, applying such cut would cause some of the non-interacting events to be treated as interactions.

The result of this effect can be seen on the S4 spectrum (fig. 42) as a long tail in high values of Z^2. The probability of such interactions can be estimated by integrating the tail and extrapolating the effect back to the beryllium peak. If all of such events would result of mislabelling an interaction event as non-interacting, the cross section would change by -0.5%. This value is included as a systematic error of the measurement.

The results of the interaction cross section measurement with the S4 detector can be found in table 11.

Table 11: Inelastic cross section of ^{7}Be + ^{9}Be interaction. The S4 method results are presented. The results are presented using following convention: result $\pm$ statistical error $\pm$ systematic error related to the uncertainty of defining charge of the measured particle (method) $\pm$ systematic error related to interactions within the S4 (S4 bias) $\pm$ systematic error related to the uncertainty of the target parameters (target).

p_{beam} [GeV/c]	$p_{\text{int}}^{\text{inel}}$ [%]	σ_{inel} [mb]	stat. error	total sys. error
$13A$	10.01 ± 0.18	$705 \pm 12 \pm^{+7}_{-11}$ method $+ 4^{\text{S4 bias}} \pm 18^{\text{target}}$	1.7%	3.1%
$20A$	9.67 ± 0.09	$680 \pm 6 \pm^{+1}_{-6}$ method $+ 4^{\text{S4 bias}} \pm 18^{\text{target}}$	0.9%	2.7%
$30A$	9.61 ± 0.07	$676 \pm 5 \pm^{+4}_{-7}$ method $+ 4^{\text{S4 bias}} \pm 18^{\text{target}}$	0.7%	2.7%

8.2.3. The GTPC method

The Gap TPC (GTPC) is a tracking detector which supplement the tracking of the very forward particles. The maximum number of clusters registered in GTPC is 7, which in itself is not enough to provide good track parameter estimation, in most analysis the GTPC clusters supplement clusters from the MTPCs giving more precise momentum determination. The energy loss in the GTPC is registered, although due to its low number of clusters and large momentum of the particles passing through it, the energy loss is not calibrated. Fortunately, even this un-calibrated data is enough to differentiate between particles with different charge. An example spectrum of the energy loss of all particles in the GTPC is shown on fig. 44.

If an interaction took place there should not be a track with energy loss corresponding to beryllium energy loss in the GTPC. To find a probable beryllium beam tracks in the GTPC following cuts were made:

- The (x, y) position of the track at the middle of the GTPC should be within 10 cm from the beam spot,
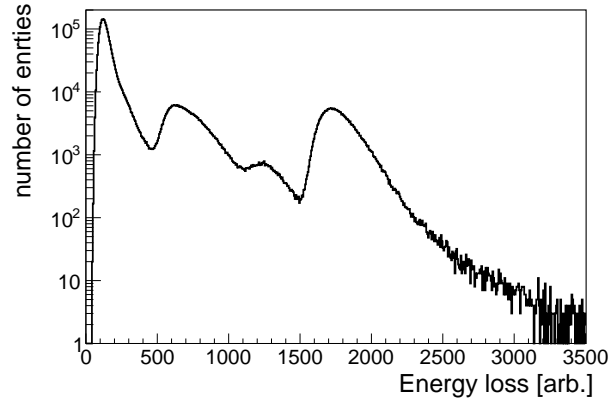
Figure 44: Energy deposited by all tracks measured in the GTPC. Peaks from particles with different charges are visible.

- The angle of the track in both XZ and YZ planes have to be within (70-110°) range,

- Only track with the highest energy loss was selected.

The cuts used in this analysis can be compared with fig. 25 and **??**. The values of the cuts were chosen to reject as much of the off–time beryllium particles without reducing statistics by a strong MHTDC event cut.

The GTPC energy loss spectrum after above cuts is shown on fig. 45. The procedure of calculating final result follows the procedure from the S4 analysis. The probability of interaction as a function of cut which define interaction for the GTPC analysis is plotted on fig. 46 and fig. 47.

The above methods of calculating inelastic cross section are model independent, therefore no model systematic error is present.

The systematic error related to the limited charge resolution of the detectors was described above and is calculated for both S4 and GTPC methods. At beam momenta of $40A$ and $150A$ GeV/c no visible plateau is present. The values for the final result were taken from a somewhat stable region just before the beam peak fluctuations. Due to this fact a rather large systematic error is assigned to

71
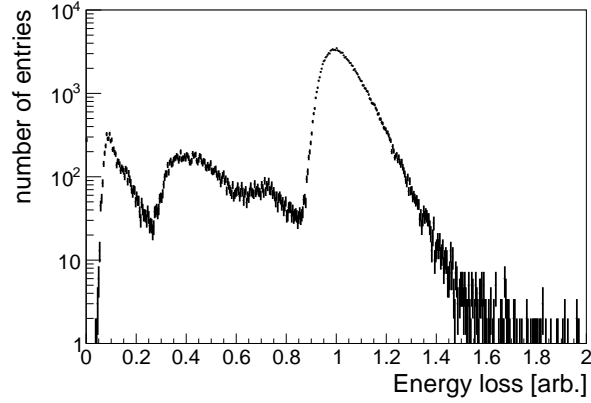
Figure 45: Energy loss from the tracks after cuts used in inelastic cross section analysis measured in the GTPC. Peaks from particles with different charges are visible.
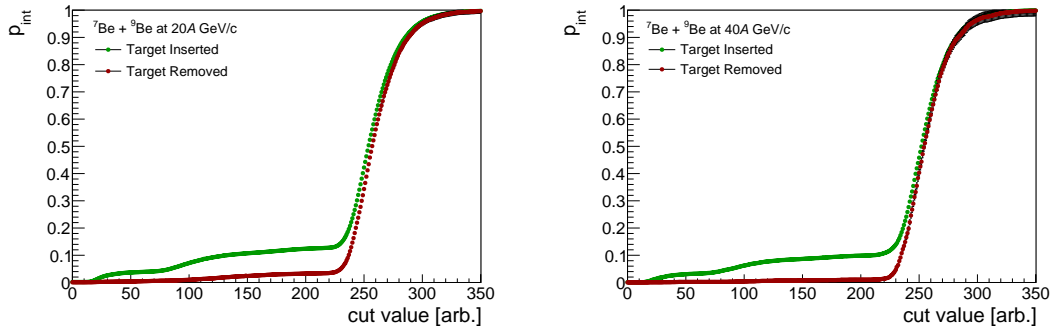
Figure 46: Probability of interaction, calculated by the GTPC method, in target inserted and target removed configuration as a function of interaction cut value. At 20A GeV/c *(left)*, a higher target removed interaction rate is visible. The larger background is due to interactions in the S4 detector placed just before the GTPC.

this measurements. The lack of a clear plateau may be caused by the fact that the GTPC was uncalibrated. A time dependant calibration could help reduce the systematic error at these beam momenta.

The track selection criteria effect on the final result was checked by varying the
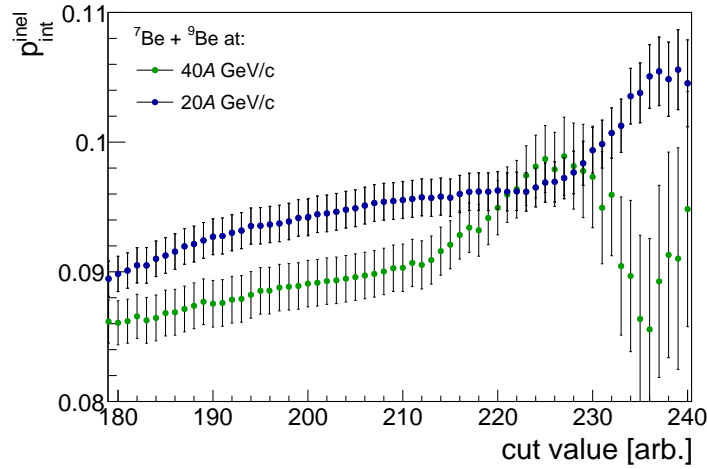
Figure 47: Probability of interaction after background subtraction for $20A$ GeV/c and $40A$ GeV/c beam momenta.

For $20A$ GeV/c (blue points) there is a plateau at 220 just before the beam peak, from which the final cross section value was calculated. The systematic error for the method was estimated by calculating cross section for values just after and before the plateau.

For $40A$ GeV/c (green points) no plateau is visible. The value used for calculating cross section was selected from the region just before large fluctuations due to the beam peak. A rather large systematic error was estimated by using value just before an enhancement at ≈ 215.

track cuts. The results were recalculated with two and three times more tight, and two and three times more loose cuts. The effect was smaller than 0.1% and will be neglected.

GTPC method do not suffer from the problem of interaction within the active volume of the detector. As a tracking detector such interaction would result in a shorter track with a lower energy loss resolution, but it would not cause misidentification of the charge, as in the S4 method.

Systematic errors related to the beam position on target were checked and calculated

according to the procedure described for the production cross section calculation. No effect was found.

Due to the analysis procedure only a beryllium off-time particle could cause bias of the inelastic cross section calculation. Fortunately, the MHTDC cut reject all events with beryllium off-time from 120 ns. While beryllium off-time within 120 ns from the trigger is rejected by the beam composition and Z vs. Z delayed cut. Therefore, no systematic error due to off-time particles will be assigned to the final result.

8.2.4. Results

A table with the results of the inelastic ^{7}Be + ^{9}Be cross section measurement together with the values of the statistical and systematic errors can be seen in table 12. The results are also plotted in the fig. 48.

Table 12: Inelastic cross section of ^{7}Be + ^{9}Be interaction. The GTPC method results are presented. The results are presented using following convention: result $\pm$ statistical error $\pm$ systematic error related to the uncertainty of defining charge of the measured particle (method) $\pm$ systematic error related to the uncertainty of the target parameters (target).

p_{beam} [GeV/c]	$p_{\mathrm{int}}^{\mathrm{inel}}$ [%]	σ_{inel} [mb]	stat. error	total sys. error
$13A$	9.73 ± 0.29	$684.3 \pm 19.2 \pm^{+13.3}_{-6.4}$ method $\pm 17.8^{\mathrm{target}}$	2.8%	3.4%
$20A$	9.62 ± 0.14	$676.2 \pm\ \ 9.6 \pm^{+5.7}_{-4.8}$ method $\pm 17.6^{\mathrm{target}}$	1.4%	2.8%
$30A$	9.63 ± 0.10	$676.9 \pm\ \ 6.4 \pm^{+0.6}_{-4.1}$ method $\pm 17.6^{\mathrm{target}}$	0.9%	2.7%
$40A$	9.73 ± 0.39	$684.6 \pm 26.2 \pm^{+11.8}_{-51.6}$ method $\pm 17.8^{\mathrm{target}}$	3.8%	8.1%
$75A$	9.67 ± 0.12	$679.8 \pm\ \ 7.8 \pm^{+9.5}_{-1.6}$ method $\pm 17.7^{\mathrm{target}}$	1.2%	2.9%
$150A$	9.62 ± 0.33	$676.0 \pm 22.0 \pm^{+37.1}_{-37.4}$ method $\pm 17.6^{\mathrm{target}}$	3.3%	8.1%

A results of both production and inelastic cross section of ^{7}Be + ^{9}Be interactions
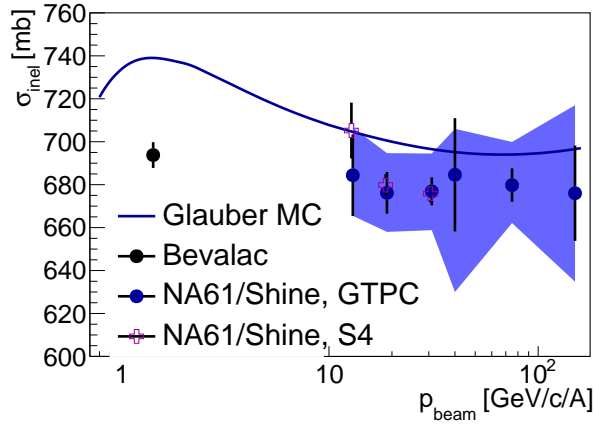
Figure 48: Inelastic cross section of ^{7}Be + ^{9}Be interactions. Previous measurment at $p_\mathrm{beam} = 1.45A$ GeV/c by Bevalac [8] comes from dedicated inelastic cross section measurement experiment. The NA61/SHINE data from both GTPC and S4 method is presented. The shaded band depicts a systematic error of the GTPC method. The S4 method agree within the errors with the GTPC method. The Glauber [6, 7] Monte-Carlo line was calculated by Geant4 [34–37].

together with previous measurements and model predictions are presented in fig. 49. For inelastic cross section results from the GTPC method were used. Both methods achieve similar precision, but performing GTPC method is possible for more beam momenta.
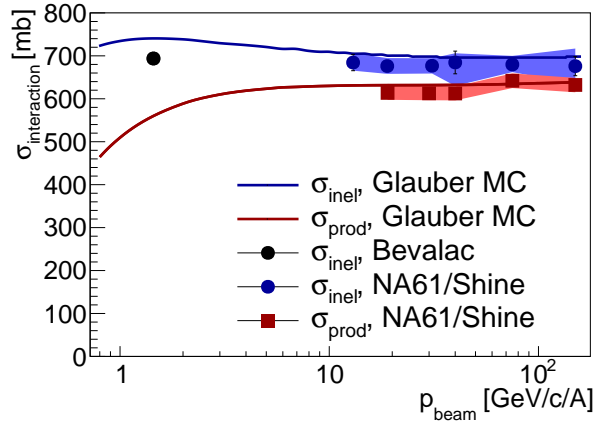
Figure 49: Inelastic and production cross section of ^{7}Be + ^{9}Be interactions. Previous measurement and Geant4 model predictions are plotted together with the new NA61/SHINE data.

9. Centrality determination

The centrality of the ^{7}Be + ^{9}Be collisions are determined by the measurement by the Projectile Spectator Detector (PSD). PSD is a modular compensating zero-degree calorimeter. The modularity of the detector ensures low position dependence of the measured energy. The modularity also allows to determine centrality based on the energy measured with various modules selection.

9.1. Projectile Spectator Detector

The Projectile Spectator Detector used in the following analysis consists of 44 transverse modules, 16 small (10 × 10 cm) modules in the central region of the detector and 28 large (20 × 20 cm) modules around the small modules (fig. 50 *(left, right)*). Each module of the PSD consists of 60 pairs of alternating plates of lead and scintillator (fig. 50 *(centre)*). The scintillators are read out by ten Silicon Photomultipliers (SiPMs) each of them connected through Wavelength Shifting Fibres to six scintillators, to allow longitudinal calibration of the detector as well

as the characterization of the longitudinal particle shower development.
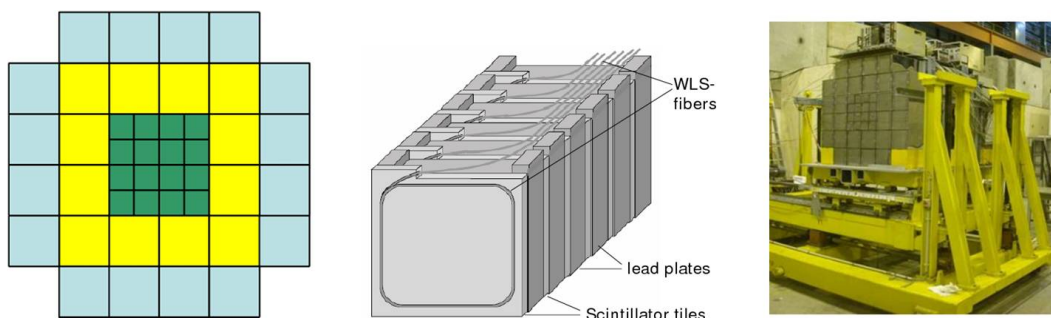
Figure 50: *(left):* Frontface of the PSD, *(center):* construction of a single PSD module, *(right):* photo of the PSD

9.2. Module selection

To select optimal modules to calculate centrality, a Monte-Carlo simulation was carried out. The minimum bias events were simulated with EPOS 1.99 primary generator. The EPOS generator includes fragment coalescence and therefore produces nuclear fragments. The momenta of fragments, as well as spectator protons and neutrons were smeared with Fermi motion momentum. The Fermi motion momentum was simulated isotropically in the fragment rest frame with the magnitude generated randomly from the Gaussian distribution with width of $\frac{200\text{MeV}}{A}$, where A is the mass number of the fragment. Then the simulated Fermi momentum were boosted to the lab frame. The Fermi momentum boosted spectators are then transported in the magnetic field to the front face of the PSD. The results of this simulation can be found in fig. 51. To calculate centrality at $13A$, $20A$ and $30A$ GeV/c beam momenta a module selection including all PSD modules was used. To calculate centrality for the higher beam momenta a module selection containing eight small and four large modules was used (top right picture on fig. 52). Additionally, centrality was calculated in the module ensembles shown on fig. 52 to calculate systematic error related to the definition of the centrality.
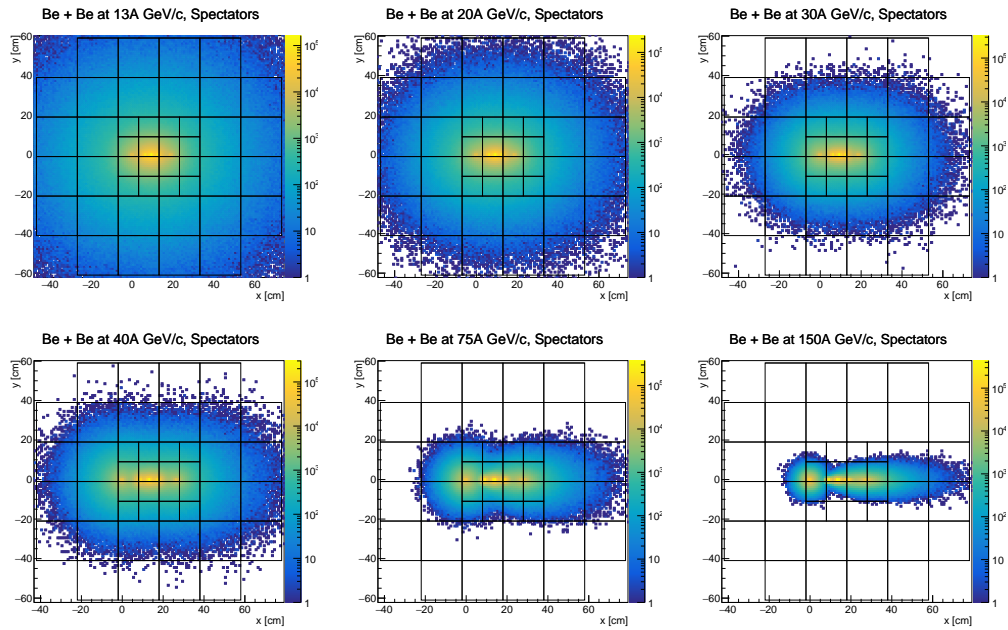
Figure 51: Simulation of spectator hits on the front face of the PSD. Three main clusters are visible. The left cluster correspond to neutrons, the middle one to nuclear fragments, and the right one to protons. Particles with different $\frac{Z}{A}$ ratio are deflected differently in magnetic field which lead to clustered appearance of above distribution.

9.3. Procedure

The centrality analysis was done in two steps. First, centrality was calculated based on the data taken with an identified beam trigger to have a minimally biased result, although with a large statistical error. Then, centrality was calculated with central identified interaction trigger. This result was compared with the unbiased result from identified beam trigger dataset to discard part of the data biased by the trigger conditions. The result obtained with this procedure have much smaller statistical error (most of the recorded data was taken with the central interaction trigger) and part of the data biased by the trigger conditions are safely discarded.

The procedure of calculating centrality is as follows.
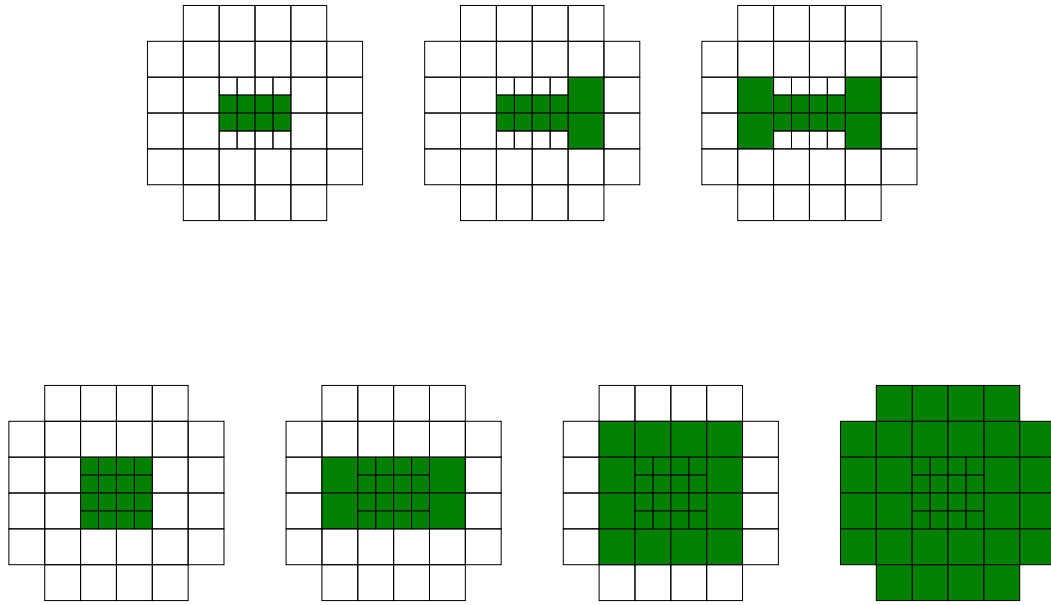
Figure 52: Various module selections used to calculate centrality. The smaller module selections suffer from bias due to spectators hits beyond acceptance. The larger module selections suffer from bias due to acceptance of non-spectator particles. Comparison of obtained analysis results with centrality selected based on different module selections can be used as a estimate of systematic error related to centrality definition.

First, only interacting events are selected by the same criteria as used in the inelastic cross section calculation (see section 8.2). For these events a histogram of the measured PSD energy is plotted and then normalized to the number of beam events (with or without interaction).

The normalization is straightforward for the beam trigger.

For interaction trigger, a trigger bias have to be calculated to determine what fraction of the cross section is registered. A fraction of cross section registered by the interaction trigger is a ratio of events which fulfil the criteria of the interaction trigger within the beam trigger event sample and is calculated by the following formula:

$$p(\text{T2} \mid \text{T1}) = \frac{N(\text{T1} \wedge \text{T2})}{N(\text{T1})}, \tag{9}$$

where $p(\text{T2} \mid \text{T1})$ is the probability of fulfilling the interaction trigger condition within the beam trigger event sample, $N(\text{T1})$ is the number of beam trigger events and $N(\text{T1} \wedge \text{T2})$ is the number of interacting events within the beam trigger event sample.

The normalization factor for the interacting trigger can be obtained using a following formula:

$$f_{\text{T2}} = \frac{N(\text{T2})}{p(\text{T2} \mid \text{T1})}, \tag{10}$$

where f_{T2} is the normalization factor and $N(\text{T2})$ is the number of events within interaction trigger event sample.

The procedure is performed independently for the target inserted and target removed configuration. The example histograms of the PSD energy of the interacting events can be seen on fig. 53 for target inserted configuration. Comparison of target inserted and removed configuration can be found on fig. 54.

From the histograms of the PSD energy a centrality is calculated according to the formula:

$$c(E_{\text{PSD}}) = \frac{\int_0^{E_{\text{PSD}}} \mathrm{d}E_{\text{PSD}}^{\text{inserted}} - \int_0^{E_{\text{PSD}}} \mathrm{d}E_{\text{PSD}}^{\text{removed}}}{1 - \int_0^{E_{\text{PSD}}} \mathrm{d}E_{\text{PSD}}^{\text{removed}}} \Bigg/ \sigma_{\text{inel}}, \tag{11}$$
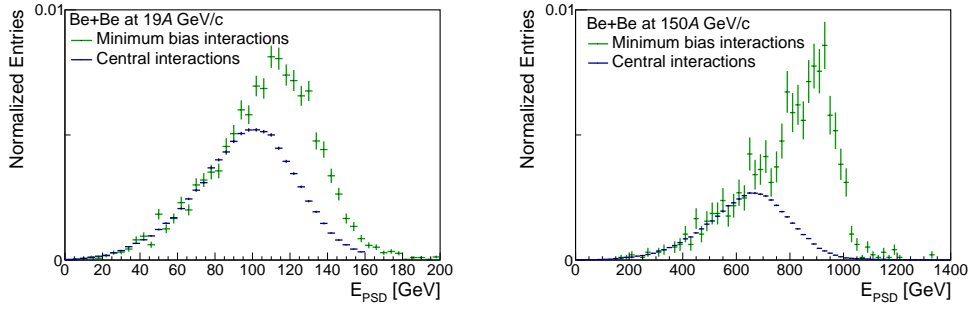
Figure 53: Two examples of the PSD energy distribution in target inserted configuration for beam trigger and central trigger. Only inelastic interactions are plotted. Histograms are normalized to the probability of inelastic interaction. Central interaction data are additionally scaled by the central trigger bias.

(left): 19*A* GeV/c dataset, *(right)* 150A GeV/c dataset.
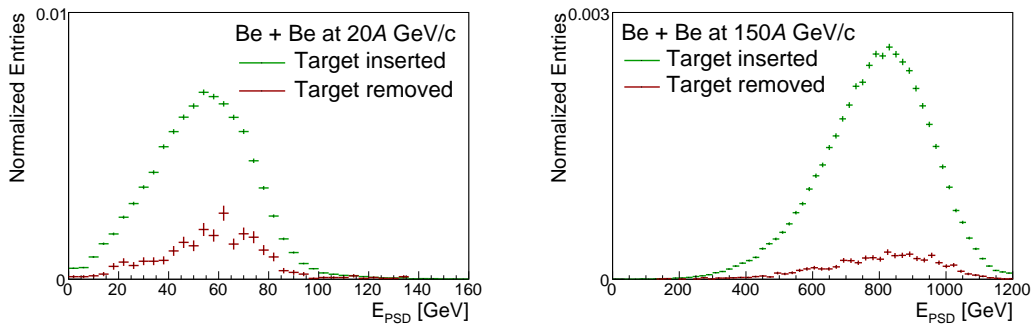
Figure 54: Two examples of the PSD energy distribution of minimum bias interactions for target inserted and removed configurations. The histograms are scaled to the probability of inelastic interaction for the corresponding dataset.

(left): 19*A* GeV/c dataset, *(right)* 150A GeV/c dataset.

The whole procedure is performed for all beam momenta and the PSD energy defined by a various module selections. The example centrality functions can be seen on fig. 55
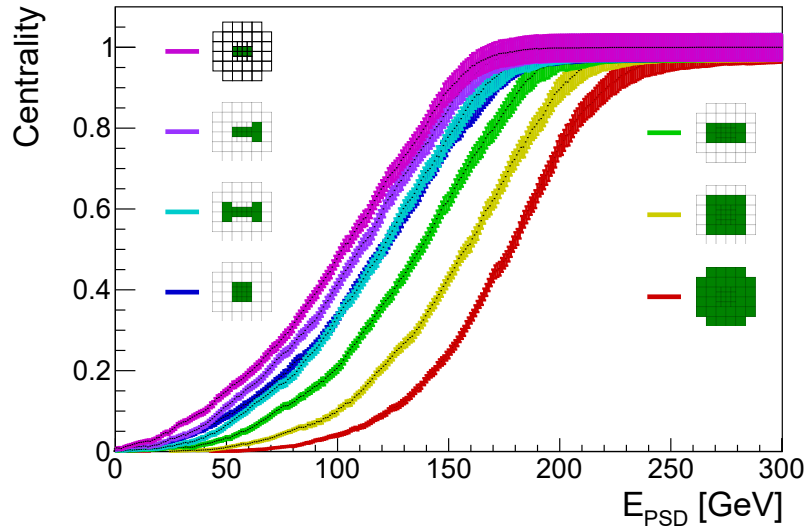
Figure 55: Centrality as a function of the energy deposited in various module selections of the PSD. Hue of the curves denote module selection. The violet-blue curves correspond to small module selections, the yellow-red curves correspond to module selections including most of the modules.

9.4. Software library design

As centrality selection will be used by all of the NA61/SHINE beryllium analyses a simple to use software package had to be developed.

The centrality selection software was written as a C++ class implemented as a header library. Such design ensures ease of use even for the users not very familiar with the use of external packages within theirs analysis programs.

The header library design was chosen as it require only one line of code and no changes to the compilation to include it to the analysis program. Namely:

```
#include <Centrality.h>
```

The use of the library to obtain desired centrality is equally easy. To setup the class:

```
Centrality DetermineCentrality;
// path to calculated centrality data
DetermineCentrality.SetDataPath("/afs/cern.ch/.../ ");
// edges of the centrality classes
double centralityEdges[4] = {0.05, 0.1, 0.15, 0.2};
DetermineCentrality.SetCentralityEdges(centralityEdges);
```

And then to determine centrality of a given event:

```
int centralityClass = DetermineCentrality.GetCentralityClass(event);
```

where event is a variable holding the event structure and centralityClass is
the centrality class of the studied event.

10. Parametric PSD simulation

To select centrality in the Monte–Carlo data a simulation of the PSD is necessary. Unfortunately, a proper microscopic simulation of the particle shower within the PSD is extremely time consuming. To simulate one minimum bias event within the Geant4 framework a ten minutes of CPU time is required. To simulate statistics order of magnitude larger than data statistics (necessary to not increase statistical errors of the results) using CERN's computing cluster more than four months for one beam momentum would be required. Therefore, a simpler simulator was necessary.

The standard simulation chain of the NA61/SHINE experiment provide information about the particles impinging on the front face of the PSD. The particle decays between target and the PSD are taken into account and momentum, mass and the history of the particle is available. The history of the particle can be used to determine whether the particle was produced in the interaction or was a non-interacting spectator.

Using this information a sum of the energy of the particles hitting PSD can be calculated. Such a simple approach neglects effects of the limited energy resolution of the detector as well as the leakage of the particle shower out of the detector.

A PSD detector simulator using parametrization of the detector resolution and parametrization of the particle shower had to be developed to obtain reasonable agreement with the experimental data using the CPU time available to the collaboration.

10.1. Software module design

The fast, parametrized PSD simulator is a necessary part of the Monte-Carlo simulation chain of the NA61/SHINE experiment.

The simulator was implemented in two modules of the S$\underline{\text{HINE}}$ $\overline{\text{Off}}\underline{\text{line}}$ software

framework [38].

The first one, *FermiMotionSimulatorEK*, selects spectators (based on collision history from MC generator), simulate fermi motion and change the momentum of the spectators. This module is currently tuned to EPOS 1.99 MC generator, but including any other generator that do not simulate fermi motion is possible.

The second module, *PSDSimulatorEK*, simulates detector resolution and transverse particle shower for each particle that hits PSD. Then, the module adds up energy deposited within each module and populate the event structure responsible for holding measured PSD energy.

10.2. PSD resolution

The distribution of the energy deposited in the PSD from single particle type hitting the PSD comprises of two regions.

For deposited energies equal or higher than the particle energy the shape of the distribution is dominated by the resolution of the detector.

For deposited energies lower than the particle energy the resolution of the detector is convoluted with the energy of the particle shower leaking out of detector. Furthermore, there is a possibility of interaction of the measured particle between the beam detectors and PSD. Such interactions also cause change of the shape of the PSD energy distribution in the region of energies lower than particle energy.

Therefore, to calculate the resolution of the PSD mostly the region of the energies higher than the particle energy have to be used. An example Gaussian fit to the ^{7}Be at 150A GeV/c momentum is presented on the fig. 56. The stability of the fit with respect to changing lower range of the fit was tested the results can be seen of fig. 57. The width of the distribution behave as expected. When the lower range of the fit is very close to the maximum of the distribution the width increases due lack of constrain from the left slope of the distribution. When the lower range of the fit is too far from the maximum the residual interactions and shower leak rises

width of the fitted function.
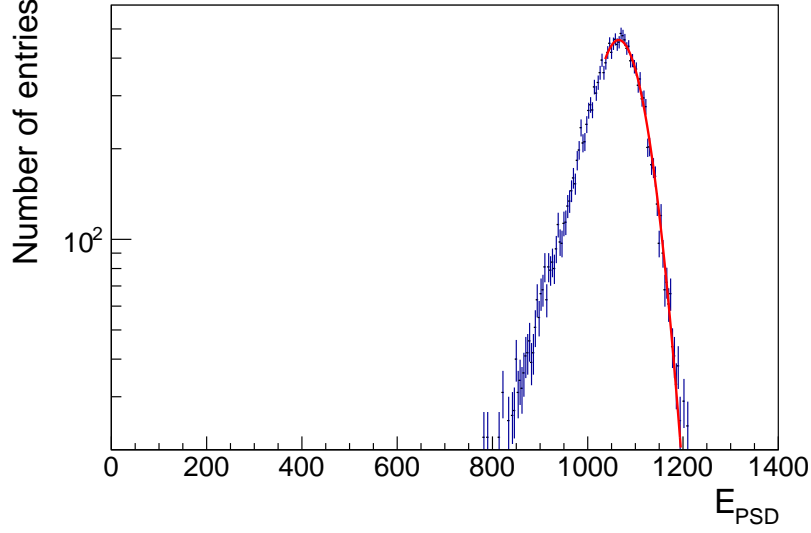
Figure 56: PSD energy deposition of the beryllium beam particles with momentum equal $150A$ GeV/c. The red line denotes a Gaussian fitted to extract resolution of the detector.

The beryllium beam was produced from lead beam fragmentation. Therefore, ions such as ^{2}H, ^{4}He, and ^{6}Li are also present in the beam. Data taken with the trigger without beam particle identification was used to determine the PSD energy resolution as well.

The resolution of the calorimeter is given by the formula [39]:

$$\frac{\sigma_{E_{\text{PSD}}}}{E_{\text{PSD}}} = \frac{a}{\sqrt{E}} + \frac{b}{E} + c \qquad (12)$$

The eq. (12) was fitted to the data obtained by fitting peaks of the PSD energy distribution of various beam ions and beam momenta. The result of the fit can be seen at fig. 58.

The equation describing the resolution of the PSD can be written as:

$$\frac{\sigma_{E_{\text{PSD}}}}{E_{\text{PSD}}} = \frac{0.72}{\sqrt{E}} + 0.026 \qquad (13)$$

86
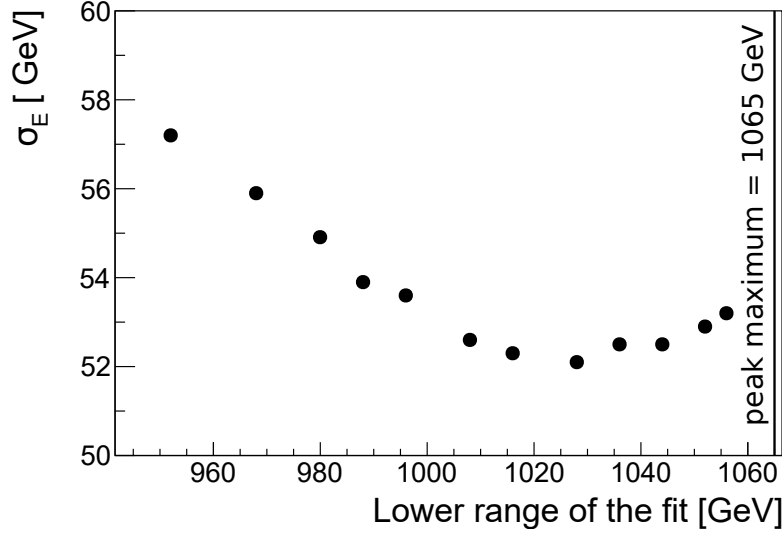
Figure 57: The width of the Gaussian fitted to the PSD energy deposition from the beryllium beam as a function of the lower range of the fit. Vertical line correspond to the maximum of the fitted distribution. At small lower range the increase of the width is caused by residual interactions in the data sample, as well as events where particle shower was not fully contained within the PSD. At large lower range the increase of the width of the fit correspond to the insufficiently constrained fit due to small number of point on the left edge of the distribution.

The b parameter of eq. (12) was fitted as 0.

10.3. Longitudinal shower profile parametrization

To simulate particle shower leakage through the back of the calorimeter an event-by-event parametrization of the longitudinal shower profile is necessary.

Within the PSD a particle will interact (and produce particle shower) after traversing some of the material of the detector. The PSD have interaction length of $7\lambda_i$. Such interaction length allows for 0.1% of particles to pass without interaction in the
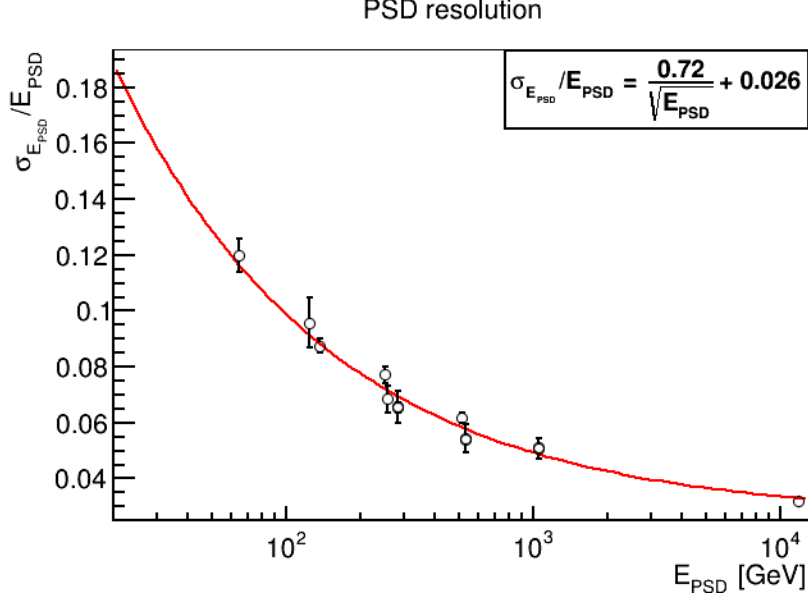
Figure 58: The energy resolution of the PSD. The point at > 10 TeV correspond to a test run of $75A$ GeV/c lead. The rest of the points correspond to the deuterium, helium and beryllium ions at three beam momenta.

detector.

To obtain event-by-event parametrization of the particle shower a fit of the interaction point, as well as shower parameters are necessary. A parametrization given by the Calice Collaboration [40] was attempted with an additional parameter responsible for the determination of the interaction point. The fitted function was of the following form:

$$\Delta E = A \cdot \left(\frac{f}{\Gamma(\alpha_{\text{short}})} \cdot \left(\frac{z^{\prime}}{\beta_{\text{short}}} \right)^{\alpha_{\text{short}}-1} \cdot \frac{e^{-\frac{z^{\prime}}{\beta_{\text{short}}}}}{\beta_{\text{short}}} + \frac{1-f}{\Gamma(\alpha_{\text{long}})} \cdot \left(\frac{z^{\prime}}{\beta_{\text{long}}} \right)^{\alpha_{\text{long}}-1} \cdot \frac{e^{-\frac{z^{\prime}}{\beta_{\text{long}}}}}{\beta_{\text{long}}} \right),$$

$$z^{\prime} = z - z_0,$$

where subscripts $_{\text{short}}$ and $_{\text{long}}$ denotes short and long component of the fit, α are the shape parameters, β are the slope parameters, f is a fractional contribution of the short component, A is a normalization factor, and z_0 is the interaction point.

Unfortunately, the fit was unstable. The z_0 parameter values were not following

physical expectations (exponential decay). The example event-by-event longitudinal profiles of the particle shower are presented on fig. 59.
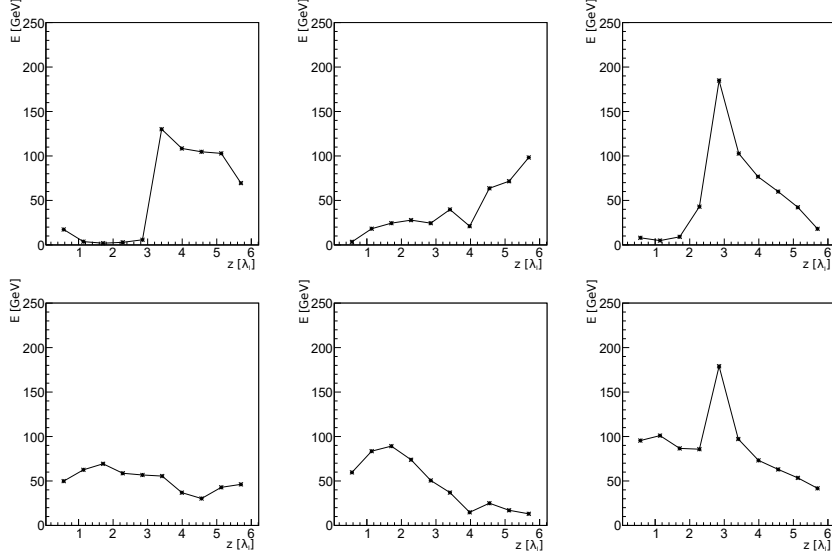
Figure 59: Event-by-event longitudinal profiles of the particle shower measured by the PSD. All presented events were randomly chosen from the $150A$ GeV/c beryllium data sample.

To test the reasons of the poor fit performance a fit from the calorimeter front face was attempted according to the parametrization given by [41].

The parametrization have a form:

$$
\begin{aligned}
\frac{\mathrm{d}E}{\mathrm{d}x} = N\Bigg\{ & \frac{wX_0}{a}\left(\frac{x}{X_0}\right)^a e^{-b\frac{x}{X_0}}\,_1F_1\left(1, a+1, \left(b - \frac{X_0}{\lambda_\mathrm{I}}\right)\frac{x}{X_0}\right) \\
& + \frac{(1-w)\lambda_\mathrm{I}}{a}\left(\frac{x}{\lambda_\mathrm{I}}\right)^a e^{-d\frac{x}{\lambda_\mathrm{I}}}\,_1F_1\left(1, a+1, -(1-d)\frac{x}{\lambda_\mathrm{I}}\right)\Bigg\},
\end{aligned} \tag{14}
$$

where N is the normalization constant, X_0 is the radiation length of the detector material, λ_I is the interaction length of the calorimeter, w is the fractional contribution of the electromagnetic component of the shower, and a, b, c, d are the parameters of the fit. The $_1F_1(\alpha, \beta, z)$ is the confluent hypergeometric function (CHF) [42]. The CHF in the first term can be calculated by:

$$
_1F_1(1, a+1, z) = az^{-a}e^z\gamma(a, z),
$$

where $\gamma(a, z)$ is the incomplete gamma function [42].

The CHF in the second term can be calculated using the series expansion:

$${}_1F_1(1, a+1, -z) = 1 - \frac{z}{a+1} + \frac{z^2}{(a+1)(a+2)} + \cdots,$$

according to [41] only three terms are enough to calculate the function with a per mille precision. In this work the series was calculated up to fifth term, as the fit was relatively fast.

An example fit the the longitudinal shower profile for ^{7}Be at 150A GeV/c momenta can be seen at fig. 60. The PSD energy profile, together with the fitted parametrization allow to gain better understanding why the event-by-event fit was unsuccessful.
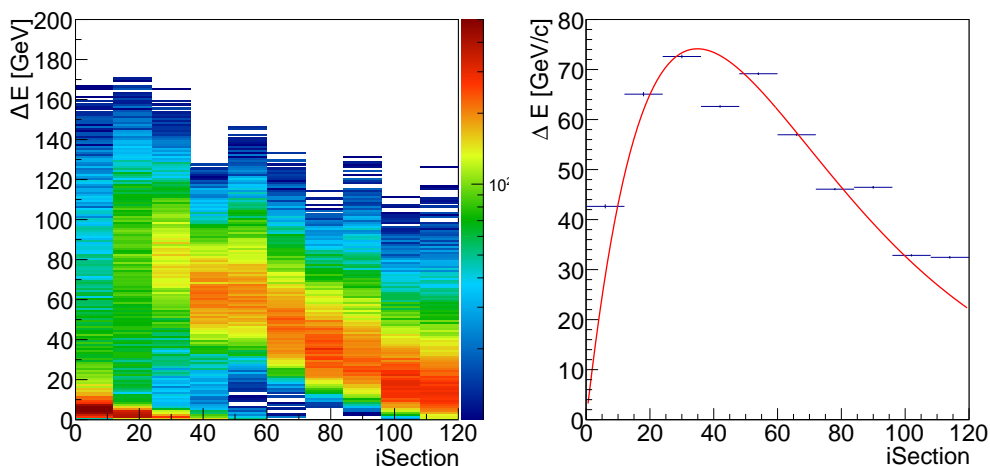
Figure 60: *(left)*: Energy deposited in each readout section of the PSD. Twelve physical sections are readout together, which allows for ten energy measurement in longitudinal direction. The area of high event density at low energy and small section number correspond to particles that interacted deeper within the PSD.
(right): Profile of the *(left)* histogram. The fit by the eq. (14) are represented by the red line. Poor calibration of some of the sections are visible as large deviation from the fitted function.

90

The PSD have only 10 longitudinal sections. While fitting the function which parametrize the shower from the front face of the PSD it gives 5 degrees of freedom, which allow a stable fit. Fit by the event-by-event parametrization have more parameters (6 vs. 5) and should still work well for the showers that start in the first few section of the PSD. Unfortunately, when shower starts at e.g. fifth section all of the preceding sections do not give important information. Therefore, the fit is unstable for such events.

Additionally, on fig. 60 a poor calibration of some sections can be seen.

Unfortunately a fit of the longitudinal shower profile starting from the front face of the PSD is of little use. The only information that can be extracted from it is the average energy leakage from the back side of the calorimeter. This average energy leak is already corrected for on the data calibration level. Therefore, the inclusion of such effect is not necessary in the simulation.

10.4. Transverse shower profile parametrization

The transverse particle shower is an important effect to include in the PSD simulation. The particle energy can leak out of the side walls of the PSD. The particles hitting closer to the sides will register as lower energy particles due to the transverse shower extending out of the detector.

In addition, due to the use of only some modules for calculating centrality of the collisions particles hitting modules out of the used module set will leak part of their energy into the modules used in analysis. For small module selections (e.g. only 8 small modules) effect can be significant, as seen on fig. 61.

To parametrize transverse particle shower profile a parametrization of the following form was used:

$$\frac{\mathrm{d}E}{\mathrm{d}x} = A \cdot \left(f \cdot e^{-\sqrt{x'^2 + y'^2}/\lambda_{\mathrm{long}}} + (1 - f) \cdot e^{-\sqrt{x'^2 + y'^2}/\lambda_{\mathrm{short}}} \right), \qquad (15)$$

$$x' = x - x_0, \quad y' = y - y_0,$$
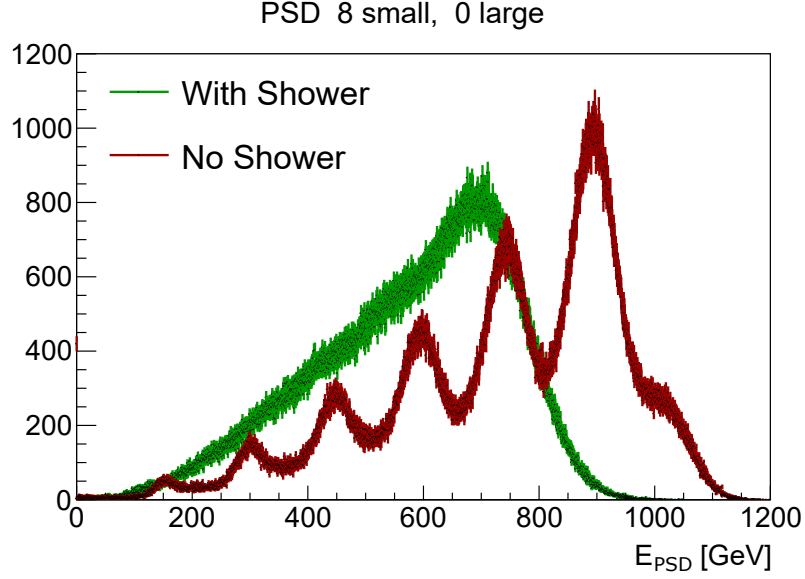
Figure 61: Simulated PSD energy deposition from minimum bias ^{7}Be + ^{9}Be collisions at beam momentum of $150A$ GeV/c. The effect of enabling transverse particle shower simulation is visible.

where A is the normalization constant, λ_{short} and λ_{long} are the slope parameters, f is the fractional contribution of the "long" term, and x_0 and y_0 are the transverse position of the interaction point.

Each PSD module integrates the energy deposited within its volume. However, an eq. (15) gives energy loss at a point. Therefore, eq. (15) have to be integrated in range corresponding to each module position and size at each step of the fit. Each calculation of the χ^2 involve 44 (number of PSD modules) 2D integrations. With hundreds of iterations of the χ^2 minimizer (MINUIT/MIGRAD [43]) for each particle hitting the PSD the procedure is very time consuming. However, using this parametrization during the simulation involve calculating only 44 integrals per simulated particle hitting the PSD, which is much faster than microscopic shower simulation.

A two step approach to fit the transverse shower profile was implemented.

First, only particles with similar trajectories were selected, an average shower profile was calculated and then fitted. This pre–fit allowed to determine starting parameters and the range of the parameters for the second part of the procedure.

After the pre–fit an event-by-event fit was performed. The interaction point position starting values were determined by extrapolation of the beam track measured by the BPDs. The rest of the parameters had their starting point determined by the pre–fit. An example x-axis projections of the event-by-event transverse particle shower profile fits can be seen on fig. 62.
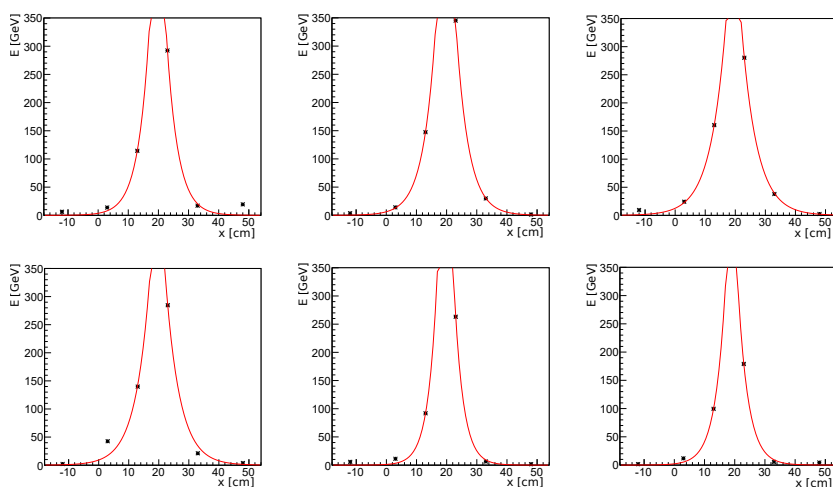
Figure 62: X-axis projections of the event-by-event transverse particle shower profile fits. An example of six randomly chosen events are presented.

The interaction point position obtained by event-by-event fit was correlated with the beam track extrapolation (fig. 63). While the horizontal (x) position of the interaction point exhibit almost perfect correlation, the vertical (y) position demonstrate some discrepancy. The non–zero intercept parameter appear when the PSD or BPDs position is measured imprecisely. Such discrepancy is easy to correct. However, the vertical position exhibit discrepancy in the slope parameter. This discrepancy is most likely caused by the beam hitting a horizontal edge of the module which biases the position measurement. As can be seen from the fig. 63 the slope of the correlation changes for particles hitting the PSD further from the

93

module edge. The bias due to the module edges was neglected as it biases the fitted position by at most $1\,\mathrm{cm}$ only for particles that hit close to the module edge, while the slope parameters (which determine width of the profile) are much larger than this bias.

As a test of the fitting method a normalization parameter distribution (fig. 64) was compared with the detector resolution. The difference is small:

$$\frac{\sigma_A}{A} = 6.8\% \approx 7.0\% = \frac{\Delta E}{E}$$

The final parametrized transverse shower profile have the following form:

$$\frac{\mathrm{d}^2 E}{\mathrm{d}x\,\mathrm{d}y} = A \cdot \left(0.964 \cdot e^{-\sqrt{x'^2+y'^2}/1.91} + (1 - 0.964) \cdot e^{-\sqrt{x'^2+y'^2}/7.83} \right),$$

where the A parameter depends on the particle energy. During simulation the A parameter is selected by the requirement $E_{\mathrm{particle}} = \int \frac{\mathrm{d}^2 E}{\mathrm{d}x\,\mathrm{d}y}\,\mathrm{d}x\,\mathrm{d}y$.

10.5. Centrality in the Monte-Carlo simulation

After the parametrized PSD simulator the event structure contain information of the deposited PSD energy in each module. The structure for simulated data is exactly the same as for measured data.

To calculate centrality in the simulated data, first histogram of the deposited PSD energy is constructed for the same module selections as in measured data.

Due to different definition of the interaction between measurement (all inelastic events) and MC (events where at least one particle was produced) Monte-Carlo data have to be calibrated to the measured data.

The calibration is performed by normalization of MC energy distribution to the measured energy distribution from the central interaction trigger in a range from $E_{\mathrm{PSD}} = 0$ to the value of E_{PSD} which correspond to 20% most central events according to measured data (which is unbiased by the trigger requirements). The comparison of the simulated energy distribution with the distribution obtained
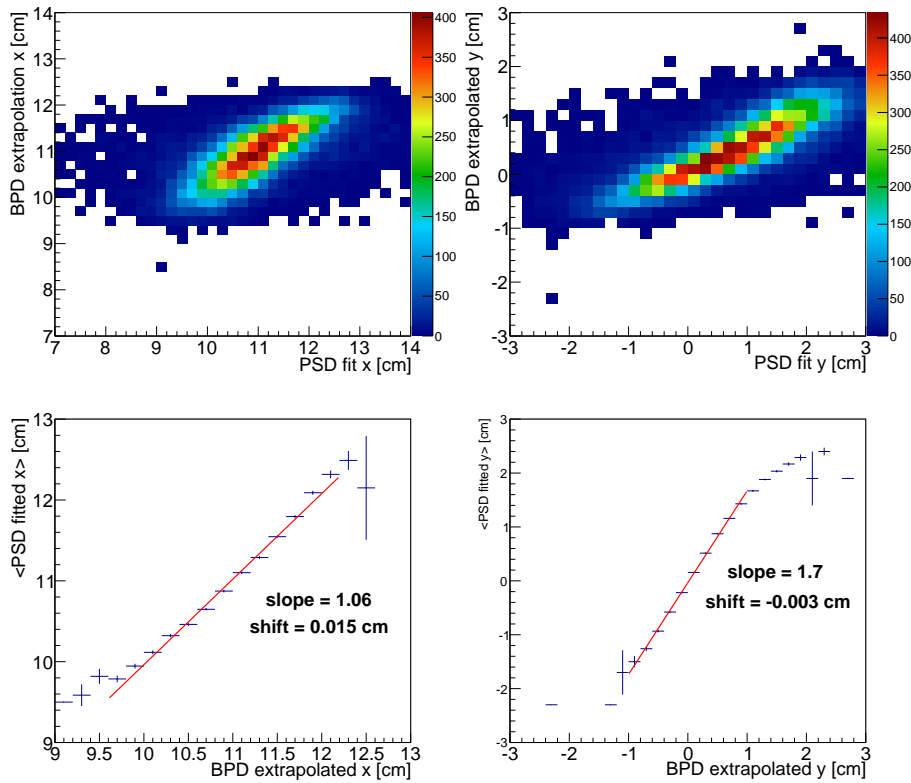
Figure 63: *(top)*: Correlation between beam trajectory extrapolated from beam
position detectors to the PSD and interaction point fitted from transverse
particle shower in the PSD. The outliers of the distributions are caused
by scattering of the beam particles on 22 meters of material between
BPDs and PSD.

(bottom): Average interaction point position obtained from the shower fit
as a function of extrapolated beam trajectory position. The X position
of the fit is the same as the extrapolated position. The Y position
exhibit some difference caused by beam hitting close to the PSD module
edge. Further from the module edge the fitted and extrapolated position
is again compatible.

from data is difficult on the level of PSD energy. The PSD energy distribution
from target inserted dataset have a non-negligible background from out-of-target
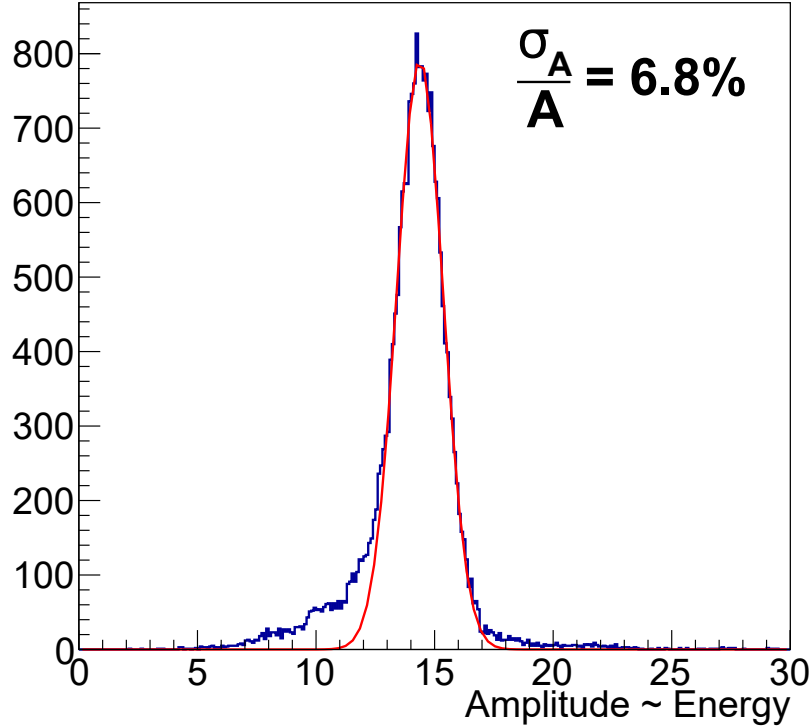
Figure 64: Amplitude of the event-by-event transverse particle shower fit. The tail at small amplitudes exists due to the longitudinal leak of the shower.

interactions. The comparison can be made on the level of background corrected centrality curves (fig. 66, fig. 65).

The centrality for simulated data is calculated according to the formula:

$$c(E_{\mathrm{PSD}}) = \int_0^{E_{\mathrm{PSD}}} N(E\text{'}_{\mathrm{PSD}}) \, \mathrm{d}E\text{'}_{\mathrm{PSD}}$$

The parametrization of the transverse particle shower within the PSD was done only for $150A$ GeV/c beryllium ion. Therefore, the performance of the simulation should be best at high beam momenta (fig. 65).

Indeed, at high beam momenta data sets the simulation behaviour mirror the behaviour of measured data even with small module selections. At low beam
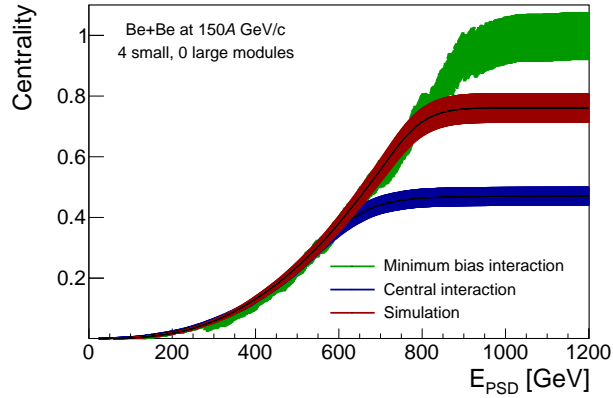
Figure 65: Comparison between experimental and simulated PSD centrality for high beam momentum and small PSD module selection

momenta the simulation perform very well with large module selections, but break down for selections which include small number of modules (fig. 66).
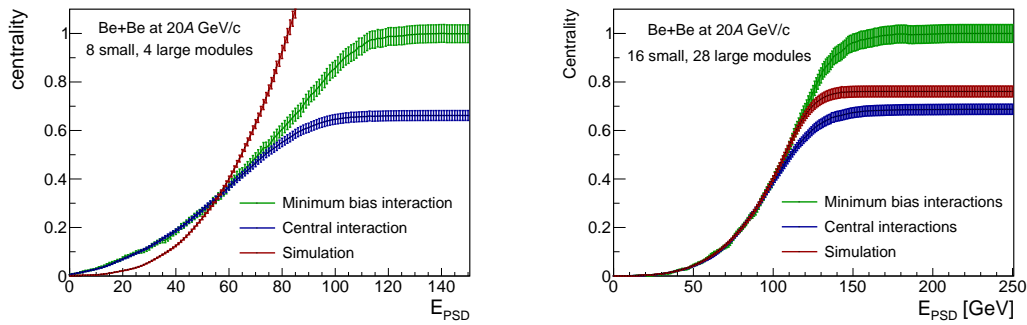
Figure 66: Comparison between experimental and simulated PSD centrality for low beam momentum. The simulation works well at large module selections, but breaks down for small module selections.

Such behaviour is not problematic. At high beam momenta the spectator spots on the PSD is narrow (fig. 51). Therefore, a good performance of the simulation is needed for small module selections. However, at low beam momenta, spectators occupy large part of the PSD surface. Hence, high module count is needed to contain them and it is enough for the PSD simulator to perform well only for the

large module selections.

The centrality curves for two example beam momenta can be seen on fig. 67 for simulation, as well as measured data. fig. 67 can be used to determine centrality at which central trigger introduce bias ($\approx 20\%$) and centrality where Monte-Carlo simulation diverge from the minimum bias data ($\approx 70\%$).
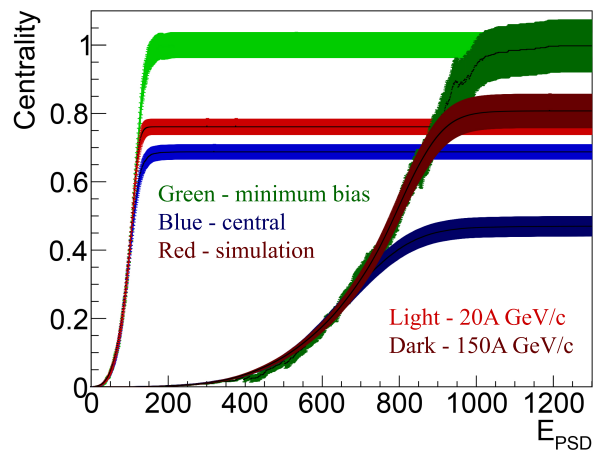
Figure 67: Centrality data for lowest and highest analysed beam momenta.

11. Spectra of the negatively charged pions

11.1. h⁻ method

In the heavy ion collisions at SPS energy range most of the produced negatively charged hadrons are π^- mesons [1, 2, 44]. Additionally, theoretical models of heavy ion collisions describe particle ratios in a relatively precise way [29, 45].

A method that use Monte–Carlo simulation to correct spectrum of all negatively charged hadrons to obtain π^- meson spectra will be described and used in the following chapter. The method is called h⁻ method.

The h⁻ method was compared with the methods that identify particles (dE/dx and ToF measurements) in p+p data. The differences were smaller than systematic error assigned to either measurement [29]. The main advantage of the h⁻ method is a very large acceptance, a comparison of acceptancee of dE/dx, ToF—dE/dx, and h⁻ methods is presented on fig. 68. The most important extension of the acceptance of the h⁻ method is the inclusion of the midrapidity for a large transverse momentum range.

The negatively charged pion spectra were obtained for five beam momenta: $13A$, $19A$, $30A$, $40A$, $75A$, $150A$ GeV/c. The spectra for $13A$ GeV/c beam momentum were not analysed due to low statistics, poor beam characteristics and difficulties with running Monte–Carlo models.
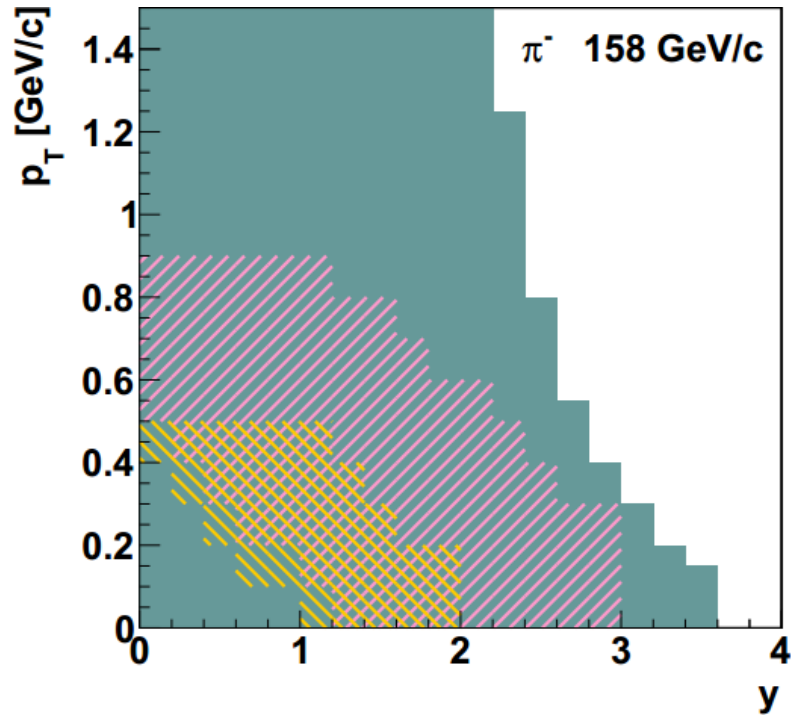
Figure 68: Comparison of the the acceptance for pi^- mesons of various particle identification methods.

11.2. Data selection

11.2.1. Non–biasing event cuts

In section 7 a detailed description of all non–biasing cuts is provided. The non–biasing cuts are divided into three categories:

- Selection of the properly reconstructed beam tracks

- Selection of the beryllium particles

- Rejection of the off–time particles

The number of events after each of the non–biasing cuts categories for all beam momenta are presented in the table 13.

The main difference between low beam momenta ($19A$ and $30A$ GeV/c) and higher

Table 13: Statistics of events after non–biasing cuts. $19A$ GeV/c and $30A$ GeV/c data cannot be compared with data for the higher beam momenta due to different trigger and beam detector setup. Beam Trajectory is a set of cuts rejecting events with poorly measured trajectory of the beam. Beam PID is a set of cuts selecting ^{7}Be beam particle from the secondary beam. Off–Time is a set of cuts rejecting events where two beam particles arrive close in time.

	All Events	Beam Trajectory	Beam PID	Off–Time
19A GeV	3440998	2380601	2048002	1015836
	100.0%	69.2%	59.5%	29.5%
30A GeV	4065716	2908097	2517817	1301211
	100.0%	71.5%	61.9%	32.0%
40A GeV	2859150	2329787	2166797	1815567
	100.0%	81.5%	75.8%	63.5%
75A GeV	3527415	2957699	2788147	2459424
	100.0%	83.8%	79.0%	69.7%
150A GeV	2344142	1764266	1607038	1332829
	100.0%	75.3%	68.6%	56.9%

beam momenta is the rejection of the off–time particles. The difference comes from the different trigger setup between these two data taking periods. In low beam momenta a cut rejecting minimum bias off–time interactions is possible. As the h⁻ method do not require large statistics this cut was set to reject any off–time minimum bias interaction within large time window.

11.2.2. Biasing event cuts

The biasing event cuts ensures that the interaction took place as well as define centrality of the interaction for further analysis. A detailed description of the cuts are presented in section 7.

The biasing cuts include following cuts:

- GTPC cut — selects minimum bias collision by rejecting events with beryllium charged track in the GTPC detector

- Primary vertex fit status — reject events with failed primary vertex fit

- Primary vertex z coordinate — reject events with primary vertex outside of the target area

- Centrality cut — selects central events (20% centrality)

The number of events after each biasing cut is presented in table 14.
The GTPC cut rejects $\approx 30\%$ of events in low beam momenta and $\approx 50\%$ of events in high beam momenta data. This difference is due to lack of the minimum bias trigger in the high momenta data taking. The central trigger defined by the energy deposited in the PSD allows some of the non–interacting events to pass as central interactions due to longitudinal leakage in the PSD.

The centrality cut accepts $\approx 30\%$ of events in low beam momenta and $\approx 50\%$ of events in the high beam momenta data. This difference is due to differently set threshold of the central trigger in different data taking periods.

102

Table 14: Statistics of events after biasing cuts. $19A$ GeV/c and $30A$ GeV/c data cannot be compared with data for the higher beam momenta due to different trigger and beam detector setup.

	All Events	Non–biasing Cuts	GTPC Cut	Vertex Status	Vertex Z	20% Centrality
19A GeV	3440998	1015836	671910	583109	543679	166094
	100.0%	29.5%	19.5%	16.9%	15.8%	4.8%
30A GeV	4065716	1301211	815970	731064	679936	219834
	100.0%	32.0%	20.1%	18.0%	16.7%	5.4%
40A GeV	2859150	1815567	840145	734727	692817	387821
	100.0%	63.5%	29.4%	25.7%	24.2%	13.6%
75A GeV	3527415	2459424	1013160	953971	901506	413863
	100.0%	69.7%	28.7%	27.0%	25.6%	11.7%
150A GeV	2344142	1332829	673252	625446	586735	256382
	100.0%	56.9%	28.7%	26.7%	25.0%	10.9%

11.2.3. Track cuts

To select well measured hadron tracks a set of track cuts have to be used. The following cuts are used in the h$^-$ analysis:

- Negative Charge — selects negatively charged particles

- Right Side Tracks (RST) — selects particles with $q \cdot p_x > 0$

- Total Points — select tracks with more than 15 clusters

- VTPC & GTPC Points — selects tracks with more than 15 clusters in GTPC or more than 4 clusters in GTPC

- Impact Parameter — selects tracks with distance of closest approach to the vertex (impact parameter) smaller than 4 cm in x direction and smaller than 2 cm in y direction

Numbers of measured tracks after each track cut are presented in table 15.

Table 15: Statistics of tracks after track cuts.

	All Tracks	Negative Charge	Right Side Tracks	Total Points	VTPC & GTPC Points	Impact Parameter
19A GeV	1416943	524145	283576	255563	255517	248109
	100.0%	37.0%	20.0%	18.0%	18.0%	17.5%
30A GeV	2330719	932142	512599	467913	467819	456208
	100.0%	40.0%	22.0%	20.1%	20.1%	19.6%
40A GeV	4961719	2049975	1133914	1043981	1043632	1022791
	100.0%	41.3%	22.9%	21.0%	21.0%	20.6%
75A GeV	7482926	3233858	1734492	1617734	1617339	1598474
	100.0%	43.2%	23.2%	21.6%	21.6%	21.4%
150A GeV	6339403	2828911	1463171	1374672	1373995	1365044
	100.0%	44.6%	23.1%	21.7%	21.7%	21.5%

The construction of the TPCs as well as magnetic field configuration favours

topology of tracks with $q \cdot p_x > 0$. For such tracks the geometrical acceptance is continuous is rapidity and transverse momentum. Furthermore the reconstruction efficiency is higher for RSTs than for Wrong Side Tracks (WST). Therefore only such tracks are selected for further analysis.

The selection based on the number of measured clusters on track ensures well measured momentum. fig. 69 show distribution of the number of measured clusters.
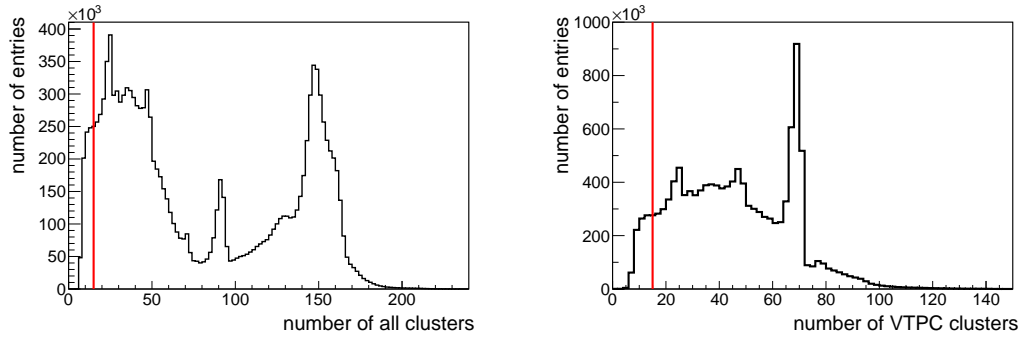

Figure 69: Distribution of clusters for all tracks. The cut value is marked with the red line.

The Impact Point track cut rejects tracks that fit poorly to the primary vertex such tracks include secondary tracks which were fitted to the primary vertex. fig. 70 shows the distribution of the impact parameter of measured tracks.

An additional cut to reject electrons and muons from the dataset is performed. The cut is defined as a region on the two–dimensional histogram of the specific energy loss versus momentum of the tracks. An example cut is presented on fig. 71.

The lepton cut region boundary was chosen at a minimum between pion and electron peak. An example plot of the specific energy loss for a given momentum is presented, together with the cut value on fig. 72.
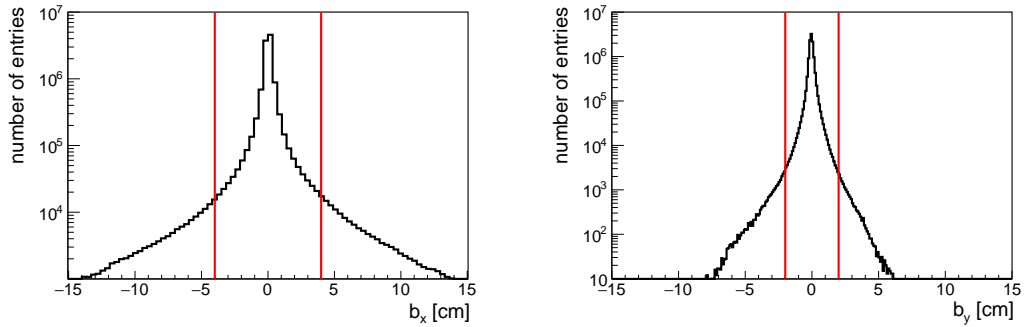
Figure 70: Impact parameter of all tracks. Magnetic field bends tracks in xz plane. The larger width of the impact parameter distribution in x direction is caused by the magnetic field.
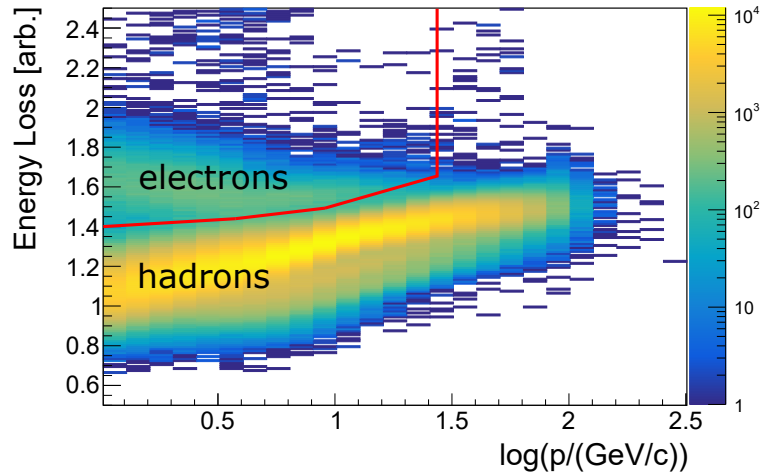
Figure 71: An example distribution of the energy loss versus momentum of the particles. The electron cut is shown as a red line.

11.3. Correction factors

In the following chapter use of the word *generated* means that the variable represent pure Monte–Carlo generator data without any changes, without detector simulation and without reconstruction.

The use of the word *selected* or *reconstructed* means that the variable represent

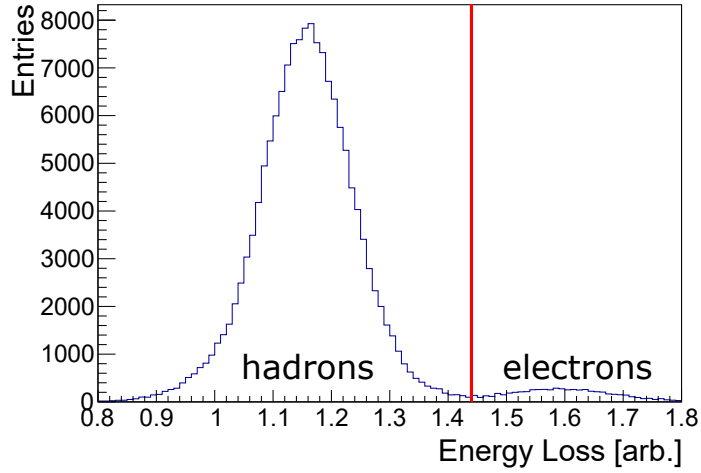Figure 72: An example energy loss distribution for particles with momenta between 2.0 and 2.5 GeV/c. The electron cut is shown as a red line.

reconstructed track after full detector simulation and all cuts.

11.3.1. Correction for out-of-target interaction

The resolution of the primary vertex fit is not enough to reject all of the out-of-target interactions from the analysed datasets. The NA61/SHINE takes around 10% of collisions with target removed from the beamline to study effects of out-of-target interactions. As can be seen on fig. 73 a small amount of out-of-target interaction background is present even after rejecting events with primary vertex far from the target position.

However, the correction for this background is not possible due to very low statistics after cuts (≈ 1000 target removed events).

The target area is filled with helium. Therefore, most of the out-of-target interactions are the minimum bias ^{7}Be+He interactions.

A study of the target removed data (section 7) shows that approximately 0.35% of target inserted events are produced in out-of-target ^{7}Be+He interactions. This
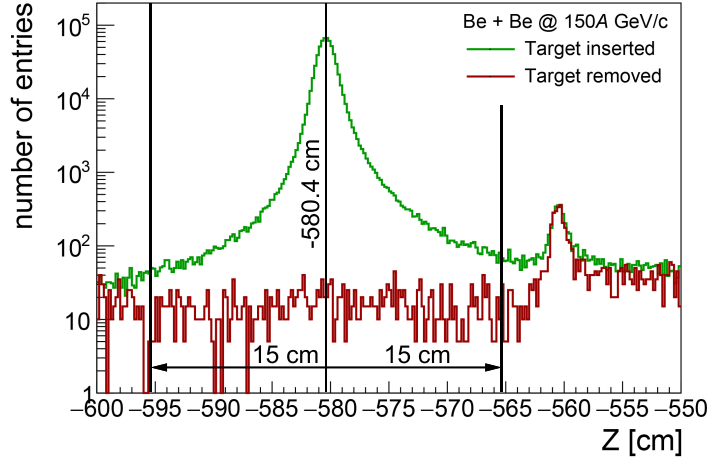
Figure 73: Distribution of the Z coordinate of the primary vertex for target inserted and removed configurations. Target removed data is normalized to the target inserted data to accurately represent amount of out-of-target background in target inserted data.

bias will be added to the systematic error of the measurements.

11.3.2. Geometrical acceptance correction factor

The NA61/SHINE detector do not have full azimuthal angle acceptance. To correct for tracks not measured due to non-instrumented parts of the phase–space a geometrical acceptance correction factor is introduced. To calculate correction factor an assumption that particles are produced isotropically in the azimuthal angle is made.

The correction is constructed using Monte-Carlo data simulated with full detector GEANT3 simulation and standard NA61/SHINE reconstruction chain. The algorithm for calculation of the correction factor is as follows:

1. Loop over all primary generated tracks

2. Fill the 3D histogram ($h_{\text{generated}}$) with (ϕ, p_{T}, y) of analysed primary generated

track

3. Check if a reconstructed track that passed all track cuts and corresponds to the analysed generated track is present

4. If such reconstructed track is present fill the 3D histogram (h_{selected}) with (ϕ, p_{T}, y) of analysed primary *generated* track. The generated track parameters are used to make the correction independent of bin migration due to reconstruction procedure and detector resolution

5. After the end of the primary generated track loop

6. Calculate efficiency histogram (e.g. fig. 74) by dividing selected histogram by the generated histogram ($h_{\text{efficiency}} = \frac{h_{\text{selected}}}{h_{\text{generated}}}$)

7. Calculate the acceptance map (fig. 75):

   a) For each (ϕ, p_{T}, y) bin of the efficiency histogram

   b) If the efficiency is lower than 90% or there is less than 20 simulated tracks the bin is rejected

   c) Otherwise the bin is accepted

8. For each (p_{T}, y) slice of the acceptance map calculate the correction factor as a ratio of the number of the accepted ϕ bins to the number of the total ϕ bins.

The result of the above procedure is the geometrical acceptance correction factor calculated for each (y, p_{T}) bin of the phase–space. Additionally, a three dimensional acceptance map was calculated.

The geometrical acceptance correction factor is presented for lowest and highest beam momenta on fig. 76. The difference between acceptance of wrong and right side tracks are presented on fig. 77. Only right side tracks are used in the analysis.

The use of the geometrical acceptance correction factor require using an acceptance map. In all further calculations (for both correction factors and data) only tracks
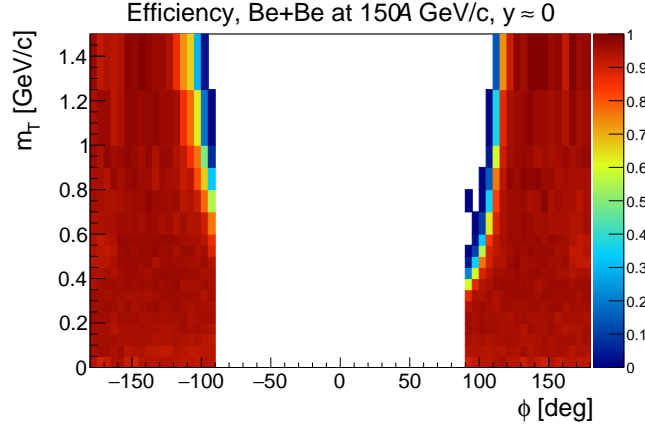
Figure 74: Efficiency of the track reconstruction for an example rapidity slice. All bins where track finding efficiency is below 90% are rejected.
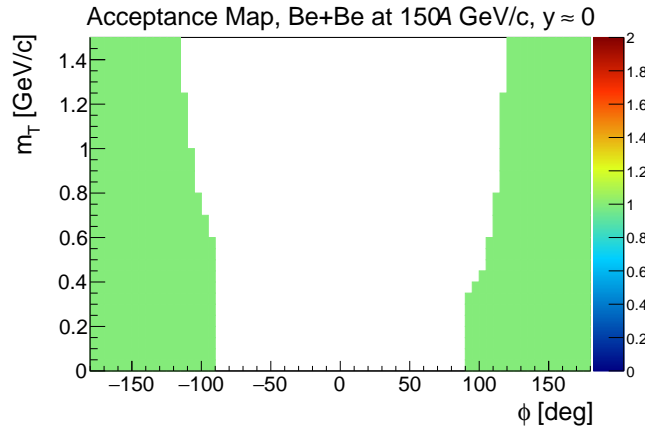
Figure 75: Acceptance map for an example rapidity slice. Only tracks with track parameters within accepted (green) bins will be analysed.

with azimuthal angle (ϕ), transverse momentum (p_T) and rapidity (y) marked as accepted in acceptance map will be used.

The geometrical acceptance correction factor is applied on the level of filling the relevant histogram. The histogram is filled with a weight that correspond to the geometrical acceptance correction factor for the rapidity and transverse momentum of the analysed track.

Figure 76: The geometrical acceptance correction factor. The correction is presented for 5% most central events. The correction depends very weakly on centrality.

This correction factor should be strongly dependent on the accuracy of the Monte–Carlo detector description as well as accuracy of the magnetic field map. It should be only weakly dependent on the primary generator simulating particles produced in the collision.
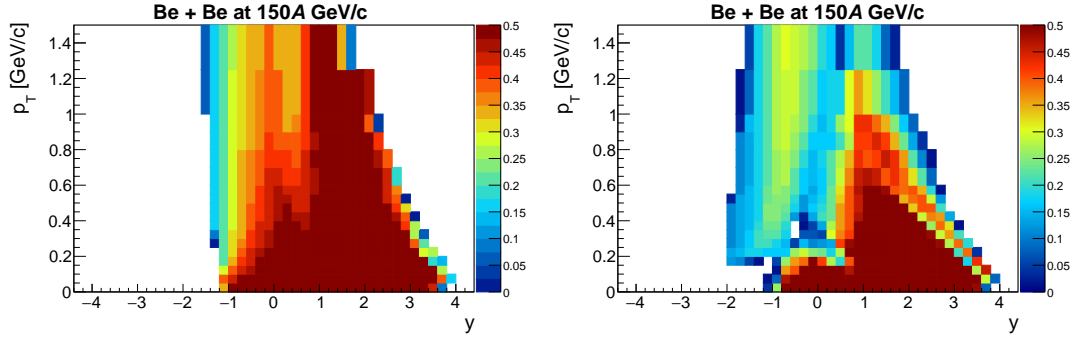
Figure 77: Difference in acceptance of right and wrong side tracks.
(left): Right side tracks   (right): Wrong side tracks

11.3.3. Reconstruction efficiency correction factor

To correct data for the loss of tracks due to inefficiencies in tracking algorithms as well as losses due to event and track quality cuts a reconstruction efficiency correction factor is used.

The correction factor is calculated in following steps:

1. Fill the 2D histogram $(n_{\text{generated}}[\pi^-])$ with (y, p_{T}) of all generated primary π^- mesons

2. Fill the 2D histogram $(n_{\text{selected}}[\pi^-])$ with (y, p_{T}) of the reconstructed primary π^- tracks after all cuts corrected with the geometrical acceptance correction factor

3. Divide selected histogram by generated histogram to obtain correction factor $(c_{\text{eff}} = n_{\text{selected}}[\pi^-]/n_{\text{generated}}[\pi^-])$

The correction factor is shown on fig. 78 for lowest and highest beam momenta.

This correction factor should be weakly dependent on the Monte–Carlo models and detector description used. The accuracy of this correction depends mostly on the accuracy of the TPC digitizer software which simulates the response of the TPC electronics to the passing particles.
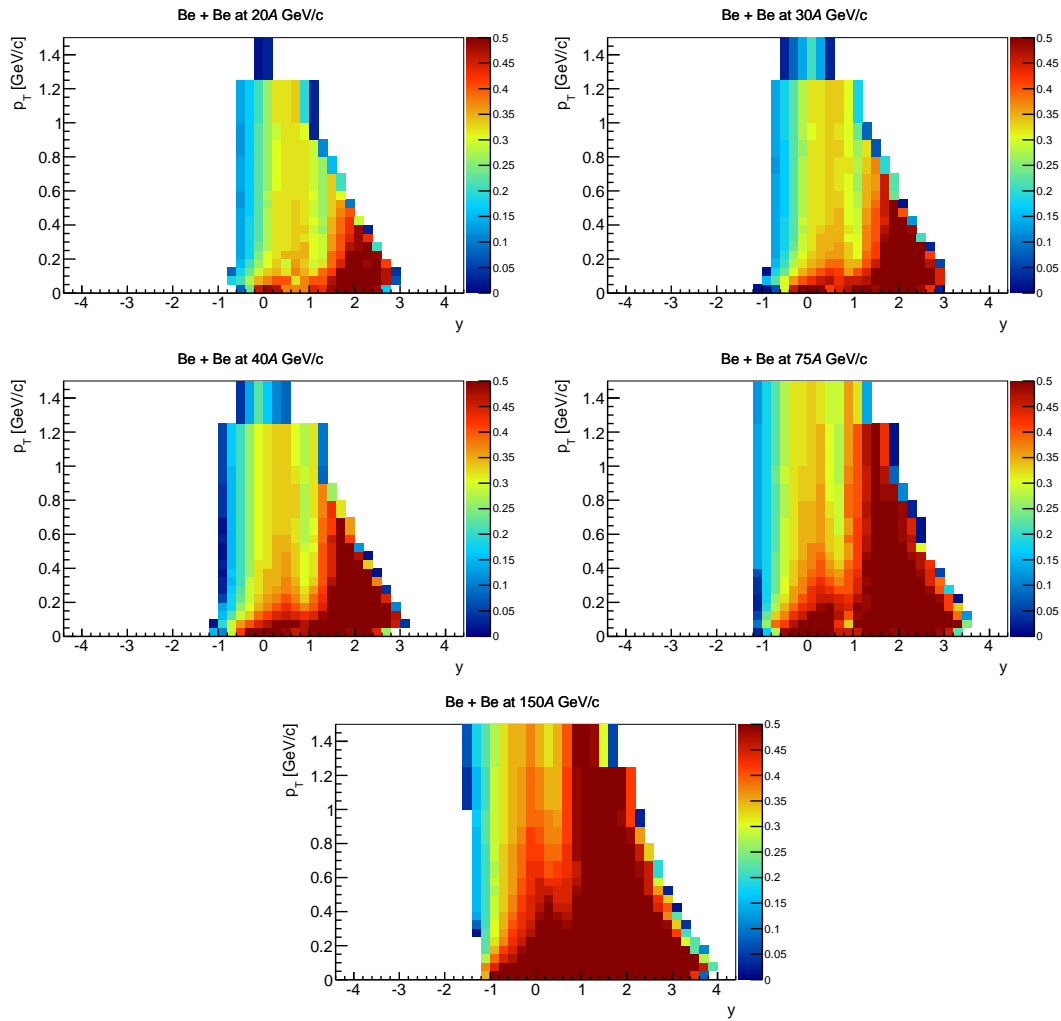
112

Figure 78: Reconstruction efficiency correction factor. The correction is presented for 5% most central events. The correction depends very weakly on centrality.

11.3.4. h⁻ correction factor

To obtain spectra of negatively charged primary pions from spectra of all negatively charged hadrons reconstructed as a primary particles additional correction factor is necessary. To calculate the so-called h⁻ correction factor following procedure is performed:

1. Fill the 2D histogram ($n_{\text{selected}}[\pi^-]$) with ($y$, p_{T}) of the reconstructed primary π^- tracks after all cuts corrected with the geometrical acceptance correction factor

2. Fill the 2D histogram ($n_{\text{selected}}[\text{h}^-]$) with ($y$, p_{T}) of all tracks reconstructed as primary particles after all cuts corrected with the geometrical acceptance correction factor
   This histogram include primary π^- mesons, primary K^- mesons, primary antiprotons as well as secondary π^- mesons, wrongly reconstructed as primary particles, from decays of lambdas, K_0 and other particles

3. Divide pion histogram by the all hadron histogram to obtain correction factor ($c_{\text{h}^-} = n_{\text{selected}}[\pi^-]/n_{\text{selected}}[\text{h}^-]$)

The correction factor is shown on fig. 79 for lowest and highest beam momenta.

The correction is highly model dependent. Although, the amount of the correction is relatively small. In most of the phase–space the correction is of the order of 10% with few regions of phase–space rising to at most 30%. Furthermore, the model used for calculating the correction (EPOS 1.99) was proven to describe NA61/SHINE p+p data [29, 46] within 10% precision. The uncertainty of this correction will be added to the systematic error of the measurement, the procedure will be described in the section 11.6.

11.3.5. Correction of the number of events

To account for the loss of inelastic events due to inefficiencies of the primary vertex finder procedure, as well as the loss of event due to cut on the Z coordinate of the primary vertex a correction of the number of events is employed.

The used Monte–Carlo model (EPOS 1.99) generates only events with at least one produced particle. To calculate loss of such events a ratio of all MC events with the defined centrality to the number of MC events with the same centrality after

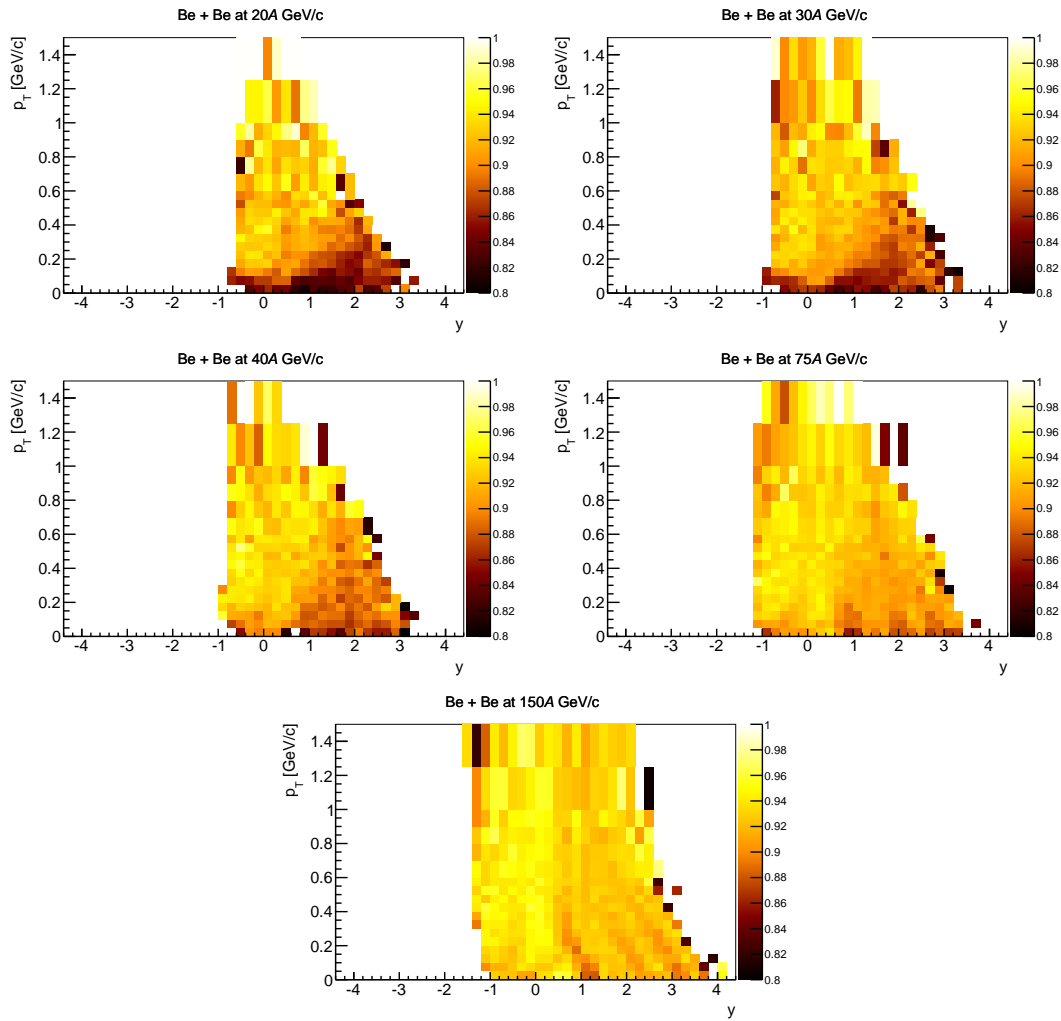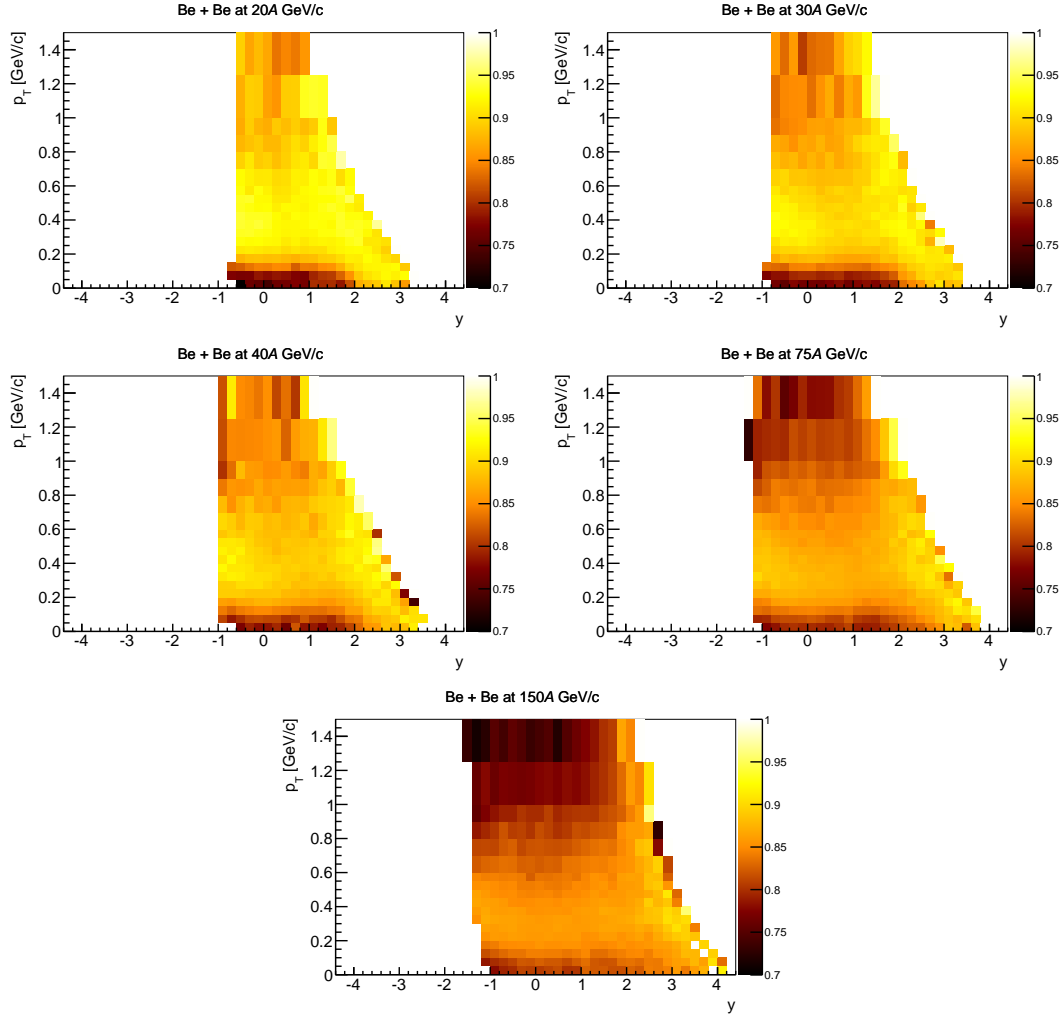Figure 79: h$^-$ correction factor. The correction is presented for 5% most central events. The correction depends very weakly on centrality.

all event cuts is used:

$$c_{\text{events}} = N_{\text{generated}}/N_{\text{selected}} \tag{16}$$

11.3.6. Data correction procedure

The geometrical acceptance correction factor is applied as a weight used for each track while filling raw data histograms.

The reconstruction efficiency correction factor and the h$^-$ correction factor are the multiplicative correction factors used by multiplying each bin of the raw data histogram by the corresponding correction factor bin:

$$n[\pi^-] = n_{\mathrm{raw}}[h^-] \cdot c_{\mathrm{h}^-}/c_{\mathrm{eff}}, \tag{17}$$

where $n[\pi^-]$ is the corrected number of π^- mesons in a given phase–space bin, $n_{\mathrm{raw}}[h^-]$ is the measured number of tracks after all cuts, c_{h^-} is the h$^-$ correction factor, and c_{eff} is the efficiency correction factor.

The corrected number of negatively charged pions is divided by the corrected number of events and bin size to obtain density of produced π^- mesons per event:

$$\frac{\mathrm{d}^2n}{\mathrm{d}y\mathrm{d}p_{\mathrm{T}}}(y, p_{\mathrm{T}}) = \frac{n[\pi^-](y, p_{\mathrm{T}})}{N \cdot c_{\mathrm{events}} \cdot \Delta y \cdot \Delta p_{\mathrm{T}}}, \tag{18}$$

where $\frac{\mathrm{d}^2n}{\mathrm{d}y\mathrm{d}p_{\mathrm{T}}}$ is the density of produced π^- mesons, $n[\pi^-](y, p_{\mathrm{T}})$ is the corrected number of produced primary π^- mesons, N is the number of measured events, c_{events} is the event loss correction factor, and Δy and Δp_{T} are the width of the respectively rapidity and transverse momentum bins.

11.4. Results

The analysis was performed for:

- Five beam momenta: $19A$, $30A$, $40A$, $75A$, and $150A$ GeV/c

- Four centrality classes for each beam momentum: 0-5%, 5-10%, 10-15%, and 15-20%

Additional analyses were performed for study of the systematic errors and biases.

As a result of the analysis two-dimensional spectra in either rapidity and transverse momentum, or rapidity and transverse mass were obtained. Rapidity and transverse mass was calculated with the assumption of negatively charged pion mass. Bin sizes were optimized to minimize statistical errors while allowing simple comparison with other experimental results.

The rapidity was binned from -4.4 to 4.4 with the bin width equal 0.2 rapidity unit.

The transverse momentum and mass binning is presented in table 16.

Table 16: Binning of the transverse momentum and transverse mass

Transverse Momentum		Transverse Mass	
Range [GeV/c]	Bin Width [GeV/c]	Range [GeV/c^2]	Bin Width [GeV/c^2]
0.0 — 0.6	0.05	0.00 — 0.72	0.06
0.6 — 1.0	0.10	0.72 — 1.20	0.12
1.0 — 1.5	0.25		

The raw number of tracks selected by all cuts is presented on fig. 80.
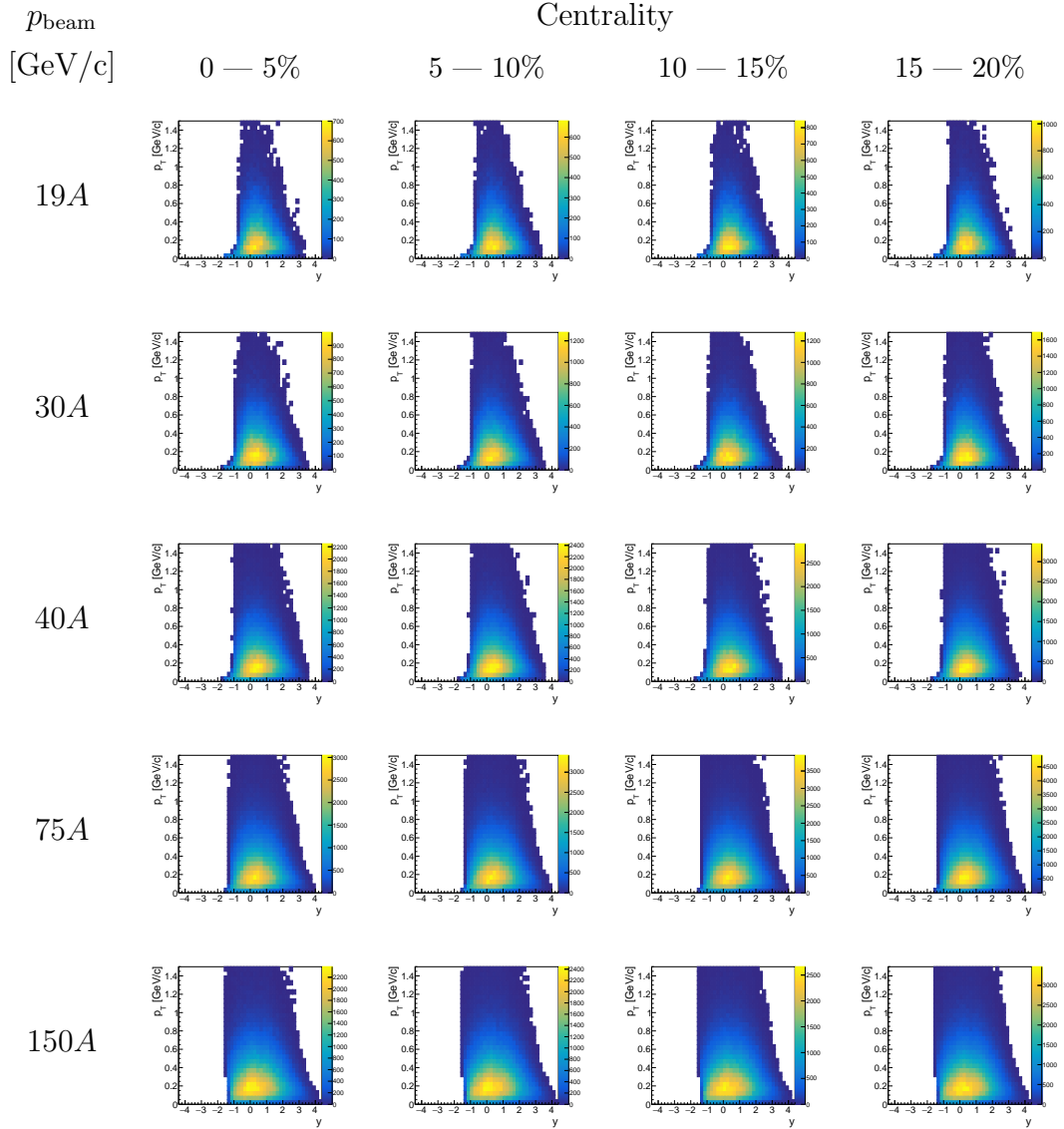
Figure 80: Raw measured number of tracks in each analysis bin.

11.4.1. Two–dimensional spectra of π^- mesons

The two-dimensional spectra in rapidity and transverse momentum are presented on fig. 81 for five beam momenta and four centrality classes. An important feature of the spectra is the rapidity acceptance which extends into backward rapidity.
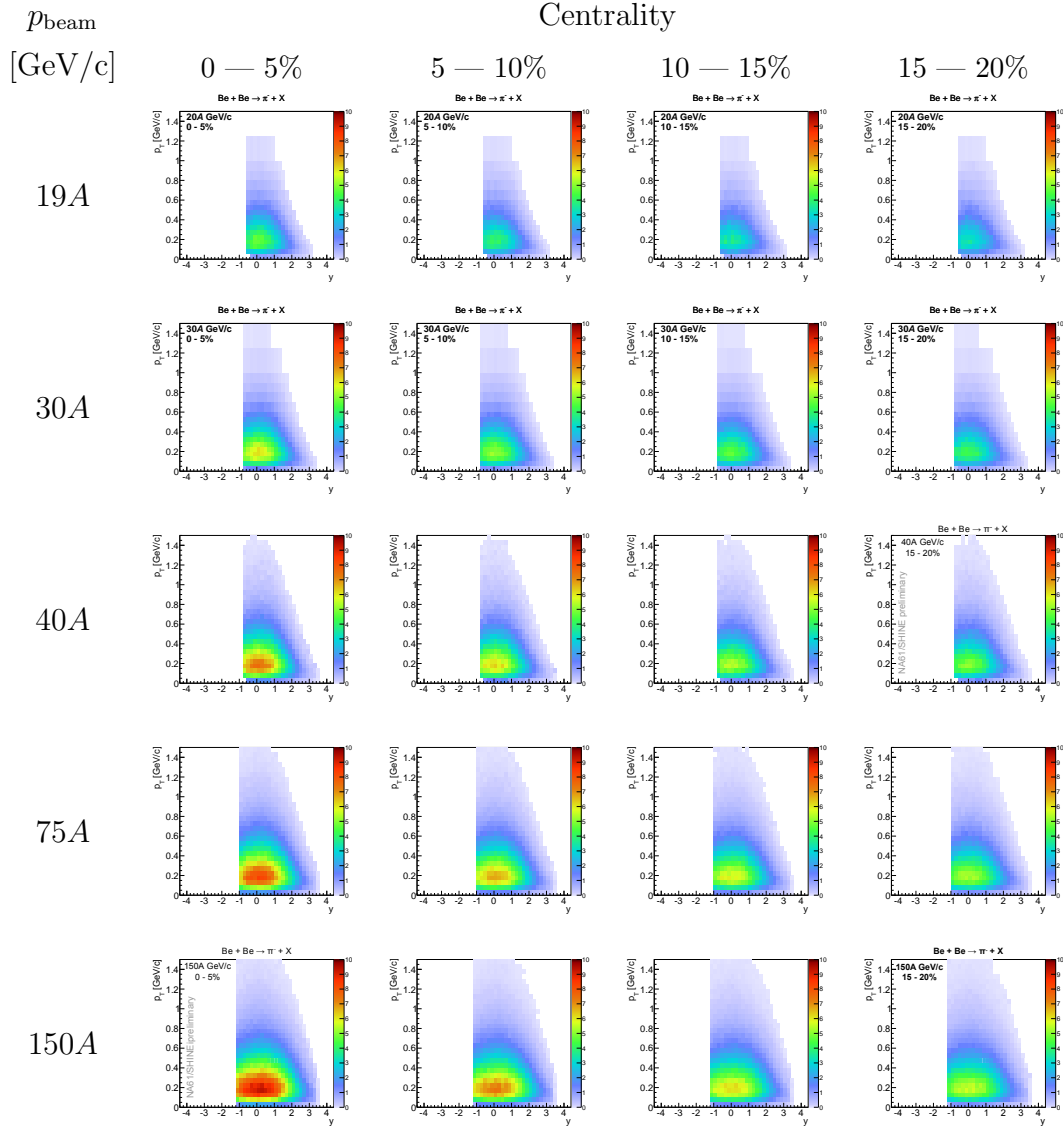
Figure 81: Corrected two-dimensional spectra of negatively charged pions produced in ^{7}Be + ^{9}Be collisions.

11.4.2. Rapidity spectra of π^- mesons

To extract one-dimensional rapidity spectra from the two-dimensional y-p_{T} spectra missing high p_T acceptance have to be extrapolated. The transverse momentum

spectrum for each rapidity bin was parametrized with the function:

$$\frac{\mathrm{d}^2 n}{\mathrm{d}y \mathrm{d}p_\mathrm{T}}(p_\mathrm{T}) = \frac{A \cdot p_\mathrm{T}}{\lambda^2 + \lambda m_{\pi^-}} \cdot \exp\left(-\frac{\sqrt{p_\mathrm{T}^2 + m_{\pi^-}^2} - m_{\pi^-}}{\lambda}\right),$$ (19)

where A is the normalization parameter, λ is the slope parameter, and m_{π^-} is the mass of the negatively charged meson. An additional constraint was added to the fit to ensure that the integral of the fitted function where data is available is equal to the integral of the data.

The p_T extrapolation change the value of the spectrum by $\approx 0.1\%$. Only for $y > 3$ the extrapolation effect rises to around 1%.

The rapidity spectra can be seen on fig. 82. A closer look reveal asymmetry of the spectra with respect to midrapidity. To quantify the amount of asymmetry the spectra were parametrized with the sum of two Gaussian functions (eq. (20)). The Gaussian functions have the same width and are displaced from the midrapidity by the same amount.

$$\frac{\mathrm{d}n}{\mathrm{d}y} = A \cdot \left(A_\mathrm{rel} e^{-\frac{(y-y_0)^2}{\sigma_0}} + e^{-\frac{(y+y_0)^2}{\sigma_0}}\right),$$ (20)

where A is the normalization parameter, A_rel is the relative amplitude of Gaussians, σ_0 is the width of the single Gaussian, and y_0 is the displacement from the midrapidity.

The eq. (20) was fitted to data with the constraint that integral of the fitted function in the range where data is available must be equal to the integral of data. The examples of the fitted functions are presented on fig. 83. The fit was tested with Monte–Carlo by producing histogram according to the fitted distribution with the same statistics and range as experimental data and than refitting such histogram. The parameters of the fit used for producing the histogram are known. Therefore, a estimate of the fit bias can be made by comparing parameters used to generate fake data to the parameters obtained from refit. The Monte–Carlo study show parameter biases consistent with zero.
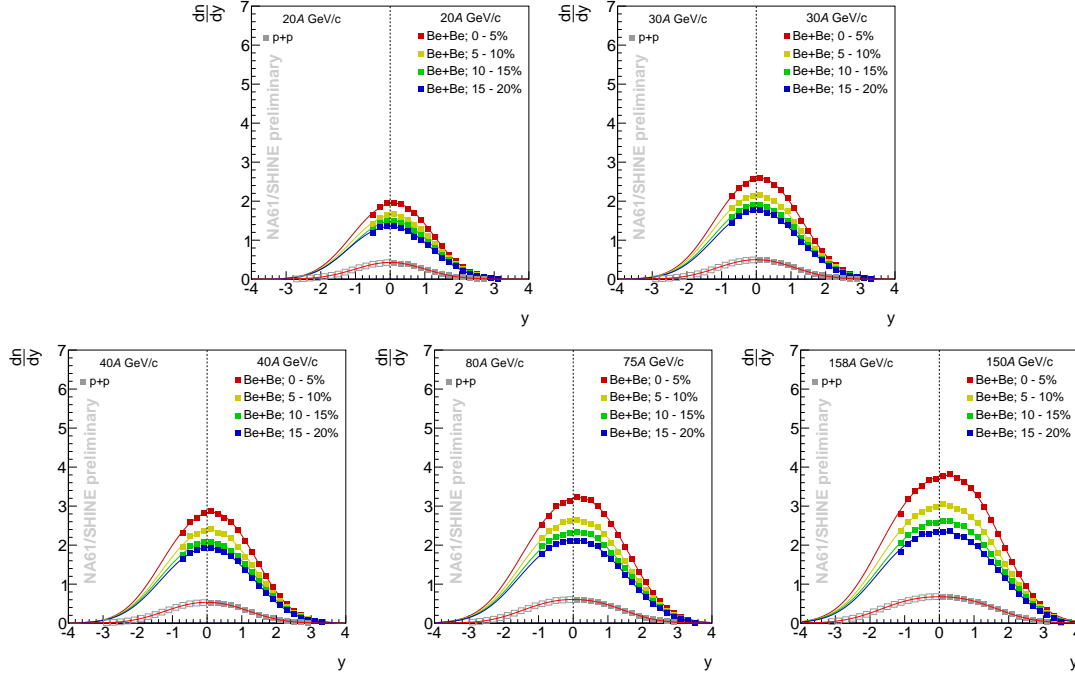
Figure 82: Rapidity spectra of negatively charged pions produced in ^{7}Be + ^{9}Be collisions. Statistical errors are smaller than the size of the points.

The relative amplitude of Gaussians is independent with beam momentum, but strongly dependent on centrality of the collision (fig. 84). Such asymmetry can be caused by two effects:

- Asymmetric system — collisions of ^{7}Be beam on ^{9}Be target can cause backward rapidity enhancement

- Centrality selection — the PSD selects centrality based on the forward-going energy

The asymmetry was studied using Glauber model and the Wounded Nucleon Model (WNM), where production of particles in backward hemisphere is proportional to the number of wounded nucleons in the target and production of particles in forward hemisphere is proportional to the number of wounded nucleons in the projectile.
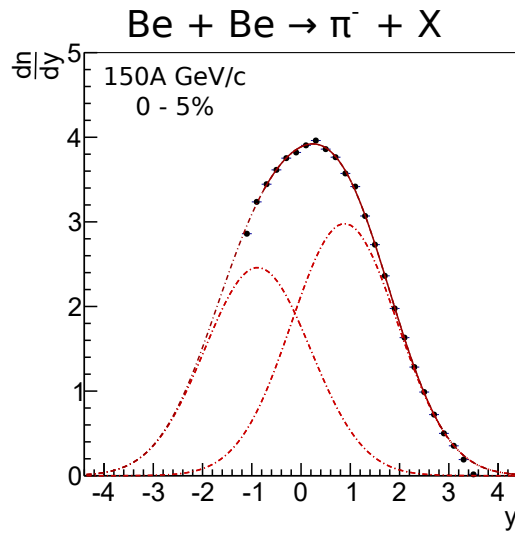
Figure 83: Parametrization of the rapidity distribution. Solid line presents range of the fit, dark dashed line show extrapolation of the fitted function. Two Gaussian functions which constitute fitted function are marked by light dashed line.
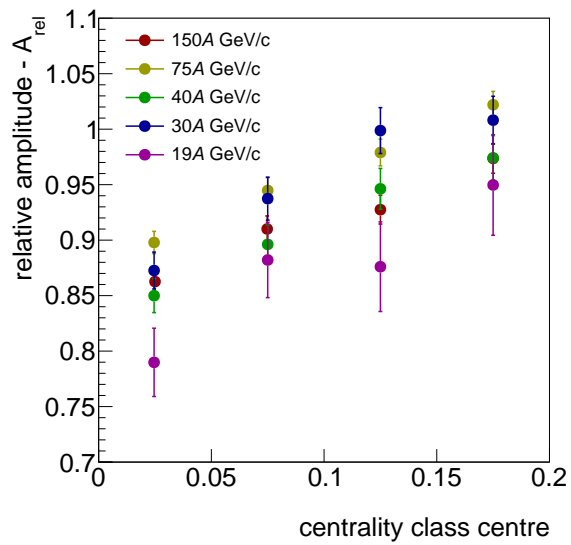

Figure 84: Relative amplitude of the Gaussian functions fitted to the rapidity spectra.

In the WNM the effect of the asymmetric system is a small enhancement of the backward rapidity production, which is opposite to what is visible in data. On the other hand, the effect of the centrality selection based only on *forward*-going energy is a large effect enhancing forward rapidity production.

By selecting centrality by the PSD a sharp cut is placed on the number of wounded nucleons from the projectile. However, the wounded nucleons from the target can freely fluctuate. Therefore, the mean number of wounded nucleons from projectile is higher than the mean number of wounded nucleons from target, which causes enhancement of forward rapidity production.

11.4.3. Width of the rapidity spectra of π^- mesons

According to hydrodynamical model [47, 48] the sound velocity ($c_{\rm s}$) is related to the width of the rapidity distribution:

$$\sigma_y^2(\pi^-) = \frac{8}{3}\frac{c_{\rm s}^2}{1-c_{\rm s}^4}\ln\left(\sqrt{s_{NN}/2m_p}\right) \tag{21}$$

The lattice QCD calculation suggest that the minimum of the sound velocity can be attributed to the phase transition between hadron gas and quark–gluon plasma. The sound velocity as a function of beam energy for p+p and Pb+Pb data is presented on fig. 85.

For simplicity this chapter will use a simpler and more directly experimental variable: the width of the rapidity distribution divided by the beam rapidity — $\sigma_y/y_{\rm beam}$. To calculate the width of the rapidity distribution from the parametrization given in previous chapter the following formula is used:

$$\sigma_y = \sqrt{\sigma_0^2 + y_0^2} \tag{22}$$

The width of the rapidity spectrum of negatively charged pions in ^{7}Be + ^{9}Be collisions is weakly dependent on centrality (fig. 86).

The dependence of the ralative width of the rapidity distribution on the beam energy is presented on fig. 87. For all system sizes the relative width decreases

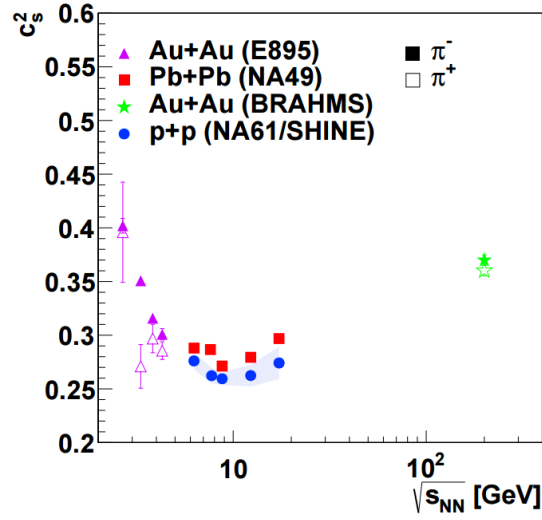Figure 85: Velocity of sound as a function of collision energy. No isospin corrections are made.
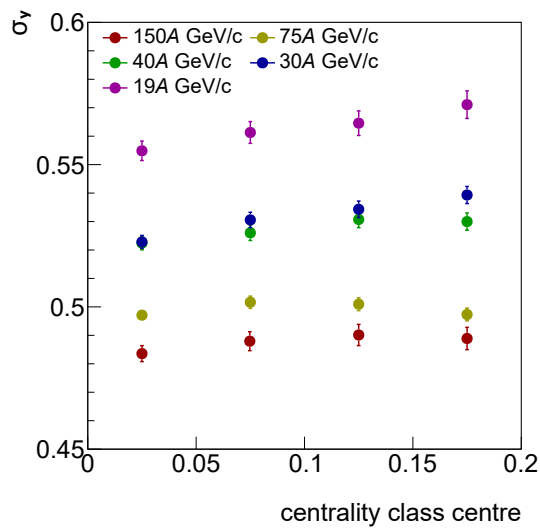

Figure 86: The width of the rapidity distribution. Weak dependence on centrality is visible.

monotonically with beam energy. However, a non-monotonic behaviour with system sizes can be observed. For all energies the p+p data is the lowest, the Pb+Pb data is in the middle and the ^{7}Be + ^{9}Be data is the highest.
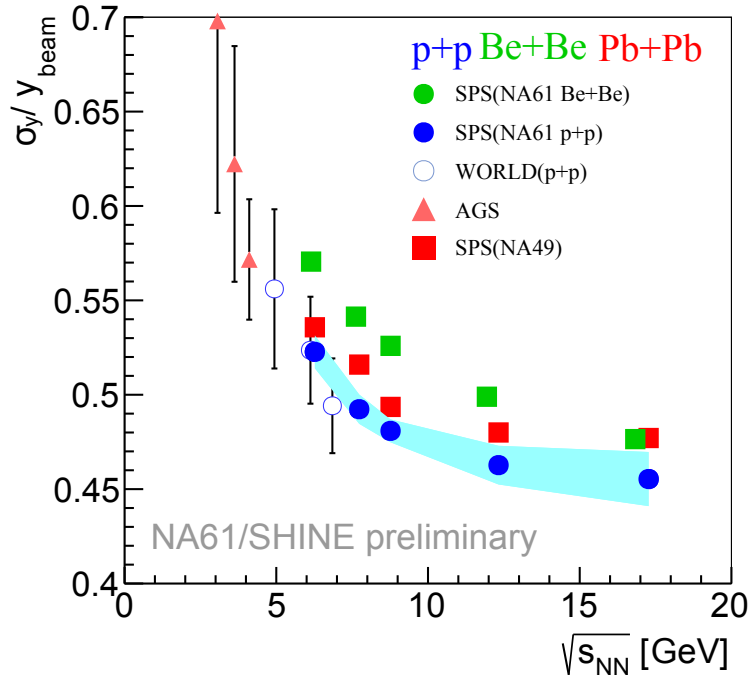
Figure 87: Relative width of the pi^- meson rapidity distribution. Monotonic behaviour in collision energy and non-monotonic behaviour in system size is visible.

The lack on monotonicity can be explained by the isospin asymmetry of different systems. In Pb+Pb collisions there will be more n+n interactions than p+p interactions. The $^7Be + {}^9Be$ is approximately isospin symmetric, there is the same number of protons and neutrons in the collision. The most isospin asymmetric system is produced in the p+p collisions, there are no n+n interactions.

For a correct comparison between different system sizes the isospin asymmetry have to be corrected. A straightforward method involve plotting the width of the summed distributions of π^- and π^+ mesons. Unfortunately, the necessary π^+ data is available only for 158 GeV/c beam momentum [49].

On fig. 88 the widths of the π^-, π^+, and $\pi^- + \pi^+$ distributions are presented for p+p at 158 GeV/c together with the $^7Be + {}^9Be$ and Pb+Pb data. It seems that the system size monotonicity is restored, although additional studies at lower beam

momenta, where isospin effects are larger, are necessary.
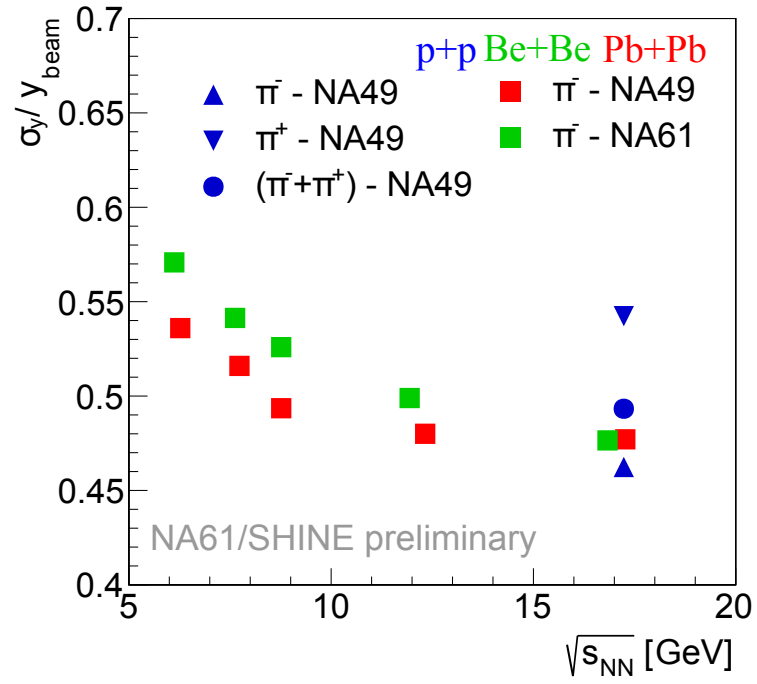
Figure 88: Effect of the isospin asymmetry in p+p collisions on the relative width of the rapidity distribution.

11.4.4. Transverse momentum and transverse mass spectra of π^- mesons

The midrapidity transverse momentum and transverse mass spectra were obtained from two-dimensional spectra by projecting rapidity bins in a range from -0.4 to 0.4 to the, respectively, transverse momentum or transverse mass axis.

The fig. 89 presents transverse mass spectra of negatively charged pions produced in ^{7}Be + ^{9}Be interactions for five beam momenta and four centrality classes together with transverse mass spectra for p+p and Pb+Pb collisions. The spectra were fitted by the exponential functions in a range $0.2 < m_T - m_{\pi^-} < 0.7$ GeV/c^2.
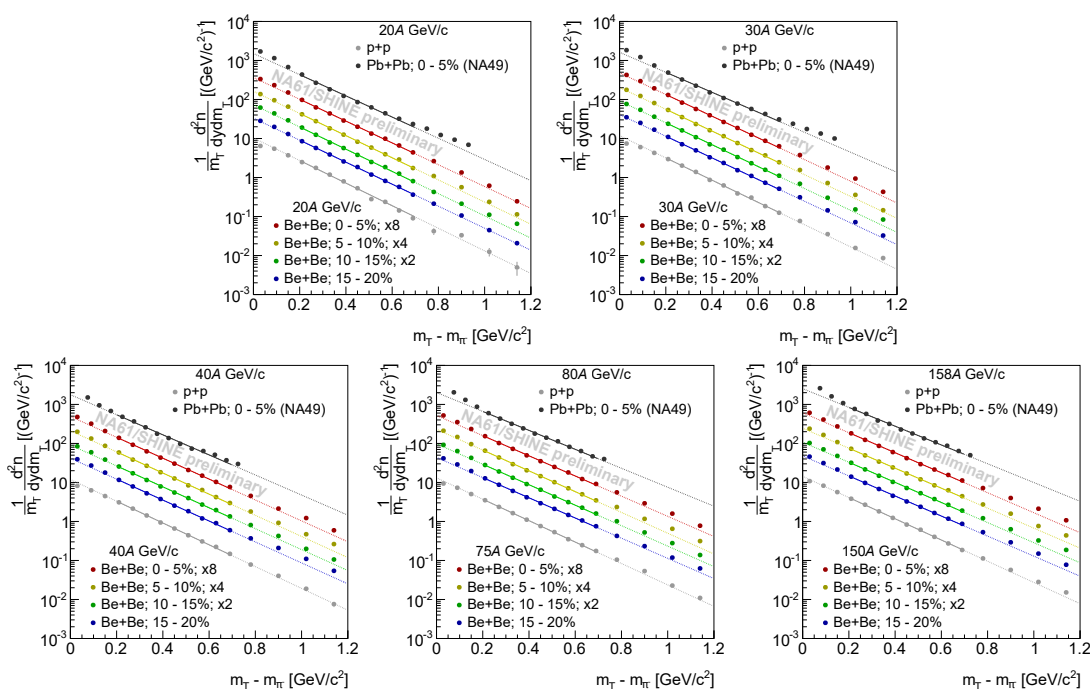
Figure 89: Transverse mass spectra of negatively charged pions produced in ^{7}Be + ^{9}Be collisions. Statistical errors are smaller than the size of the points. The p + p data follows exponential distribution while ion + ion data show deviation at low and high transverse mass.

The transverse mass spectrum measured by the NA61/SHINE experiment can be divided into two parts: low transverse mass region with $m_T < 0.3$ GeV/c^2 and intermediate transverse mass region with $m_T > 0.3$. The low m_T region is

dominated by the resonance production. The intermediate region can show the effects of the final state interactions. In the nuclear matter the produced pions can increase their transverse mass by multiple interactions giving rise to the collective radial flow of particles. Such effect presents itself as a enhancement of intermediate region of transverse mass with respect to p+p data.

To compare the transverse mass spectra between systems the each spectrum was normalized to the integral of the spectrum in a range of $0.24 < m_T < 0.72$. The normalized ion-ion spectra were then divided by the p+p spectra used as a reference. The resulting ratio is presented on fig. 90.
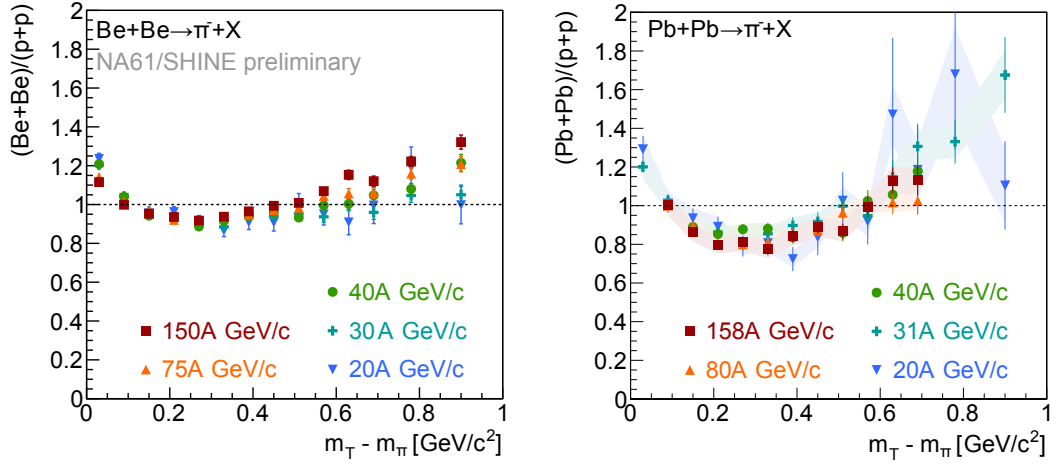
Figure 90: Ratio of normalized transverse mass spectra.
(left): ^{7}Be + ^{9}Be / p + p   *(right):* Pb + Pb / p + p

The enhancement with respect to p+p data at intermediate m_T is visible for both Pb+Pb and ^{7}Be + ^{9}Be data. The quantitative comparison between Pb+Pb and ^{7}Be + ^{9}Be data is difficult due to large statistical errors of Pb+Pb data.

The enhancement in ^{7}Be + ^{9}Be data is the largest for the highest beam momentum data, which is better visible on fig. 91. Which may be interpreted as increase of the radial flow magnitude with beam momentum.
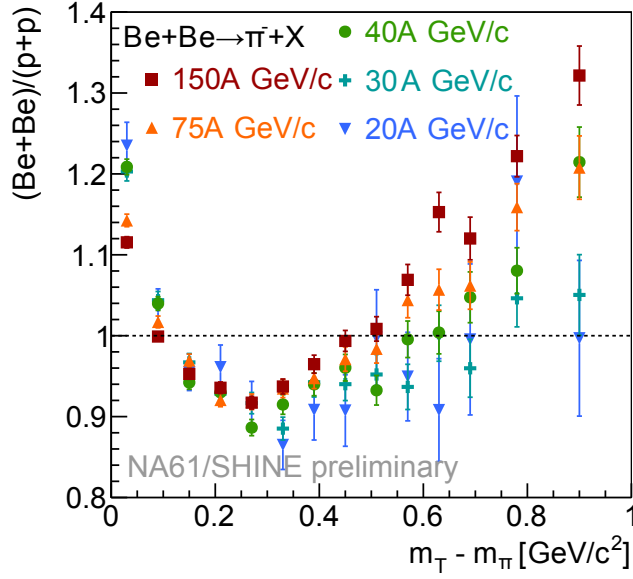
Figure 91: Ratio of normalized transverse mass spectra.
The energy ordering at large $m_T - m_{\pi^-}$ is visible. The enhancement is largest for high beam momenta.

11.5. Statistical error

Two sources contribute to the final statistical uncertainties of the results. First source of the error is the limited statistics of the measured data. Second source of the error is the limited statistics of produced Monte–Carlo simulations. The number of MC events was order of magnitude higher than the number of measured events. Therefore, the main source of the statistical error is the limited statistic of experimental data.

The statistical error of the uncorrected spectra was calculated assuming Poisson probability distribution for the weighted number of entries in each bin. The weight corresponded to the geometrical correction factor.

To calculate statistical error of the h^- correction factor a large correlation between number of negatively charged pions and number of all negative hadrons have to be taken into consideration. Taking into account Poisson distribution of number of

pions and number of hadrons the equation describing statistical error the the h⁻ correction is given by:

$$\sigma_{c_{h-}} = c_{h-}^2 \frac{n[h^-] - n[\pi^-]}{n[\pi^-]} \sqrt{\frac{1}{n[\pi^-]} + \frac{1}{n[h^-] - n[\pi^-]}}$$

The reconstruction efficiency correction factor follows a binomial distribution. Therefore, the statistical error is given by:

$$\sigma_{c_{\mathrm{eff}}} = c_{\mathrm{eff}} \sqrt{\frac{n[\pi^-]_{\mathrm{gen}} - n[\pi^-]_{\mathrm{sel}}}{n[\pi^-]_{\mathrm{gen}} \cdot n[\pi^-]_{\mathrm{sel}}}}$$

The correction for the inelasitic event loss follows a binimial distribution as well. Therefore, the error for this correction was calculated in the same way as the reconstruction efficiency correction.

Total statistical error of the rapidity—transverse momentum spectra of negatively charged pions was calculated with the assumption that the statistical errors of the various contributions in eq. (17) and eq. (18) are uncorrelated.

Statistical uncertainty of the two-dimensional specra is presented in fig. 92. The uncertainty value is approximately 2% for the most of the measured phase-space. The uncertainty rises to values of approximately 10—20% at the edges of the acceptance.
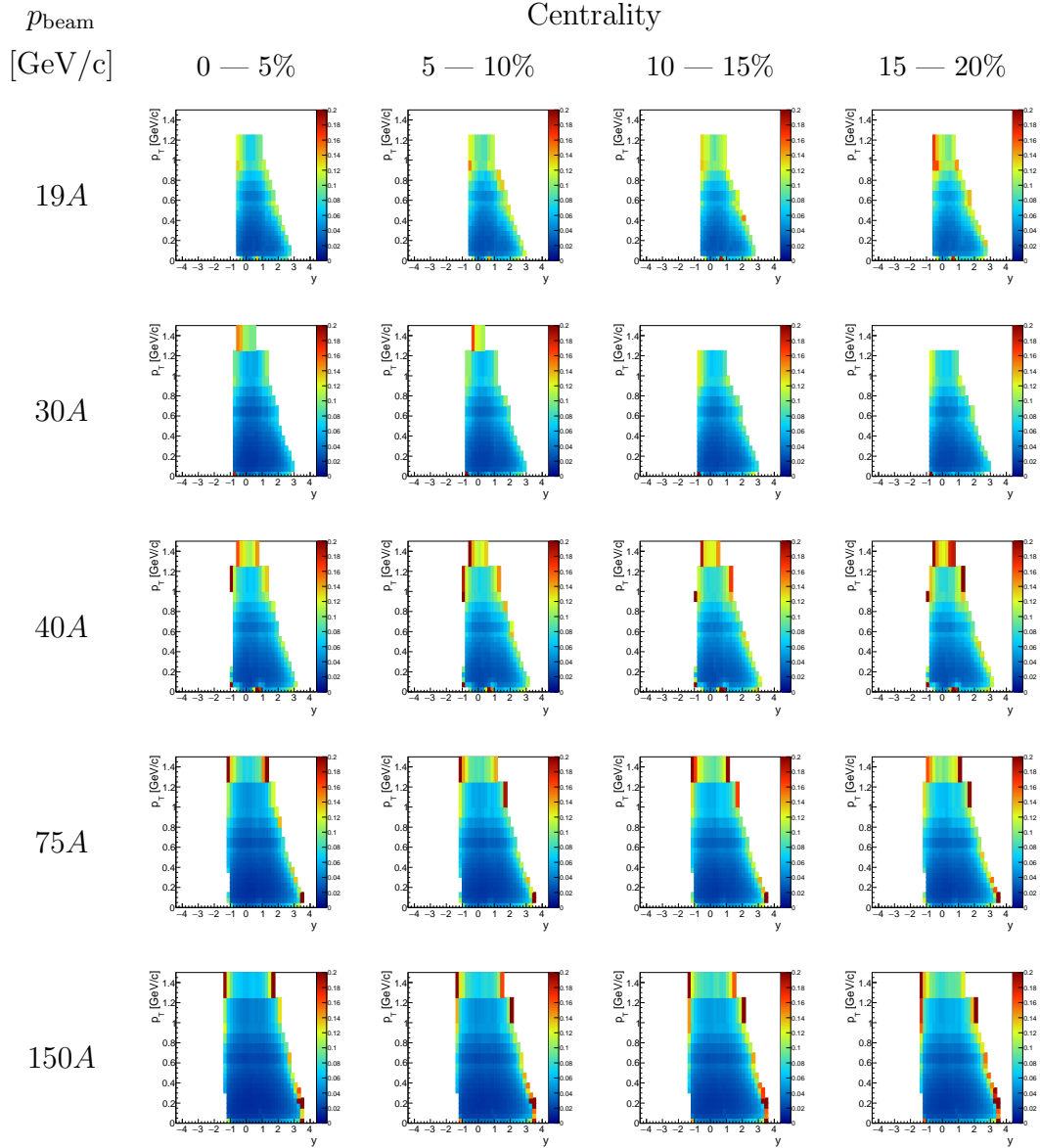
Figure 92: Statistical error of the negatively charged pion spectra.

11.6. Systematic error

fig. 93 presents systematic uncertainies for all beam momenta and centrality classes. The effects contributing to the uncentainty are listed below:

- The uncertainty of the h⁻ correction factor

- The uncertainty of the number of in-target event lost due to vertex Z cut and the uncertainty due to background events within accepted values of the vertex Z cut

- The uncertainty due to not rejected events with off–time interactions

- The uncertainty due to tracking inefficiencies not corrected by the Monte–Carlo simulations

- The uncertainty due to centrality definition.

The contributions listed above are uncorrelated.

The h⁻ correction factor is highly model dependent. Fortunately, the amount of the correction is relatively small (fig. 79) and Monte–Carlo models describe ratios of produced particles relatively well [29, 46]. To account for the inaccuracies of the models in previously unmeasured ^{7}Be + ^{9}Be interactions a 30% of the h⁻ correction factor will be taken as the model dependent systematic error. This error is a dominant contribution in total systematic error in two cases:

- In low beam momenta data the feed–down correction from secondary pions misidentified as primary is a significant contribution at low transverse momenta,

- In high beam momenta data the contribution from heavier hadrons (kaons and antiprotons) is large at the high transverse momentum region.

The maximum value of this contribution to the systematic error is approximately 10%.

The uncertainty of the in–target events lost due to cut on the Z coordinate of the fitted primary vertex is correlated with the uncertainty of the out–of–target background events accepted within the cut range. The effect of either of this contributions is < 1%.

The loss of in–target events results in higher multiplicity, while background from

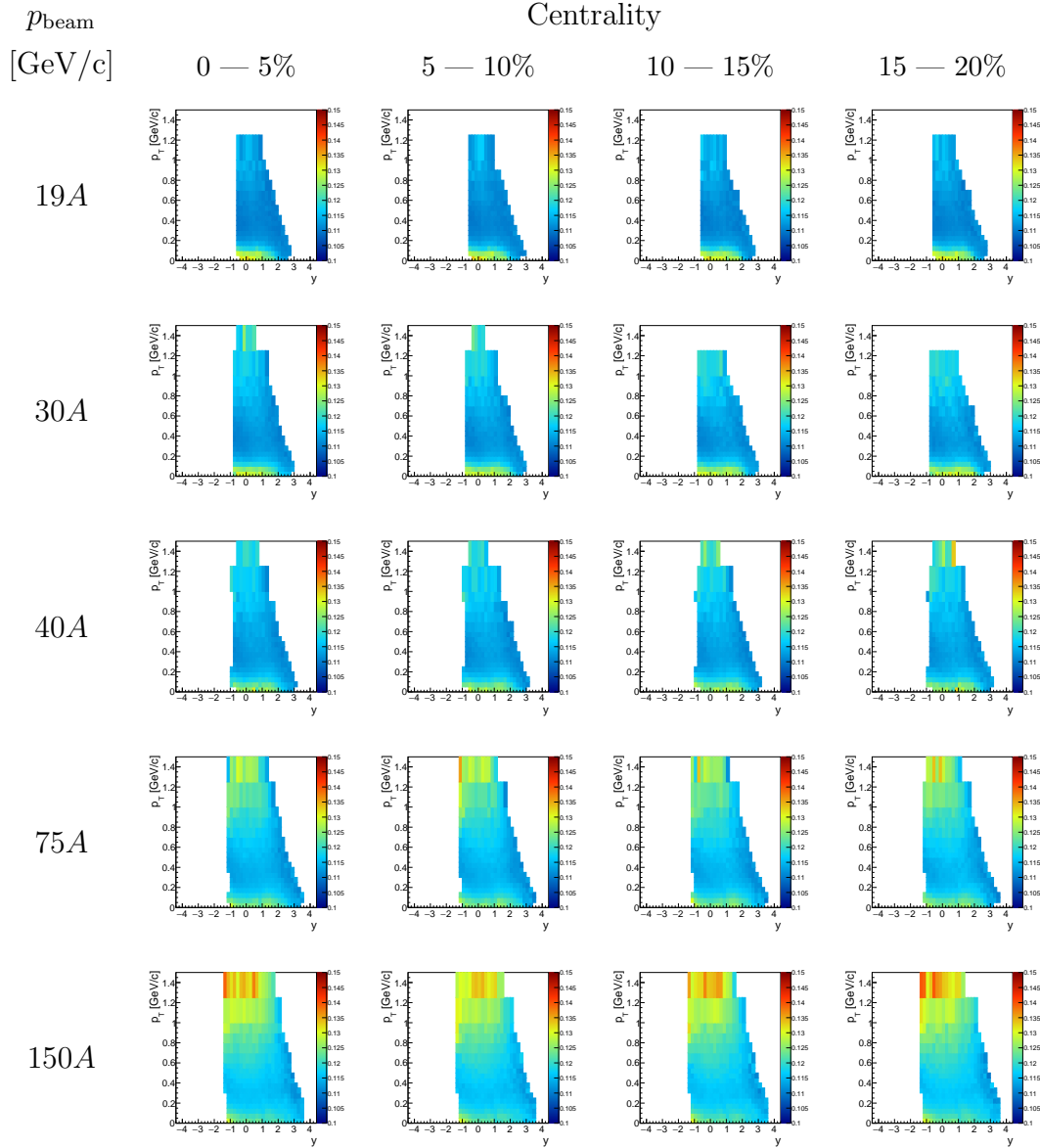Figure 93: Systematic error of the negatively charged pion spectra. Calculated as a quadrature sum of the systematic error contributions. The colour scale starts at 10% for better visibility of the structures in the systematic uncertainty.

out–of–target interactions (which are mostly $^7\text{Be}+^4\text{He}$ peripheral interactions) lowers the multiplicity. Therefore the total contributions of these two effects will

be event smaller. The systematic uncertainty contribution related to the cut on the Z coordinate of the fitted primary vertex will be neglected due to its low value.

The uncertainty related due to accepted events with off–time interactions in 0–120 ns from the trigger beam particle was calculated according to the procedure described in section 7.3. The negligible contribution of $< 1\%$ will not be taken into consideration.

The uncertainty due to tracking inefficiencies was tested by varying the track cuts and studying the changing acceptance as well as the changes of the fully corrected spectra in the smallest common acceptance. A test of the time stability of the spectra revealed discrepancy at $150A$ GeV/c at $y \approx 0.8$ and $p_{\mathrm{T}} \approx 0$. The fig. 94 shows the technical plot of the corrected rapidity spectra with the data divided into two periods. The discrepancy between first and second period is of the order of 4%. Such discrepancy would change the final results by 2%.
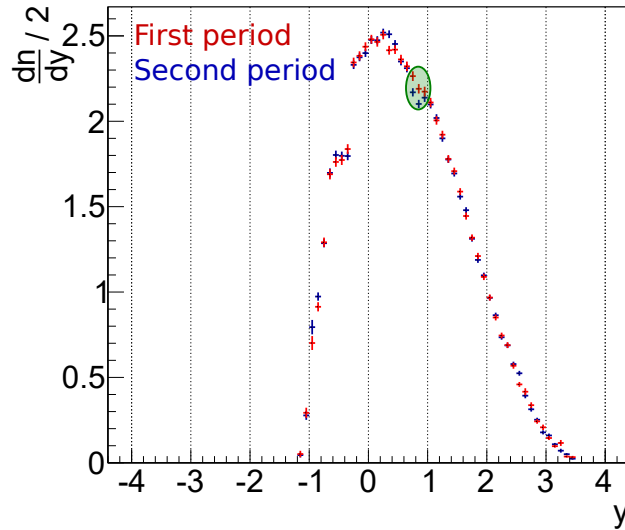

Figure 94: The discrepancy of the rapidity spectrum of the π^- mesons between two periods of the data taking.

The spectra instability with time and track cuts described above was corrected by finding the track category rejected in the second period and accepting them in

analysis. However, the undetected change in magnetic field or detector geometry could cause similar effects of lesser magnitude which were overlooked. To take them into account a 2% systematic error related to the tracking inefficiencies will be added to the total systematic error.

The dominant source of the systematic uncertainty is the uncertainty of the centrality definition.

The PSD allows to define kinematic region of the centrality determination in various ways by selecting different modules for the energy calculation. Some of these kinematic region will suffer from not including spectators with large Fermi motion, others will suffer from the inclusion of large amount of produced particles.

A person without access to the full simulation chain of the NA61/SHINE have no possibility to properly select centrality within studied model. There is an ongoing NA61/SHINE project which would facilitate simple comparisons with models by correcting PSD centrality selected data to centrality selected by more abstract variable (e.g. number of projectile spectators, number of particles with momentum higher than some threshold, impact parameter).

However, at the time of the writing of this thesis the project is far from being finished. Therefore, all the presented data was calculated with centrality selected with various ("reasonable") module regions. The spread of results was typically around 10%. This spread will be added to the systematic error of the results. Although, any comparison made with full simulation of the NA61/SHINE detector could be made without taking this systematic error into account.

12. Summary and Outlook

12.1. Physics results

This thesis presents experimental results on inelastic and production cross section, and inclusive spectra of negatively charged pions produced in centrality selected ^{7}Be + ^{9}Be interactions at five beam momenta: $19A$, $30A$, $40A$, $75S$, $150A$ GeV/c by strong and electromagnetic processes. The measurement was performed using the large acceptance NA61/SHINE hadron spectrometer located at CERN Super Proton Synchrotron.

The cross section results were compared with Glauber Monte–Carlo simulations from Geant4.10 package, as well as with a dedicated experimental measurement at beam momentum equal 1.45 GeV. The MC predictions seemed to describe NA61/SHINE data relatively well. A slight ($\approx 2\%$) overestimation within the systematic error of the NA61/SHINE measurement was observed. However, the MC overestimated the measuremnt at 1.45 GeV by 10%.

Two–dimensional spectra were defined in terms of rapidity and transverse momentum or mass. The statistical uncertainties were below 10% in large regions of the phase–space. The systematic uncertainties were approximately equal 10%, mostly due to the difficulties of centrality selection within small colliding system.

The results were obtained by removing a contribution of hadrons other than π^- from the unidentified spectra of negatively charged hadrons with use of the EPOS Monte–Carlo model. The resulting biases introduced by this and other corrections were studied and included in the systematic uncertainty.

The negatively charged pion spectra were not compared with the MC simulations due to large difficulties of determining precisely the same event selection in MC and in data. An additional correction to the experimental data is being developed which would allow unbiased comparisons between data and MC.

The only other available data of light ion collisions is the C + C data of the

NA49 experiment. The data is available at 40A GeV/c and 158A GeV/c beam momenta for minimum bias and semi–central collisions respectively. However, as described by NA49 collaboration, the beam quality was very poor and the centrality selection was not precise. Additionally, the published rapidity spectra show only data at forward rapidity with the assumption of forward–backward symmetry. This symmetry was disproven in this thesis for light ion collisions with centrality selected in one hemisphere only. All of the above problems makes useful comparison difficult. Therefore, quantitative comparison will not be tried.

12.2. Analysis building blocks

In addition to physics measurements various building blocks useful for all NA61/SHINE ion+ion analyses were developed.

Particle showers produced by beryllium ions in the PSD calorimeter were parametrized which enabled development of fast PSD simulator used by the collaboration for determination of centrality in simulated Monte–Carlo data.

^{7}Be + ^{9}Be collision centrality was determined. An easy to use software package was developed to use centrality data in any ^{7}Be + ^{9}Be analysis.

The non–biasing event cuts to selects only inelastic ^{7}Be + ^{9}Be interactions, without off–time collisions, from secondary fragmentation beam with bunched time structure were developed. A software package was written to facilitate use of the developed cuts by all ^{7}Be + ^{9}Be analyses. These cuts introduced non–biasing event cut culture into all ion + ion analyses performed by the NA61/SHINE collaboration.

12.3. Author's contribution

The analyses described in this work were done within the NA61/SHINE collaboration. The methods and results were discussed numerous times with the collaboration on various meetings both in-person, as well as over the internet. The final results of the analyses, as described above, could not be obtained without these discussions.

However, most of the actual data analysis was performed by the author himself. In particular the author executed following tasks (in order of appearance in this work):

- Calibration of beam and trigger detectors.

- Development of the event cuts specific to the ion analyses.

- Introduction of the distinction between biasing and non-biasing event cuts.

- Development of common software library allowing easy use of the event cuts in beryllium analyses.

- Determination of the production and inelastic cross section of the ^{7}Be + ^{9}Be interactions together with statistical and systematic error calculations.

- Determination of the centrality of the ^{7}Be + ^{9}Be collision in experimental data.

- Development of the common software library allowing easy centrality selection in beryllium analyses.

- Determination of the resolution of the PSD.

- Parametrization of the particle shower profiles in the PSD.

- Development of the fast, parametrized PSD simulator.

- Determination of the centrality in the Monte-Carlo data.

- Obtaining negatively charged pion spectra, including calculation of correction factor, and statistical and systematic errors.

- Parametrization of the negatively charged pion spectra and comparison with p + p and Pb + Pb data.

In addition the author was responsible for various tasks in the collaboration. The exact responsibilities were described in the first chapter of this work.

12.4. Outlook

The cross section measurement systematic uncertainty can be drastically lowered by remeasurement of the target geometry, as well as calibration of the energy loss of the GTPC detector. Both of these tasks will be performed resulting of order of magnitude more precise results being available for publication.

The procedure of correcting centrality selection based on the energy deposited in the PSD to the (currently unknown) variable available in the Monte–Carlo models will be implemented. Such correction would allow to directly compare Monte–Carlo models with experimental data.

The ^{7}Be + ^{9}Be data taken at beam momentum of $13A$ GeV/c will be analysed. Due to poor beam quality and trigger inefficiencies this dataset require separate, careful analysis.

The identified hadrons spectra analyses in ^{7}Be + ^{9}Be data performed by my colleagues will be finished, which together with this work will allow to shed more light on the question of quark–gluon plasma and the onset of deconfinement.

A. Coordinate system and kinematic variables

A.1. Coordinate system of the NA61/SHINE experiment

The coordinate system of the NA61/SHINE experiment have the origin in the middle of the VERTEX2 magnet. The Z axis of the system is pointed along the beam line downstream (away from the accelerator). The Y axis is vertical pointing upwards. The X axis is the horizontal axis which points left looking along the Z axis. The direction of the X axis is set in a way for coordinate system to be right-handed. In the North Area of CERN it is customary to call the directions of the X axis by the name of the mountains the axis points to. Therefore the positive values of X is so-called Jura side, and the negative values, so-called Saleve side.

A.2. Kinematic variables

The spectra of negatively charged pions are presented within a phase-space defined by various kinematic variables. These variables will be explained below.

A.2.1. Transverse variables

The transverse momentum is defined as:

$$p_\mathrm{T} = \sqrt{p_x^2 + p_y^2},$$

where p_x and p_y are particle momentum components perpendicular to the beam axis (Z)

The transverse mass is defined as:

$$m_\mathrm{T} = \sqrt{p_T^2 c^{-2]+m^2}},$$

where m is the mass of given particle. By definition $m_\mathrm{T} \geq m$, therefore the spectra are usually presented as a function of $m_\mathrm{T} - m$.

The transverse variables are Lorentz invariant under boost along the beam axis (Z).

A.2.2. Rapidity

In this work the rapidity is defined as:

$$y = \frac{1}{2} \log \frac{E + p_z c}{E - p_z c},$$

where E is the energy of the particle and p_z is the momentum component parallel to the beam line.

Rapidity is a dimensionless variable invariant with respect to the Lorentz transformation. It can be transformed from the laboratory frame of reference to the centre of mass frame of reference by subtracting a constant y_{beam}:

$$y_{\mathrm{CMS}} = y_{\mathrm{LAB}} - y_{\mathrm{beam}},$$

where

$$y_{\mathrm{beam}} = \mathrm{atanh} \frac{p_{\mathrm{beam}} c}{E_{\mathrm{beam}} + m_{\mathrm{p}} c^2},$$

where p_{beam} is the beam momentum, E_{beam} is the beam energy, and m_{p} is the mass of the proton. In this work rapidity is always given in the centre of mass frame of reference.

References

[1] C. Alt et al. Pion and kaon production in central Pb + Pb collisions at 20-A and 30-A-GeV: Evidence for the onset of deconfinement. *Phys. Rev.*, C77:024903, 2008.

[2] S. V. Afanasiev et al. Energy dependence of pion and kaon production in central Pb + Pb collisions. *Phys. Rev.*, C66:054902, 2002.

[3] Marek Gazdzicki and Mark I. Gorenstein. On the early stage of nucleus-nucleus collisions. *Acta Phys. Polon.*, B30:2705, 1999.

[4] R. V. Poberezhnyuk, M. Gazdzicki, and M. I. Gorenstein. Statistical Model of the Early Stage of nucleus-nucleus collisions with exact strangeness conservation. *Acta Phys. Polon.*, B46(10):1991, 2015.

[5] Marek Gazdzicki, Mark Gorenstein, and Peter Seyboth. Onset of deconfinement in nucleus-nucleus collisions: Review for pedestrians and experts. *Acta Phys. Polon.*, B42:307–351, 2011.

[6] RJ. Glauber. *In Lectures in Theoretical Physics*. Interscience, 1959. ed. WE Brittin and LG Dunham.

[7] Michael L. Miller, Klaus Reygers, Stephen J. Sanders, and Peter Steinberg. Glauber modeling in high energy nuclear collisions. *Ann. Rev. Nucl. Part. Sci.*, 57:205–243, 2007.

[8] I. Tanihata, H. Hamagaki, O. Hashimoto, Y. Shida, N. Yoshikawa, K. Sugimoto, O. Yamakawa, T. Kobayashi, and N. Takahashi. Measurements of Interaction Cross-Sections and Nuclear Radii in the Light p Shell Region. *Phys. Rev. Lett.*, 55:2676–2679, 1985.

[9] G. Agakichiev et al. Dielectron production in C-12+C-12 collisions at 2-AGeV with HADES. *Phys. Rev. Lett.*, 98:052302, 2007.

[10] G. Agakishiev et al. Measurement of charged pions in C-12 + C-12 collisions at 1A-GeV and 2A-GeV with HADES. *Eur. Phys. J.*, A40:45–59, 2009.

[11] K. Kanaki. *Study of Λ hyperon production in C+C collisions at 2 AGeV beam energy with the HADES spectrometer.* PhD thesis.

[12] A. Sadovski. *Investigation of K+ meson production in C+C collisions at 2 AGeV with HADES.* PhD thesis.

[13] A D Panagiotou, A Petridis, and G Vasileiadis. Large acceptance hadron detector for an investigation of Pb-induced reactions at the CERN SPS. Technical Report CERN-SPSLC-91-31. SPSLC-P-264, CERN, Geneva, 1991.

[14] Ingrid Kraus. *Hyperonenproduktion in C+C- und Si+Si-Kollisionen bei 158 GeV pro Nukleon.* PhD thesis.

[15] H H Gutbrod, A M Poskanzer, and H G Ritter. Plastic ball experiments. *Reports on Progress in Physics*, 52(10):1267, 1989.

[16] H. Ströbele and P. Danielewicz. *Relativistic Heavy Ion Collisions studied with the Streamer Chamber at the BEVALAC*, pages 45–61. Springer US, Boston, MA, 1989.

[17] Marek Gazdzicki, Z Fodor, and G Vesztergombi. Study of Hadron Production in Hadron-Nucleus and Nucleus-Nucleus Collisions at the CERN SPS. Technical Report SPSC-P-330. CERN-SPSC-2006-034, CERN, Geneva, Nov 2006. revised version submitted on 2006-11-06 12:38:20.

[18] C. De Marzo et al. Multiparticle Production on Hydrogen, Argon and Xenon Targets in a Streamer Chamber by 200-GeV/c Proton and anti-Proton Beams. *Phys. Rev.*, D26:1019, 1982.

[19] Study of relativistic nucleus-nucleus collisions at 60 and 200 GeV per nucleon. Technical Report CERN-SPSC-85-36. SPSC-M-407, CERN, Geneva, 1985.

[20] Clemens Adler, Alexei Denisov, Edmundo Garcia, Michael J. Murray, Herbert Strobele, and Sebastian N. White. The RHIC zero degree calorimeter. *Nucl. Instrum. Meth.*, A470:488–499, 2001.

[21] John Adams et al. Experimental and theoretical challenges in the search for

the quark gluon plasma: The STAR Collaboration's critical assessment of the evidence from RHIC collisions. *Nucl. Phys.*, A757:102–183, 2005.

[22] C. Adloff et al. Construction and Commissioning of the CALICE Analog Hadron Calorimeter Prototype. *JINST*, 5:P05004, 2010.

[23] http://www.linearcollider.org/.

[24] N. Abgrall et al. NA61/SHINE facility at the CERN SPS: beams and detector system. *JINST*, 9:P06005, 2014.

[25] Cinzia De Melis. The CERN accelerator complex. Complexe des accélérateurs du CERN. Jul 2016. General Photo.

[26] T. Pierog C. Baus and R. Ulrich. https://web.ikp.kit.edu/rulrich/crmc.html.

[27] Klaus Werner, Fu-Ming Liu, and Tanguy Pierog. Parton ladder splitting and the rapidity dependence of transverse momentum spectra in deuteron-gold collisions at RHIC. *Phys. Rev.*, C74:044902, 2006.

[28] K. Werner, T. Hirano, Iu. Karpenko, T. Pierog, S. Porteboeuf, M. Bleicher, and S. Haussler. Gribov-Regge theory, partons, remnants, strings - and the EPOS model for hadronic interactions. *Nucl. Phys. Proc. Suppl.*, 196:36–43, 2009.

[29] A. Aduszkiewicz et al. Measurements of $\pi^{\pm}$, $K^{\pm}$, p and $\bar{\text{p}}$ spectra in proton-proton interactions at 20, 31, 40, 80 and 158 GeV/c with the NA61/SHINE spectrometer at the CERN SPS. *Submitted to: Eur. Phys. J. C*, 2017.

[30] R. Brun, F. Bruyant, M. Maire, A. C. McPherson, and P. Zanarini. GEANT3. 1987.

[31] Georges Audi, O Bersillon, J Blachot, and AH Wapstra. The nubase evaluation of nuclear and decay properties. *Nuclear Physics A*, 624(1):1–124, 1997.

[32] Ilona Weimer. Measurement of the ^{7}Be $+$ ^{9}Be cross section at beam momenta of $13a$, $20a$ and $30a$ gev/c. Master's thesis, 2013.

[33] S. Kowalski. New beam detectors for primary ion beams. NA61/NA49 Collaboration meeting at CERN, 2014.

[34] S. Agostinelli et al. GEANT4: A Simulation toolkit. *Nucl. Instrum. Meth.*, A506:250–303, 2003.

[35] John Allison et al. Geant4 developments and applications. *IEEE Trans. Nucl. Sci.*, 53:270, 2006.

[36] J. Allison et al. Recent developments in $G_{EANT}4$. *Nucl. Instrum. Meth.*, A835:186–225, 2016.

[37] Alberto Ribon. Private communication.

[38] Roland Sipos, Andras Laszlo, Antoni Marcinek, Tom Paul, Marek Szuba, Michael Unger, Darko Veberic, and Oskar Wyszynski. The offline software framework of the NA61/SHINE experiment. *J. Phys. Conf. Ser.*, 396:022045, 2012.

[39] C. W. Fabjan and F. Gianotti. Calorimetry for Particle Physics. *CERN-EP*, page 075, 2013.

[40] F. Sefkow and M. Chadeeva. Parametrisation of hadron shower profiles in the calice sc-fe ahcal. CALICE Collaboration Meeting at Argonne, 2014.

[41] Yu. A. Kulchitsky and V. B. Vinogradov. Analytical representation of the longitudinal hadronic shower development. *Nucl. Instrum. Meth.*, A413:484–486, 1998.

[42] Milton Abramowitz and Irene A. Stegun, editors. *Handbook of Mathematical Functions with Formulas, Graphs and Mathematical Tables*, volume 55 of *Applied Mathematics Series*. National Bureau of Standards, Washington, D.C., 1964. Reprinted by Dover, New York.

[43] F. James and M. Roos. Minuit: A System for Function Minimization and Analysis of the Parameter Errors and Correlations. *Comput. Phys. Commun.*, 10:343–367, 1975.

[44] T. Anticic et al. Energy and centrality dependence of deuteron and proton production in Pb + Pb collisions at relativistic energies. *Phys. Rev.*, C69:024902, 2004.

[45] P. Braun-Munzinger, I. Heppe, and J. Stachel. Chemical equilibration in Pb + Pb collisions at the SPS. *Phys. Lett.*, B465:15–20, 1999.

[46] A. Aduszkiewicz et al. Production of Λ -hyperons in inelastic p+p interactions at 158 GeV/*c*. *Eur. Phys. J.*, C76(4):198, 2016.

[47] Katarzyna Grebieszkow. Hot strong matter. *PoS*, DIS2014:018, 2014.

[48] Szabolcs Borsanyi, Gergely Endrodi, Zoltan Fodor, Antal Jakovac, Sandor D. Katz, Stefan Krieg, Claudia Ratti, and Kalman K. Szabo. The QCD equation of state with dynamical quarks. *JHEP*, 11:077, 2010.

[49] C. Alt et al. Inclusive production of charged pions in p+p collisions at 158-GeV/c beam momentum. *Eur. Phys. J.*, C45:343–381, 2006.